PROPERTIES OF INTRINSIC AND CO-SPUTTERED HYDROGENATED AMORPHOUS SILICON FILMS AND SCHOTTKY PHOTOVOLTAIC DEVICES

By

Mark Gordon Thompson

A DISSERTATION

Submitted to
Michigan State University
in partial fulfillment of the requirements
for the degree of

DOCTOR OF PHILOSOPHY

Department of Electrical Engineering
and Systems Science

1980

ABSTRACT

PROPERTIES OF INTRINSIC AND CO-SPUTTERED
HYDROGENATED AMORPHOUS SILICON FILMS
AND SCHOTTKY PHOTOVOLTAIC DEVICES

By

Mark Gordon Thompson

This dissertation describes an investigation of hydrogenated amorphous silicon prepared by the technique of rf sputtering silicon in a reactive argon/hydrogen atmosphere. Significant contributions of this research include the results of co-sputtering silicon and substitutional impurities, and the establishment of minimum deposition atmosphere purity requirements for producing Schottky barrier photovoltaic devices.

Optical and electrical properties of intrinsic hydrogenated silicon films have been studied as functions of the hydrogen partial pressure in the sputtering atmosphere and the rf input power. Optical energy gap, dark conductivity, and photoconductivity depend critically on these deposition parameters. Also, the quality of the vacuum system, in particular the leak rate as compared to the gas flow rate, is an important quanity in determining film properties. A five fold increase in the $\mu\tau$ product, from $1.9 \times 10^{-9} cm^2/V$ to $9.6 \times 10^{-9} cm^2/V$, is observed going from a 98.6% pure atmosphere to a 99.98% pure atmosphere. Models are suggested to explain the observed behavior of dark

and photo conductivity.

Optical and electrical properties of hydrogenated amorphous silicon co-sputtered from composite targets containing 0 - 10.6% aluminum are also investigated. The room temperature conductivity varies over the range of $10^{-12}(\Omega\text{-cm})^{-1}$ to $10^{-5}(\Omega\text{-cm})^{-1}$ and the optical energy gap varies from 1.83eV to 0.87eV with these aluminum concentrations. Electron microprobe data indicate that films contain 2.2 times as much aluminum as is present in the target. Co-sputtering aluminum is observed to be a less efficient method of doping, in terms of the number of incorporated impurities that act as acceptors, than aluminum ion implantation. Using the extended state model, approximately one aluminum atom in three thousand acts as an acceptor in co-sputtered films.

The sample preparation conditions which yield rectifying Schottky barrier devices are described. Two of the important factors influencing device performance are the purity of the sputtering atmosphere and the method of Schottky metal contact deposition. When the sputtering atmosphere is 99.98% pure, Schottky barrier devices with good rectification characteristics are formed. For 99.7% pure atmosphere, rectifying devices are not formed. Sputtering the Schottky metal contact results in a large number of defect surface states caused by sputter damage, and rectifying devices are not formed, therefore, evaporation deposition of the Schottky metal is preferred. Results are reported for two gold-hydrogenated amorphous silicon photovoltaic devices fabricated with this technique. It is determined via spectral response data, that the conversion efficiency

(~0.1%) is limited by a narrow space charge layer only about 125Å thick. Wider space charge layers, and thus higher efficiencies, are anticipated for higher purity sputtering atmospheres.

ACKNOWLEDGMENTS

I would like to sincerely thank Dr. Donnie K. Reinhard, my advisor and friend, for his help and guidance throughout my entire gratuate program. It is certain that this research would not have been possible without him. Thanks also to my guidance committee, Dr. P. David Fisher, Dr. H. Roland Zapp, and Dr. Peter Schroeder, for their help and comments. In addition, I thank Dr. Patrick McCleer and Dr. John B. Kreer for their input. Finally, I thank Carol Graham for her assistance in the preparation of the final draft and for sharing this entire experience with me.

(This research was supported in part by the National Science Foundation, Grant No. ENG 79-10896)

TABLE OF CONTENTS

LIST OF FIGURES

CHAPTER I

INTRODUCTION

Hydrogenated amorphous silicon was first investigated in 1969 by Chittick et al. and has since received considerable attention from many research groups.[1] The material has been shown to contain significant amounts of bonded hydrogen, typically on the order of 15%, and may be properly considered a silicon-hydrogen alloy. Hydrogen is responsible for compensating dangling bonds and, as a consequence, hydrogenated amorphous silicon possesses an exceptionally low density of states in the gap and exhibits a number of unique properties for an amorphous semiconductor. Among these properties are a large photoconductive effect, a high intrinsic dark resistivity, and a sensitivity to both p and n type substitutional impurities. Both p-n junctions and Schottky barriers have been successfully fabricated. In addition, the methods of deposition are relatively simple, inexpensive, and adaptable to mass production. Hydrogenated amorphous silicon is being considered as a potential material for several thin film electronic devices and applications such as photodetectors for electrophotographic processes and vidicons, thin-film transistors and integrated circuits for drivers and controllers in large-area displays, and p-i-n devices and Schottky barriers for large-area solar photovoltaic arrays.

The growing need to develop inexpensive photovoltaic energy has

been the primary reason for interest in hydrogenated amorphous silicon. It is well known that the high cost of producing single-crystal silicon solar cells is the main reason photovoltaic power cannot yet compete economically with fossil fuel or nuclear power. It is estimated that a cost of 20¢ to 70¢ per peak watt produced with ten percent efficient solar cells would make photovoltaic power systems a viable alternative to conventional power.[2] Presently, crystalline silicon solar cells with 11 to 14 percent efficiencies are commercially available at a cost of approximately ten dollars per peak watt.[3] The U.S. Department of Energy has set a goal to reduce the cost of photovoltaic power to 70 cents (in 1980 dollars) per peak watt by 1986.[2] Significant reductions in cost may be possible by using hydrogenated amorphous silicon instead of single-crystal silicon, although at a likely sacrifice in device performance. The reductions in cost would result for three reasons.

1) The deposition processes are relatively simple and hence less expensive.
2) Amorphous silicon solar cells are thin-film devices approximately 1 micron thick, therefore, much less silicon is required per cell compared to crystalline silicon solar cells which are typically 250 microns thick.
3) The manufacturing process can be easily adapted to mass production.

It is unrealistic to expect amorphous devices to be of the same quality as the best single crystal devices, however, hydrogenated amorphous silicon thin-film solar cells have already been reported to have efficiencies as high as 5.5%.[4] This is below the ten percent

efficiency usually accepted as the minimum for an economically feasible system but there is considerable room for improvement. The latest estimate on the theoretical upper limit for conversion efficiency of hydrogenated amorphous silicon solar cells is approximately 16%.[5]

This thesis is motivated by the photovoltaic problem and describes an investigation of hydrogenated amorphous silicon prepared by the technique of rf sputtering. Significant contributions of this research include the results of the co-sputtering experiments and the establishment of minimum purity requirements for producing device quality material and Schottky barrier photovoltaic devices with a rf sputtering system. Chapter II outlines the background work on amorphous silicon that has lead to the present understanding of the material. Also, the state of the art in doping amorphous silicon and device fabrication are presented. In Chapter III the fabrication techniques of rf sputtering and the details of sample preparation are discussed. Also, the dependence of the electrical and optical properties of intrinsic hydrogenated amorphous silicon on sputtering input variables is investigated. Chapter IV reports an investigation of co-sputtering silicon and substitutional impurities from a composite target as an alternate technique for doping hydrogenated amorphous silicon. The fabrication of Schottky barrier devices and their electrical and photovoltaic properties are reported in Chapter V. Finally, Chapter VI summarizes these results and reviews several significant outstanding problems for future investigation.

CHAPTER II

BACKGROUND

Amorphous or non-crystalline semiconductors have become a topic of widespread interest in recent years from both a theoretical and applications point of view. In 1975 the potential application of amorphous ternary semiconductors to relatively inexpensive, large area, thin-film photovoltaic energy conversion devices was recognized. This potential stems from the development of a well controlled technique for substantial doping of hydrogenated amorphous silicon and germanium.[6,7] In addition to these experimental results, significant advances have been made in the theoretical understanding of non-crystalline materials. N.F. Mott and P.W. Anderson, for example, shared the 1977 Nobel Prize in physics due in part to their work in disordered systems. The level of knowledge surrounding non-crystalline semiconductors, however, remains much below that of crystalline semiconductiors and presents a challenging frontier to those involved in semiconductor physics and semiconductor applications.

The role of hydrogen in amorphous silicon films has been the key to recent developments on amorphous silicon thin film solar cells. Silicon, incidentally, is more suited to photovoltaic applications than germanium because of its more suitable energy gap. Chittick *et al.* first studied hydrogenated amorphous silicon in 1969.[1] They deposited films by the rf glow discharge decomposition of silane

(SiH_4) and observed a large photoconductivity effect and dark resistivities orders of magnitude higher than those observed in evaporated or argon sputtered amorphous silicon films. Brodsky noted that an electron paramagnetic resonance (EPR) signal, usually associated with dangling bonds on internal surfaces, was not observed in films produced by the glow discharge decomposition of silane in contrast to evaporated silicon films.[8] These observations suggest that the presence of hydrogen during film growth has a considerable effect on the structure and thus the electronic properties of amorphous silicon. A hypothesis was developed to explain the role of hydrogen in amorphous silicon as follows. Hydrogen atoms being small in diameter and monovalent enter the amorphous film by occupying vacant bonding sites (dangling bonds). When not bonded to hydrogen, dangling bonds give rise to localized defect states within the energy gap. However the energy of the hydrogen-silicon bond lies deep in the semiconductor's valence band, therefore, hydrogen acts as a termination agent and effectively neutralizes these defect states. The result is a relatively low density of localized states in the gap. This argument was supported by the work of Malhorta and Neudeck, and Spear, LeComber, and Madan.[9,10,11] Malhorta and Neudeck evaporated silicon in a partial pressure of hydrogen and observed, by means of field effect measurements, a reduction in band gap states with increasing hydrogen partial pressure. Spear et al. also investigated the field effect in glow discharge and evaporated silicon films. They reported a much lower density of states within the gap for silane produced films. In hydrogenated amorphous silicon the midgap density of states is typically 10^{17} cm^{-3}-eV^{-1}

compared to about 10^{20} cm^{-3}-eV^{-1} for non-hydrogenated material.[9] Also, the presence or absence of dangling bonds in amorphous semiconductors plays an important role in determining the effect of doping impurities on the electronic properties. For controlled substitutional doping of amorphous semiconductors to be possible it is essential that the density of localized defect states near the Fermi level be minimized. Although this can be accomplished to some extent by annealing, the most effective way appears to be by the incorporation of hydrogen into the material. Two groups independently progressed to the point of selectively doping hydrogenated amorphous silicon and producing thin-film p-n junctions. Spear and LeComber reported films produced by the glow discharge decompostion of silane with electrical conductivities ranging over ten orders of magnitude, from 10^{-12} $(\Omega\text{-cm})^{-1}$ to $10^{-2}(\Omega\text{-cm})^{-1}$, by introducing precise amounts of phosphine (PH_3) or diborane (B_2H_6) into the silane.[6] Phosphorous is a traditional n type impurity and boron is a traditional p type impurity in crystalline silicon. The range of doping induced changes in conductivity available in crystalline silicon is about the same, although it is shifted upward in conductivity with the highest conductivity being on the order of 10^4 $(\Omega\text{-cm})^{-1}$. They also produced p-n junctions by varying the impurity gas during deposition.[12] Carlson and Wronski, also using silane decomposition, reported thin-film amorphous silicon solar cells of the p-i-n and Schottky barrier type using similar doping techniques.[7,13] Work on these devices has resulted in solar cell efficiencies of up to 5.5% for Schottky barriers.[4] If the effect of hydrogen is to saturate dangling bonds, it should not be highly significant how it is

incorporated. Paul et al. obtained results comparable to those of silane decomposed films by rf sputtering in a mixed argon-hydrogen atmosphere.[14] Doping was again achieved by introducing phosphine or diborane into the sputtering gas and p-n junctions and Schottky barrier devices were formed. Thus, they showed that the sputtering method offered an alternative to silane decomposition for film preparation.

Investigations of infrared and Raman spectra of hydrogenated amorphous silicon have shown that hydrogen bonds into the network in several different bonding configurations.[15,16,17] Also, films with good electronic properties, such as high photoconductivity and good junction characteristics, contain one to two orders of magnitude more hydrogen than needed to compensate dangling bonds. These findings suggest that the role of hydrogen is much more complicated than first believed. The types of structural defects present in the film as well as the bonding configurations of hydrogen are dependent on the method of preparation (silane decomposition or reactive rf sputtering, for example) and also on the details of the preparation conditions. Paul et al. have studied the effect of hydrogen partial pressure and substrate temperature on hydrogen bonding and transport properties in rf sputtered amorphous silicon films.[17,18] For substrate temperatures between 200° C and 350° C they observe that small amounts of hydrogen in the sputtering gas decreases the room temperature conductivity by up to seven orders of magnitude and the conductivity becomes singly activated between 80° C and 250° C. For hydrogen partial pressures greater than 0.2 mTorr they observe three types of

hydrogen bonding: monohydride (Si-H), dihydride ($Si-H_2$), and trihydride ($Si-H_3$) bonding, with dihydride usually being the dominate configuration. This differs from reports on silane decomposed films which contain predominately monohydride bonds when deposited on substrates at 250° C or above.[16] Jeffrey, Shanks and Danielson present data which suggest that monohydride bonding is the preferred configuration for good semiconductor properties such as high carrier mobilities and long lifetimes.[19] They have achieved predominately monohydride bonding by increasing the sputtering power and suggest that the ion temperature in the plasma is the parameter which controls the hydrogen bonding.

It may be noted that the role of hydrogen as a terminating agent in amorphous silicon is not, apparently, completely unique. Ovshinsky et al. have reported comparable quality silicon films using flourine rather than hydrogen.[20] In fact, they report a lower density of states in the gap for flourinated silicon than for hydrogenated silicon. However, most work has been on hydrogenated films and devices.

Because of the sensitivity of hydrogenated amorphous silicon to preparation conditions, there has been a great deal of interest in investigating alternate schemes of achieving doped material. Such ideas as co-evaporation and co-sputtering from composite targets have so far resulted in only limited success.[21,22] Ion implantation, on the other hand, has been used to control the conductivity of hydrogenated amorphous silicon over the same range as for gas phase doping by

implanting phosphorous and boron ions to a concentration of 3×10^{21} cm^{-3} into films held at 250° C.[23] To date, however, gas phase remains the most efficient method of doping in terms of the number of impurity atoms incorporated into the film that act as donors or acceptors.

RCA Laboratories reported the first hydrogenated amorphous silicon solar cells in 1975.[7] Several device structures were investigated including p-n junctions, p-i-n devices and Schottky barriers. These early cells had efficiencies on the order of 1% - 2%. In 1976 a 5.5% efficient cell of small area was reported.[4] It was fabricated in a metal-insulator-semiconductor (MIS) structure with a partially transparent platinum contact. There have been problems with the stability of junction characteristics for Schottky barrier devices, however, and presently the emphasis is on the development of large area p-i-n devices. A group at Osaka University has obtained efficiencies as high as 4.5% with a p-i-n cell having a sensitive area of 9 cm^2.[24] The theoretical upper limit of conversion efficiency for p-i-n hydrogenated amorphous silicon solar cells is estimated at about 16%.[5] To approach this, however, several problem areas must be resolved. These include further reduction of the defect density of undoped amorphous silicon to help reduce recombination losses and improvement in the quality of doped material to increase the built-in potential and reduce the series resistance.

CHAPTER III

INTRINSIC HYDROGENATED AMORPHOUS SILICON MATERIAL PROPERTIES AS A FUNCTION OF SELECTED DEPOSITION PARAMETERS

3.1 Introduction

Hydrogenated amorphous silicon material properties are highly sensitive to preparation conditions. Diode rf sputtering is a useful technique for depositing amorphous silicon films in that there are a number of sputtering input parameters that may be adjusted over a wide range to facilitate the optimization of material properties.

Among the various deposition parameters that are likely to play an important role in determining the properties of rf sputtered hydrogenated amorphous silicon are: partial pressure of hydrogen in the sputtering atmosphere, substrate temperature, rf input power, argon partial pressure, flow rate of sputtering gas, substrate to target spacing, and substrate bias. Other conditions that will effect film properties but are rather fixed for a given system are the quality of the vacuum system and the concentration of contaminates present in the sputtering gas and target. In many cases these sputtering variables are not independent and must be optimized simultaneously to achieve the best semiconductor properties.

This chapter describes the fabrication of rf sputtered hydrogenated amorphous silicon samples and the experimental procedures for determining optical and electrical properties. The optical and electrical

properties have been studied for intrinsic samples prepared at different hydrogen partial pressures and rf input powers. Based on previously reported work, these two parameters were judged to be most crucial to optimizing the performance of a given sputtering system. It is noted that when the rf power is the independently varied sputtering parameter, other sputtering parameters may change with it. These include sputter rate, sputter voltage, and ion temperature. The same is true for hydrogen partial pressure. For example, at high hydrogen partial pressure the sputter rate decreases. This is because hydrogen, being a light ion, carries a large portion of the discharge current while contributing little to the sputtering yield.

3.2 Fabrication Techniques

3.2.1 RF Sputtering System

Sputtering as a physical phenomenon has been known and studied for over 100 years. During this time,it has developed into a useful technique of film deposition and nonchemical etching of a wide variety of materials. The process of sputtering deposition, or etching, involves the removal of surface atoms from a solid cathode or target by bombardment from positive ions originating in a plasma discharge.

Radio frequency sputtering is a particularly useful and versatile form of sputtering because it allows the deposition of both metals and dielectrics. In a diode rf sputtering system,the rf field between the two electrodes ionizes the sputtering gas atoms and maintains a low pressure discharge plasma. Because the electrons in the plasma are much lighter and thus more mobile than the ions, they rapidly move

from electrode to electrode as the rf voltage changes polarity. As a result, most of the rf current in the external circuit is due to electrons collected from the plasma and the electrodes assume a negative potential with respect to the plasma. For a system with equal area electrodes and no blocking capacitor, positive ions from the sputtering gas are attracted equally to both electrodes resulting in equal sputtering of both surfaces.[25,26]

In most practical rf diode sputtering systems, one electrode is appreciably larger than the other and a blocking capacitor is inserted in the external circuit. Since the total current through each electrode must be the same, the current density at the smaller electrode will be greater than that at the larger electrode. From the Langmuir equation, a larger current density corresponds to a larger potential difference between the electrode and plasma.[25] With the capacitor in the external circuit blocking dc charges from leaking away, the smaller electrode can assume a significantly higher negative dc potential than the larger one. Thus, positive ions from the sputtering gas are strongly attracted to the smaller electrode and only weakly attracted to the larger electrode. Sputtering is a threshold phenomena with the threshold energy depending on, among other things, the velocity and mass of the bombarding ion. Therefore, under the right conditions most of the sputtering will occur from the smaller electrode which is made the cathode or target. In some systems, such as the one described below, the large area electrode consists of the grounded substrate holder as well as the grounded walls of the can and ground shield around the target.

Radio frequency diode sputtering is the technique used in this research for the deposition of amorphous silicon films and most of the metal electrical contacts. The rf sputtering system is designed to be a highly flexible and easily maintained system. It is similar to a system previously described by Reinhard.[27] The sputtering chamber itself is constructed of stainless steel and is 8 inches high and 6 inches in diameter. The removable flanged top is equipped with a viewing window, electrical feed through and substrate shutter. It is sealed with a copper gasket and secured with 20 bolts to provide a high vacuum connection and yet allow easy access to the interior of the chamber. The system is designed to accept targets of any size up to four inches in diameter. Two inch diameter targets are used in this work and are a good trade-off between conserving target material and achieving high sputtering yield. Several targets have been constructed. Among those used in this research are silicon, molybdenum, platinum, nichrome and indium. A typical target consists of a sheet or foil of the material cut in a two inch diameter circle and fixed to an aluminum backing plate with silver conducting epoxy. The aluminum backing plate is then connected to the water cooled target assembly (cathode) via an O-ring seal and six bolts. Water cooling of the target is necessary because sputtering is an inefficient process with less than 1% of the input power contributing to the actual ejection of target atoms and most of the rest being dissipated as heat.[25] It is noted that it is not absolutely necessary to fix the target material to the aluminum backing plate as described. The conducting epoxy has a relatively low thermal conductivity (0.016 $W\text{-}cm^{-1}\text{-}K^{-1}$), so not much is lost in terms of heat dissipation by simply setting the

target material on the backing plate. This is convenient in that the entire target assembly does not have to be removed in order to change targets. All that is required is to change the target disk on top of the backing plate and re-adjust the target height via an o-ring Ultra-Torr connector to maintain the top of the target a few millimeters above the edge of the ground shield. This adjustment is necessary to compensate for differences in target thickness.

The substrate holder is a two inch diameter stainless steel disk suspended from the top of the sputtering can. This "sputter-up" system has the advantage that dust particles will not settle on the substrate and contaminate, or cause pinholes in the film. The substrate holder is electrically insulated from the top and walls of the chamber with a teflon spacer so that a dc or rf voltage can be applied to facilitate bias or back sputtering. During the deposition phase of a sputtering run though, the substrate holder is grounded. The target to substrate distance is adjustable from about 10.5 cm to 5.5 cm by simply loosening the O-ring connector and sliding the assembly up or down. The substrate holder can be either water cooled or heated with a cylindrical cartridge heater. Two heaters of different ratings are used. One is rated at 120 volts - 75 watts and is capable of heating the substrate to a maximum of 175^{o} C without degradation of the heater. The second heater is rated at 240 volts - 250 watts and achieves substrate temperatures of greater than 250^{o} C. The substrate temperature is monitored by a thermocouple clipped to the substrate such that it is shielded from direct exposure to the plasma.

The sputtering chamber is mounted on a portable support table which houses the target cooling system, the rf matching network, a blocking

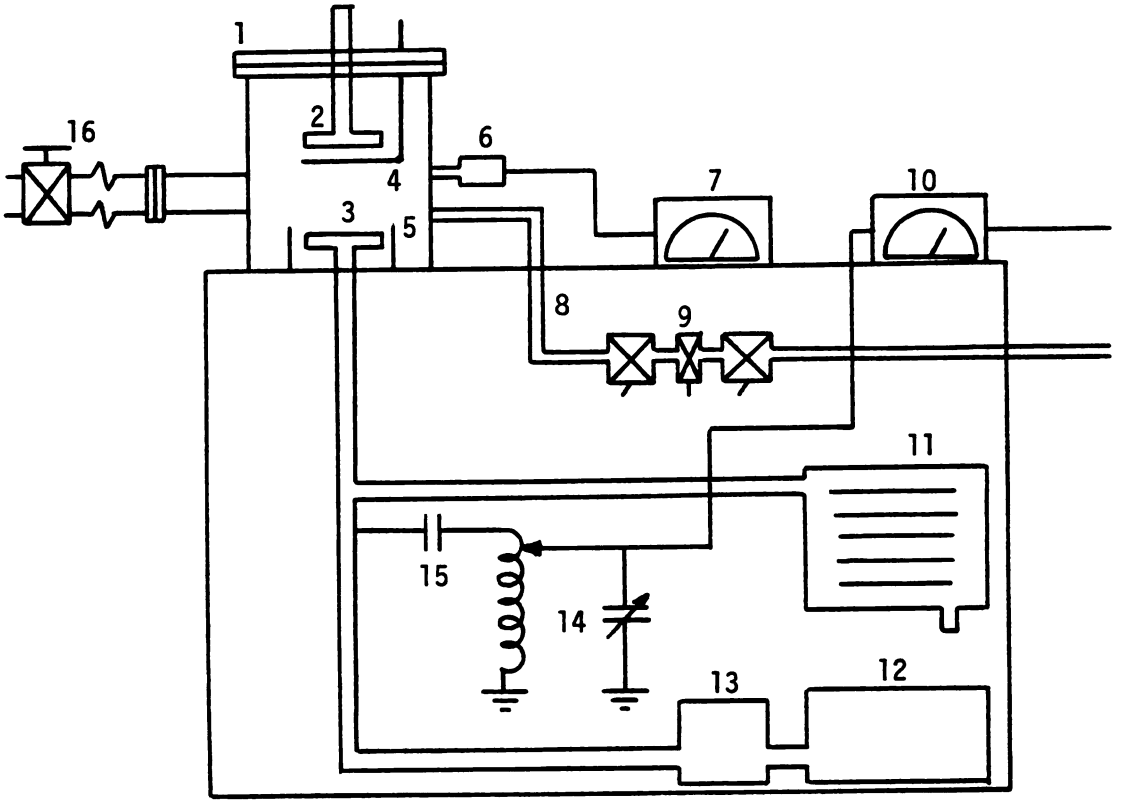

1. Sputtering Chamber
2. Substrate Holder
3. Target
4. Shutter
5. Ground Shield
6. Pirani Tube
7. Pirani Gauge
8. Sputtering Gas Line
9. Gas Control Valves
10. Power Meter
11. Radiator
12. Coolant Storage Tank
13. Water Pump
14. Matching Network
15. Blocking Capacitor
16. Isolation Valve

Figure 3.1 Schematic of rf sputtering system

capacitor and the sputtering gas control values (Figure 3.1). The closed cycle target cooling system consists of a water pump, radiator, water storage tank and several feet of interconnecting plastic tubing. The system circulates water through the target assembly at 1.4 liter/min to prevent overheating and deterioration of the targets. The rf power is supplied by a 500 watt, 13.56 MHz generator connected to the cathode through an impedance matching network and a 500 pf blocking capacitor. The matching network is used to match the sputtering chamber to the rf generator and is necessary to prevent high reflected powers from damaging the output stage of the generator. The incident and reflected power is monitored by a 2-30 MHz power meter in the feedline. The network is cooled by a fan mounted inside the support table. The flow of the sputtering gas is controlled by two on-off toggle valves and a metering valve mounted on the front of the support table. All sputtering gas lines are 1/4" O.D. copper tubing. The pressure in the chamber is measured with a Pirani gauge with a range of 100 mTorr to 0.1 mTorr.

The vacuum system employed with this sputtering system is part of a CVC vacuum evaporation unit and consists of a rotary type mechanical pump for roughing and a four inch, water cooled, oil diffusion pump that is capable of base pressures of about 1×10^{-6} Torr. Base pressures in the system are measured with an ionization gauge mounted in the base plate of the evaporation bell jar. The diffusion pump has a freon chilled cold trap to reduce oil contamination in the system. The sputtering system and evaporation system sit side by side and are interconnected by a 1 5/8" diameter flexible stainless steel tube and a bellows-sealed isolation valve.

The gas mixing system is set up to handle two gases, argon and hydrogen. These two cylinders are connected together with copper tubing to a third smaller mixing tank. Each cylinder is equipped with a regulator and pressure gauge to control the mixing ratio. Details of the gas mixing procedure are presented in the following section.

3.2.2 Sample Preparation

All amorphous silicon films in this study are prepared by rf sputtering in the system described in Section 3.2.1. Most of the electrical contacts to these samples are also deposited by sputtering although some are thermally evaporated in the CVC system. Three types of samples are prepared for different diagnostic purposes. They are; optical transmission samples, infrared transmission samples, and electrical samples in both a sandwich and coplanar geometry. The procedures for preparing these samples are very important to ensure reliable and repeatable results. This section outlines in detail the procedural steps for fabricating typical samples including the operation of the vacuum system and the gas handling system.

The warm-up procedure for the diffusion pump is as follows. First turn on the roughing pump and open the backing valve to allow it to evacuate the foreline of the diffusion pump. The foreline pressure must be below 50 mTorr before turning on the diffusion pump heaters, and at all times during the operation of the diffusion pump. The water cooling for the diffusion pump is interconnected with the roughing pump and should come on automatically, however, the water flow should be checked before proceeding. Next turn on the diffusion pump and allow

it to warm up for 20 to 30 minutes before turning on the cold trap. If the pump is not sufficiently warmed up when the cold trap cools down, gases may condense on the trap and outgasing may occur for several hours. It is best to check that the pump is hot with a light touch of the hand before proceeding to turn on the freon cold trap. The cold trap should be allowed 10 to 15 minutes to cool down.

While the vacuum system is warming up, the target and substrate can be prepared for sputtering. The target is placed on top of the aluminum backing plate of the cathode assembly. The entire assembly is then adjusted up or down via the o-ring connector such that the top surface of the target is 1/16" to 1/8" above the edge of the ground shield. The copper strip that connects the cathode assembly to the blocking capacitor and the rf power should be checked for security as should all of the target cooling lines.

The substrate is prepared for sputtering by thoroughly cleaning it to remove any dirt or grease that may contaminate the film or cause pinholes. The standard cleaning procedure is to rinse the substrate first in acetone, then methanol and finally in deionized distilled water followed by drying in a nitrogen stream. Glass 1" x 1" microscope cover slip substrates are used for the optical and electrical samples. For infrared transmission samples, 15 to 17 mils thick crystalline silicon substrates are used. The doping, which is not critical, was 5 to 8 Ω-cm p type. After cleaning and drying, the substrate is placed on a 1" x 3" microscope slide on the substrate holder. The appropriate mask is then aligned and held in place by the clips on the substrate holder. To monitor the substrate temperature during

the run, a thermocouple is placed under one of the clips on the microscope slide. The electrical and optical samples are mounted side by side and deposited at the same time.

Once the substrates are mounted, the shutter is put in place and the top is carefully positioned on the sputtering can. The bolts are tightened in such a way as to keep the pressure even on the flanges. One way of doing this is to tighten every other bolt in pairs opposite each other. Going twice around the can in this manner should secure the top with a vacuum tight seal. When the diffusion pump is completely warmed up, close the backing valve, open the roughing valve, and open the isolation valve between the bell jar and the sputtering can. Make sure the bell jar is in place. Open all valves in the sputtering gas line, including the needle valve, and open the valve on the mixing tank to allow the roughing pump to evacuate the entire system, up to the hydrogen and argon tanks, down to about 30 mTorr. This takes from 45 to 60 minutes. If the diffusion pump is properly warmed up the foreline pressure will remain less than 50 mTorr for this time. When the pressure reaches 30 mTorr in the system, close the roughing valve, open the backing valve, and slowly open the high vacuum valve, keeping the foreline pressure less than 50 mTorr. Now, let the diffusion pump evacuate the system, including mixing tank, down to base pressure. This takes several hours due to the small diameter and thus low conductance of the gas lines. In fact, this conductance could cause a substantial pressure difference between the mixing tank or sputtering can and the base plate of the bell jar where the base pressure of the system is measured.

The pumping speed of the diffusion pump, S_p, is approximately 500 liters/sec at 2×10^{-6} Torr base pressure which corresponds to a throughput of 1 μ-liter/sec where μ refers to a pressure of one micron of mercury, or 1 mTorr. Expressed in cubic centimeters per second at standard temperature and pressure, the throughput is

$$\frac{1\ \mu\text{-liter/sec}}{760} = 1.3 \times 10^{-3}\ \text{scc/sec}$$

The conductance of the piping to the sputtering chamber is 5 liters/sec, so the pressure differential between the diffusion pump and sputtering chamber is

$$\Delta P = \frac{Q}{C} = \frac{1\ \mu\text{-liter/sec}}{5\ \text{liters/sec}} = 0.2\ \mu = 2 \times 10^{-4}\ \text{Torr.}$$

So the pressure in the sputtering chamber is approximately 0.2 mTorr. Between the pump and mixing tank the conductance is much smaller, 6×10^{-3} liters/sec, due to 1/4" O.D. lines. The pressure differential in this case is

$$\Delta P = \frac{1\ \mu\text{-liter/sec}}{6 \times 10^{-3}\ \text{liters/sec}} = 170\ \mu.$$

So the pressure in the mixing tank is approximately 0.17 Torr.

These may be taken as upper limits for two reasons. First the pumping speed of 500 liters/sec is for a new pump with fresh oil. Secondly the system leak rate is observed to be 3×10^{-6} scc/sec under best conditions. This is too small to support, in steady state,

the throughput used in the previous calculations. A lower throughput would correspond to lower values of ΔP.

The effect of 170 mTorr in the holding tank prior to filling is marginally significant. If 2 atmospheres of sputtering gas are supplied, the purity of the mixture (assuming pure sputtering gases) is 99.99%. This is equal to the purity of the argon sputtering gas.

To mix the sputtering gas, the partial pressures of argon and hydrogen desired during sputtering must be known as well as the total pressure of gas to be mixed in pounds per square inch as read on the regulator gauge. For example, assume a total of 30 psi (2 atmospheres) of gas is to be mixed and a partial pressure of 5 mTorr of argon and 3 mTorr of hydrogen is desired during sputtering. Then $(\frac{5}{5+3} \cdot 30) =$ 18.75 psi of argon should be mixed with $(\frac{3}{5+3} \cdot 30) = 11.25$ psi of hydrogen. To mix the gas once the mixing tank is evacuated, close one of the toggle valves in the gas line, open the valve on the argon tank and adjust the regulator valve to bring the pressure in the mixing tank up to 3.75 psi. This corresponds to a total argon pressure of 18.75 psi since the regulator gauge only reads above atmospheric pressure and 1 atmosphere is approximately 15 psi. Next close the valve on the argon tank and open the valve on the hydrogen tank. Adjust the hydrogen regulator to bring the total pressure in the mixing tank to 30 psi. Allow a few minutes for equilibrium to be reached,then close the valve on the mixing tank and evacuate the gas lines as described previously. When the lines are evacuated again, pressurize them by closing the needle valve to the zero position and open the valve on the mixing tank. Throttle the diffusion

pump so that the high vacuum valve is about 2 1/2 turns open and then adjust the needle valve to bring the chamber up to the desired pressure. Turn on the target cooling system, the matching network cooling fan, and the rf generator. Connect the variac to the substrate heater and turn it on.

A typical sample fabrication involves:

1) sputter cleaning the target with the shutter in place for 5 minutes;
2) back bias sputter cleaning the substrate with the shutter retracted for 5 minutes;
3) depositing the sample film with the shutter retracted and the substrate grounded.

The discharge should start easily with the application of the rf power to the target. It may be necessary to increase the pressure at first to initiate the discharge. Once the glow has started, minimize the reflected power by adjusting the inductor and capacitor in the matching network. The chamber can usually be matched so that less than 5 watts of power are reflected. When a good match is achieved adjust the incident power to the desired level. For the first five minutes the shutter is in place shielding the substrate from any deposition to ensure a clean target surface. Before removing the shutter check the temperature of the substrate on the thermocouple gauge. Adjustments are made with the variac. If the substrate temperature is acceptable, retract the shutter and apply a -15 volt dc bias to the substrate for 5 minutes to induce back sputtering to help remove any oxidation or contamination that may have occured on

the substrate. After sputter cleaning, ground the substrate and deposit the film for the allotted time. To achieve 1 μm thick films, typical sputtering times are 2 to 3 hours. During this time it may be necessary to adjust the needle valve to maintain the correct pressure, rematch the chamber to minimize reflected power or adjust the variac to maintain the correct substrate temperature.

3.3 Optical Properties

3.3.1 Optical Absorption Coefficient

Optical absorption data is obtained from transmittance and reflectance measurements on optical sample films deposited on glass coverslip substrates in the experimental arrangement shown in Figure 3.2 and Figure 3.3. A Bausch and Lomb grating monochrometer supplies a monochromatic photon beam from 0.8 eV to 2.5 eV using combinations of two gratings, a visible grating and an infrared grating, and three optical filters to eliminate higher order spectra. The photon beam is chopped at about 200 Hz and split with a partially transmitting mirror. The two detectors, A and B, are germanium photodiodes. The outputs of the detectors are fed into a phase-locked amplifier (PLA) to improve the signal to noise ratio. The reference signal for the PLA is derived from detector B after amplifying it with an instrumentation amplifier. The outputs of the detectors are measured without the sample in place, V_A and V_B, and with the sample in place, V_A' and V_B', over the range of wavelengths of interest. For reflection measurements without the sample in place, a totally reflecting mirror is positioned in place of the sample. The transmittance (or reflectance)

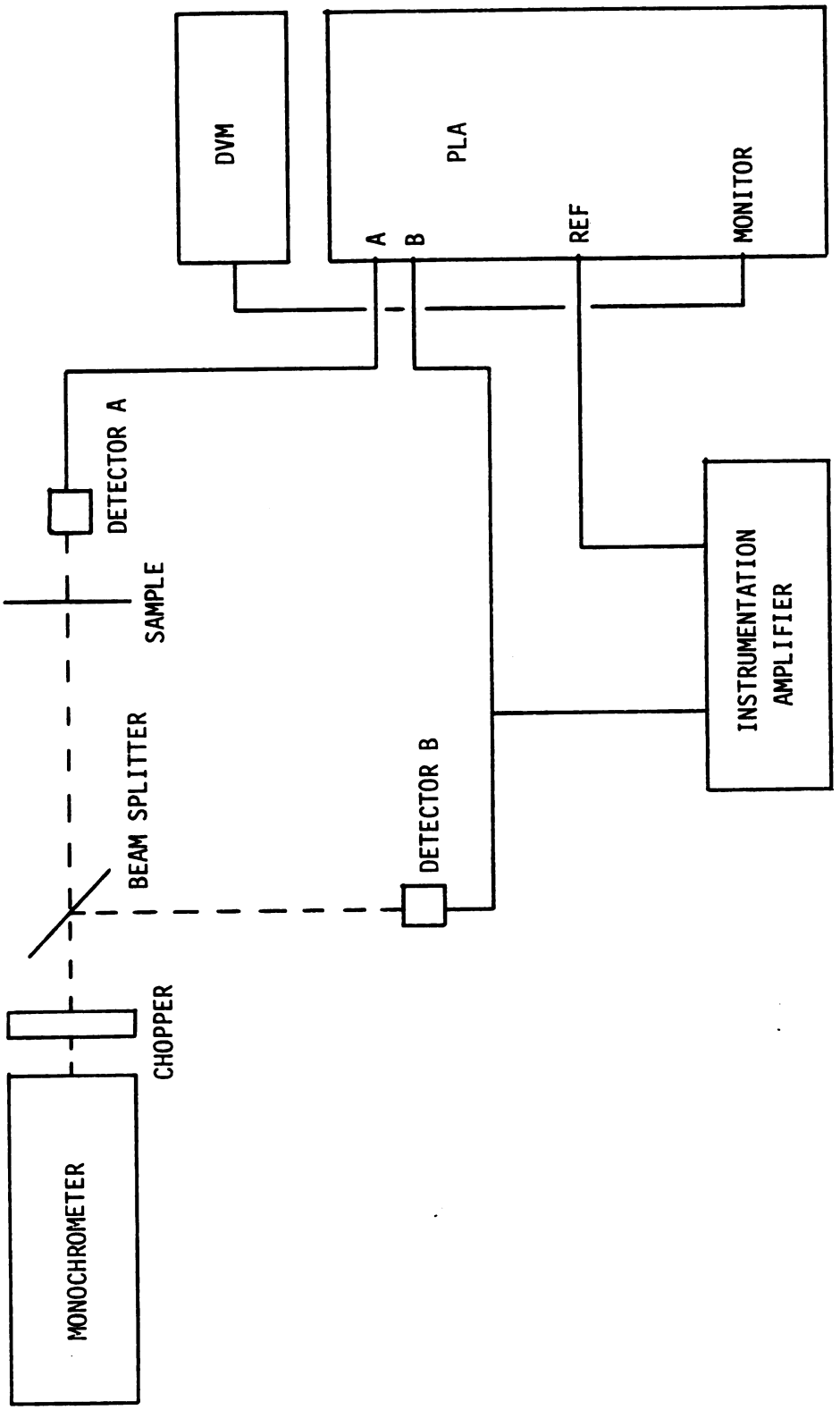

Figure 3.2 Experimental transmittance setup.

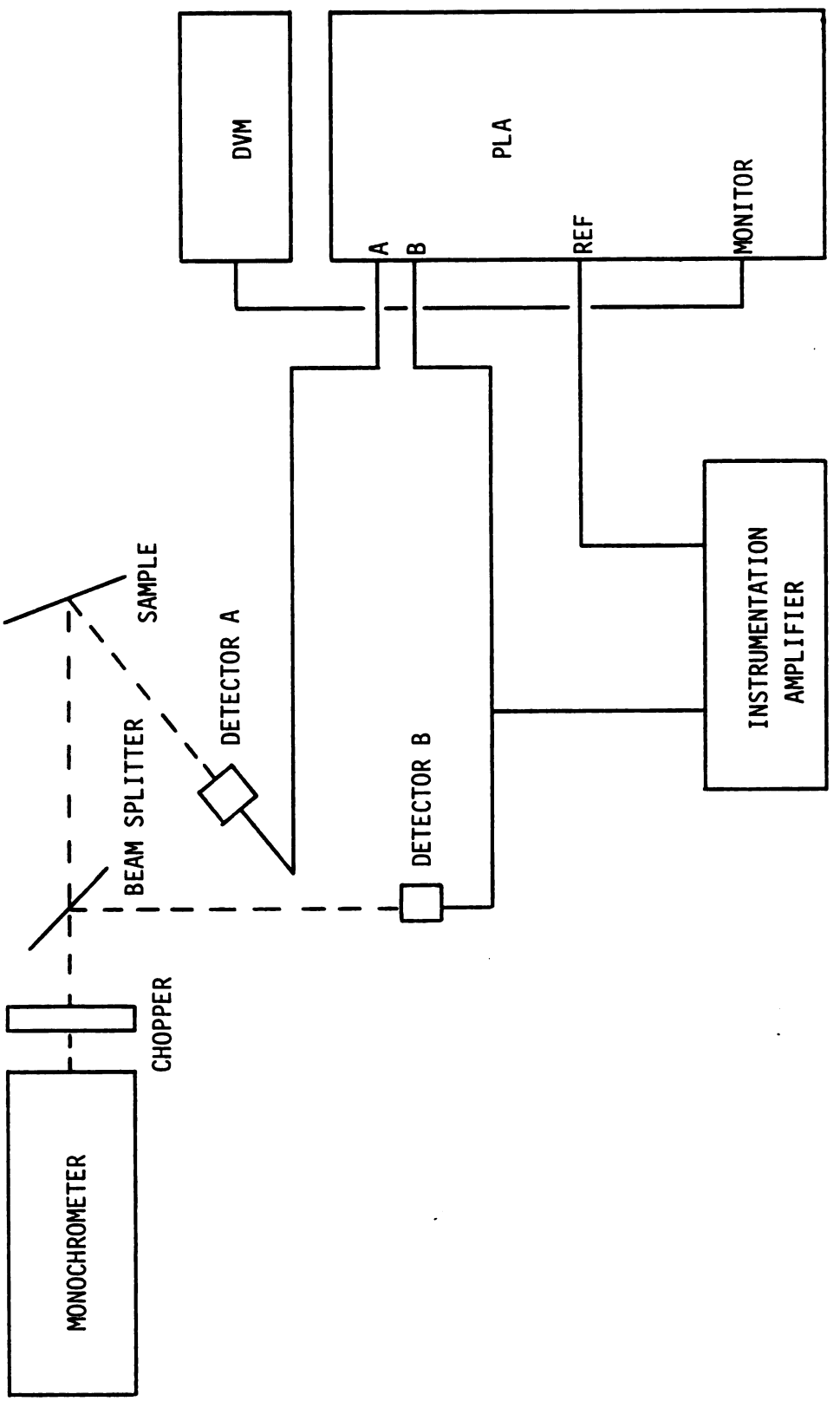

Figure 3.3 Experimental reflectance setup.

is then determined as

$$T = \frac{V_B}{V_A}\frac{V_{A'}}{V_{B'}} .$$

This technique compensates for instrumentation drift between measurements.

Structure in the transmittance curves is due to three related phenomena; absorption, reflection, and interference (Figure 3.4). For a freely supported sample with air boundaries front and back, the transmittance is given by

$$T = \frac{(1-R)^2 e^{-\alpha d}}{1 + R^2 e^{-2\alpha d} - 2e^{-\alpha d} R^2 \cos(2\theta+\psi)}$$

where the third term in the denominator represents the interference contribution and accounts for the observed maxima and minima in the longer wavelength transmittance.[28] Also, α is the optical absorption coefficient, d is the film thickness, and R is the reflectance of the air/film interface. However, our samples are not surrounded by air on both sides but are deposited on glass substrates. The transmittance of an absorbing film on a non-absorbing substrate in the limit of incoherent multiple reflections or, equivalently, after numerically averaging of the interference maxima and minima, may be written as[29]

$$T = \frac{T_{FS}(1-R_3)}{1 - R_3 R_{FS}}$$

where

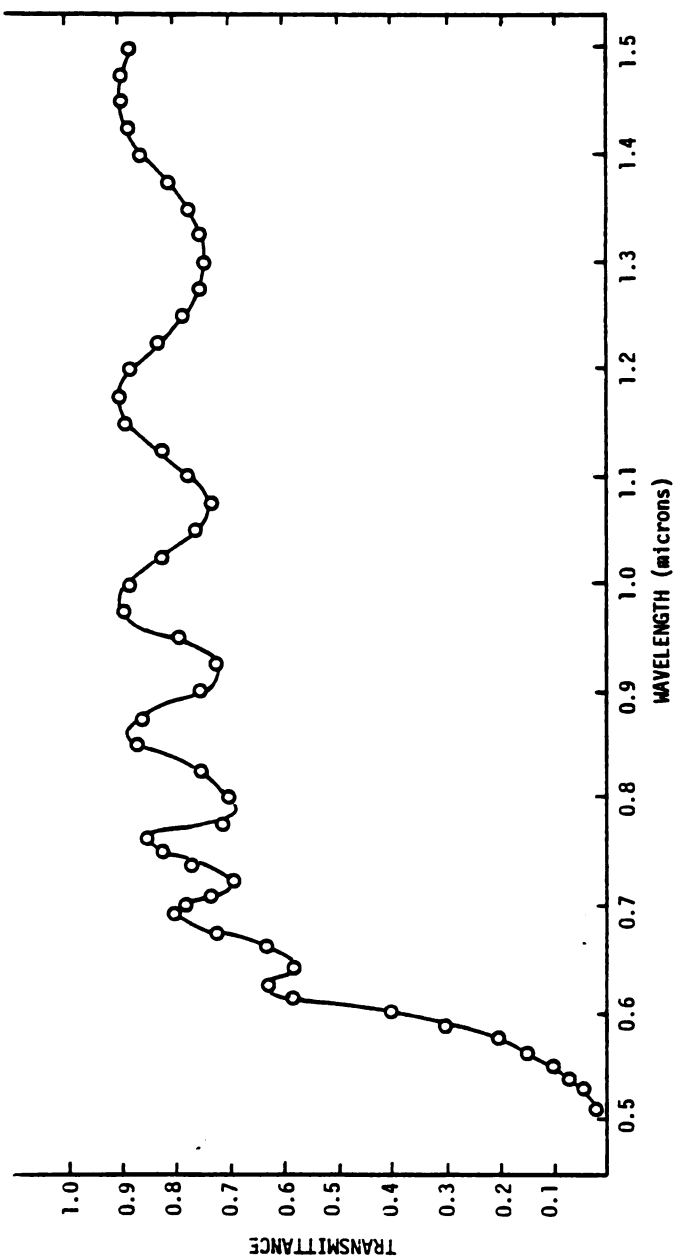

Figure 3.4 Typical transmittance vs. wavelength curve.

$$T_{FS} = \frac{(1-R_1)\ (1-R_2)\ e^{-\alpha d}}{1 - R_1R_2\ e^{-2\alpha d}}$$

is the transmittance of the film into a semi-infinite substrate, and

$$R_{FS} = \frac{R_2 + R_1e^{-2\alpha d}\ (1 - 2R_2)}{1 - R_1R_2e^{-2\alpha d}}$$

is the reflectance for light impinging on the film from the substrate. R_1, R_2, and R_3 are the reflectances from the air/film, film/substrate, and substrate/air interfaces, respectively. Again d is the film thickness and α is the optical absorption coefficient of the film. These equations may be combined to yeild[30]

$$T = \frac{(1 - R_1)\ (1 - R_2)\ (1 - R_3)\ e^{-\alpha d}}{1 - R_2R_3 - (R_1R_2 + R_1R_3 - 2R_1R_2R_3)\ e^{-2\alpha d}}\ .$$

Two approximations are made to simplify the determination of the optical absorption coefficient. First, we assume that reflection is constant with wavelength. Figure 3.5 shows a typical front reflection vs. wavelength plot which indicates that this is reasonable. Here the interference averaged reflectance varies from about 25% to 30%. Secondly, since R_1, R_2, and R_3 are not determined separately as a function of wavelength, we approximate the expression for transmittance as

$$T \simeq (1 - R)\ e^{-\alpha d}$$

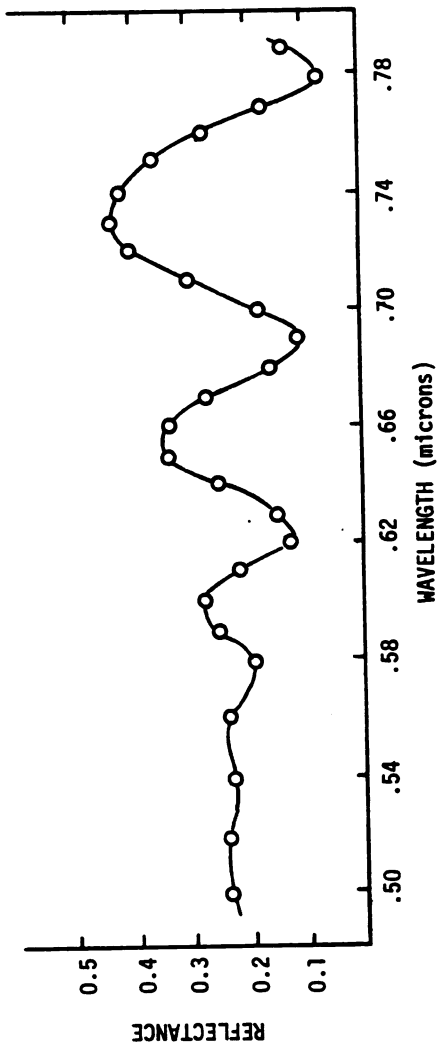

Figure 3.5 Typical reflectance vs. wavelength curve.

where

$$(1-R) = \frac{(1-R_1)\ (1-R_2)\ (1-R_3)}{1 - R_2R_3 - (R_1R_2+R_1R_3-2R_1R_2R_3)}$$

Defined in this way (1-R) is the value at which the interference averaged transmittance levels off at longer wavelengths, i.e. where α is small. For these approximations the uncertainty in α is small for $\alpha > 10^4$ cm^{-1} but increases rapidly for $\alpha < 10^3$ cm^{-1}. We will consider only values of α in the easily accessible range of 10^3 cm^{-1} to 10^5 cm^{-1} where it is estimated that the uncertainty in α is less than 10%.

We have observed the effects of varying the rf input power and hydrogen partial pressure on the optical absorption coefficient. Figure 3.6 shows the optical absorption coefficient vs. photon energy for three samples prepared at a hydrogen partial pressure of 0.8 mTorr and rf input power levels of 100 watts, 200 watts, and 300 watts. It is observed that the absorption edge shifts downward in energy for a fixed hydrogen partial pressure and increasing input power. Figure 3.7 shows that at a fixed input power level of 200 watts, the absorption edge can be shifted upward in energy by increasing the hydrogen partial pressure in the sputtering atmosphere. A more quantitative account of these absorption observations is contained in the next section.

3.3.2 Optical Energy Gap

A characteristic quantity called the optical energy gap may also be obtained from optical absorption measurements. An expression for α

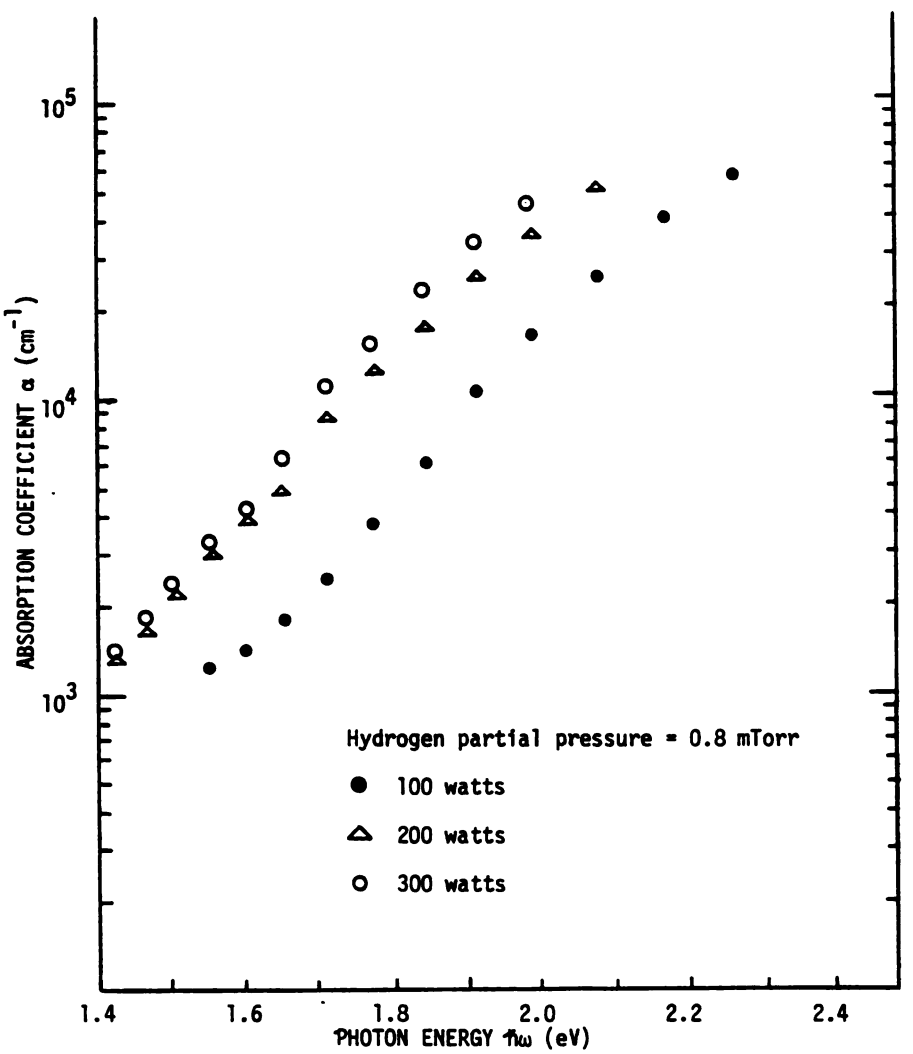

Figure 3.6 Absorption coefficient vs. photon energy for constant hydrogen partial pressure and varying power.

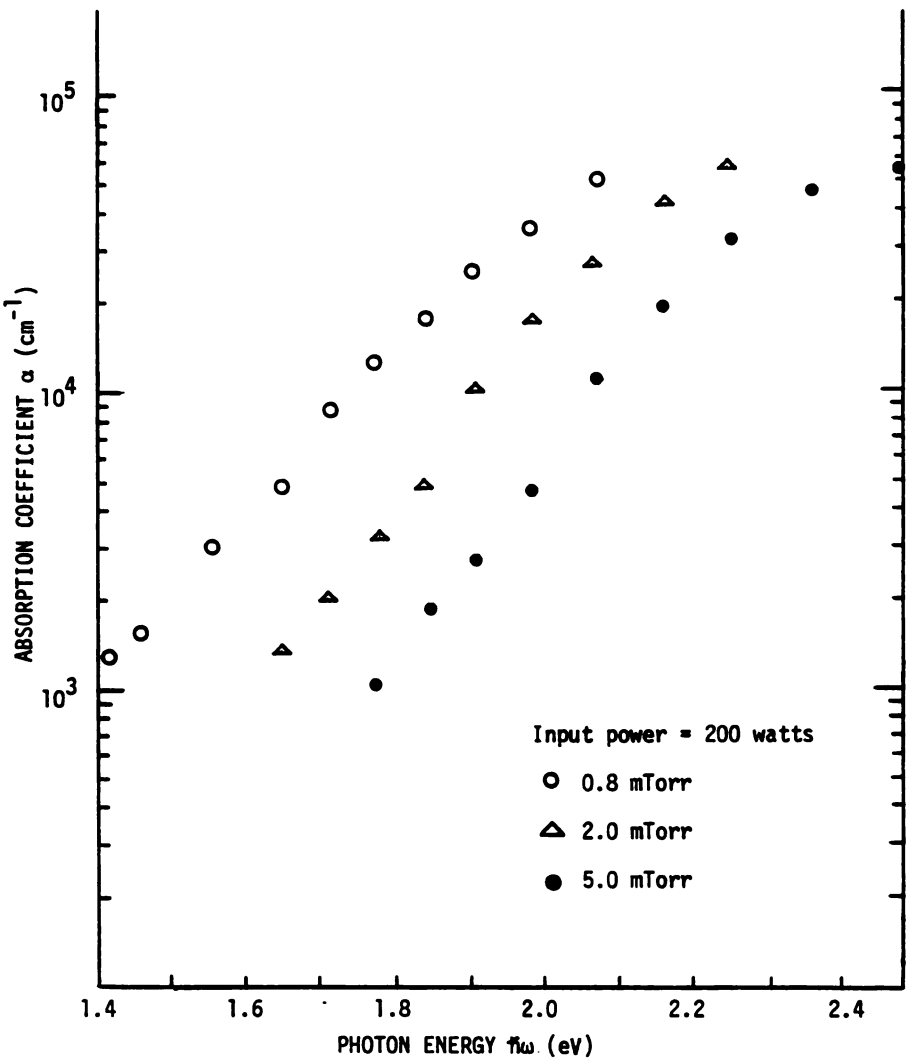

Figure 3.7 Absorption coefficient vs. photon energy for constant input power and varying hydrogen partial pressure.

may be obtained by considering the photon excitation of electrons from a full valance band with density of states g_v to an empty conduction band with density of states g_c as shown in Figure 3.8(a)[31]. Here E is the energy of the electron in the final state in the conduction band and $-E_{og}-E'$ is the energy of the electron in the initial state in the valence band. The bottom of the conduction band, E_c, is taken as the zero of energy. Conservation of energy requires that $\hbar\omega = E_{og} + E + E'$. For a fixed E' and photon beamwidth $d\omega$, the number of states in the conduction band in the interval between which transitions may take place from a state at E' is, following Smith, [32]

$$N_c(E)dE = g_c(E)dE = g_c(\hbar\omega-E_{og}-E')\hbar d\omega.$$

To find the total number of pairs of states between which transitions may take place, $N(\omega)$, we must integrate with respect to E' over the valence band density of states,

$$N(\omega)d\omega = C\, d\omega \int_0^{E'_m} g_c(\hbar\omega-E_{og}-E')g_v(E')dE'$$

where $E'_m = \hbar\omega - E_{og}$ and C is a constant. The absorption coefficient α is proportional to $N(\omega)$ and a complete quantum-mechanical treatment shows that

$$\alpha = \frac{C'}{\hbar\omega} \int_0^{E'_m} g_c(\hbar\omega-E_{og}-E')g_v(E')dE'$$

where C' is a constant.[32]

Now if the density of states in the conduction and valence bands is assumed to be parabolic, i.e., $g_c(E) = aE^{\frac{1}{2}}$ and $g_v(E') = a'E'^{\frac{1}{2}}$ then

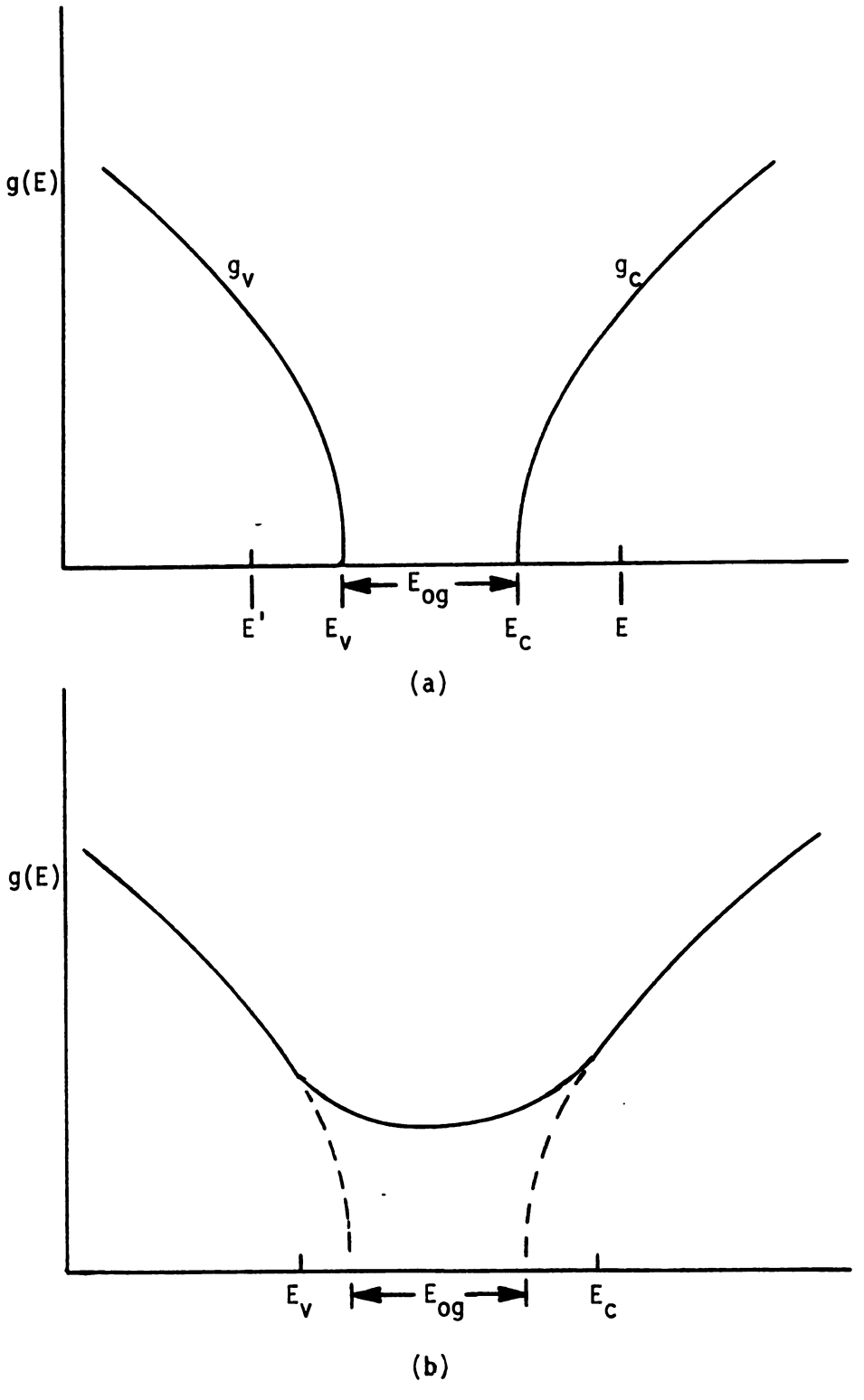

Figure 3.8 Density of states for defining optical energy gap E_{og}.

$$\alpha\hbar\omega = F \int_0^{E'} m(\hbar\omega - E_{og} - E')^{\frac{1}{2}} E'^{-\frac{1}{2}} dE'$$

where F is a constant. Evaluating this integral yields

$$\alpha\hbar\omega = F (\hbar\omega - E_{og})^2$$

from which E_{og} is defined as the optical energy gap. In amorphous materials, defining an optical gap does not mean there is a region where the density of states is zero. Rather a more likely interpretation is that E_{og} is representative of the energy which separates the extrapolated limits of the extended states in the valence band and the extended states in the conduction band. There are still tail states and localized defect states in between so that the density of states never goes to zero in the so called pseudogap (Figure 3.8(b)). In fact, there is no definitive interpretation of E_{og} in amorphous materials. Nevertheless, it is a useful measure for comparison purposes.

For a semiconductor with parabolic, or nearly parabolic, bands the optical gap may be found from measurements of the absorption coefficient by extrapolation of a plot of $(\alpha\hbar\omega)^{\frac{1}{2}}$ vs. $\hbar\omega$ to zero absorption. The intercept with the $\hbar\omega$ axis gives E_{og}. The experimental data indicate a good approximation of the above equation for large absorption ($\alpha > 10^4$ cm^{-1}) and a poor approximation at lower absorption. This is not surprising since energetic carriers with energy much greater than the pseudogap will only be slightly affected by long range fluctuations in the potential. For such carriers then, the difference in amorphous and crystalline states should not be very great. For lower energies the tail states and localized gap states

will have a significant effect and α will no longer follow a relation as given above.

Figure 3.9 shows $(\alpha\hbar\omega)^{\frac{1}{2}}$ vs. $\hbar\omega$ for samples prepared at a fixed hydrogen partial pressure of 0.8 mTorr and varying rf input power levels of 100 watts, 200 watts, and 300 watts. The optical gap decreases for increasing power although there is only a small difference between the optical gap at 200 watts and 300 watts. Figure 3.10 shows $(\alpha\hbar\omega)^{\frac{1}{2}}$ vs. $\hbar\omega$ for samples prepared at a fixed input power of 200 watts and hydrogen partial pressures of 0.8 mTorr, 2.0 mTorr, and 5.0 mTorr Over this range it is observed that the optical gap is monotonically increasing with hydrogen partial pressure. Since E_{og} increases for increasing hydrogen content, the data show that film hydrogenation increases with the hydrogen partial pressure, as expected, and decreases with increasing power.

An explanation of the decreasing gap with increasing power requires an understanding of how and where hydrogenation of the silicon film takes place. Three possible mechanisms may be hypothesized. Firstly, the target may become hydrogenated which could lead to sputtering of SiH_x molecules directly from the target. Secondly chemical reactions of the form

$$Si + H_x \rightarrow SiH_x$$

may occur in the plasma. Finally,the above reaction may take place as a surface reaction on the substrate which is in constant contact with the plasma. Unfortunately,a definitive answer as to the role of these three mechanisms does not exist in the literature. Indeed the

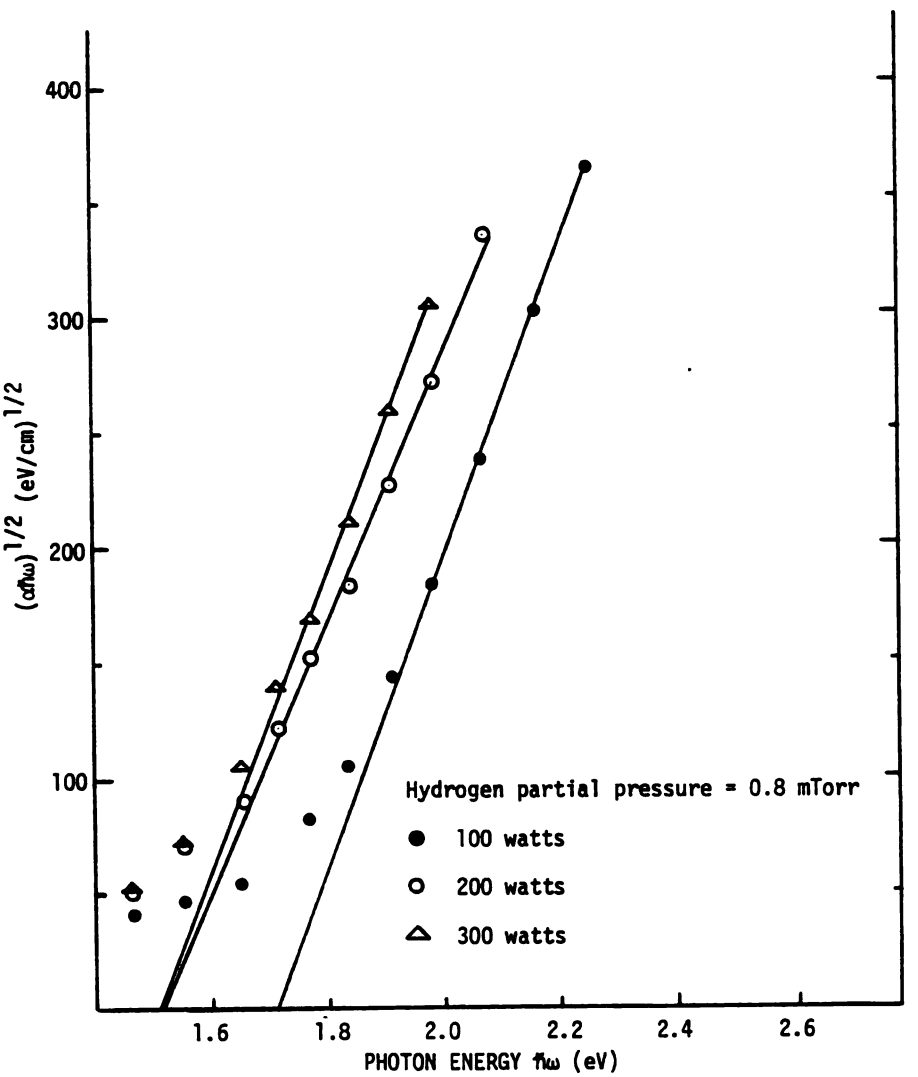

Figure 3.9 $(\alpha\hbar\omega)^{1/2}$ vs. photon energy for constant hydrogen partial pressure and varying power.

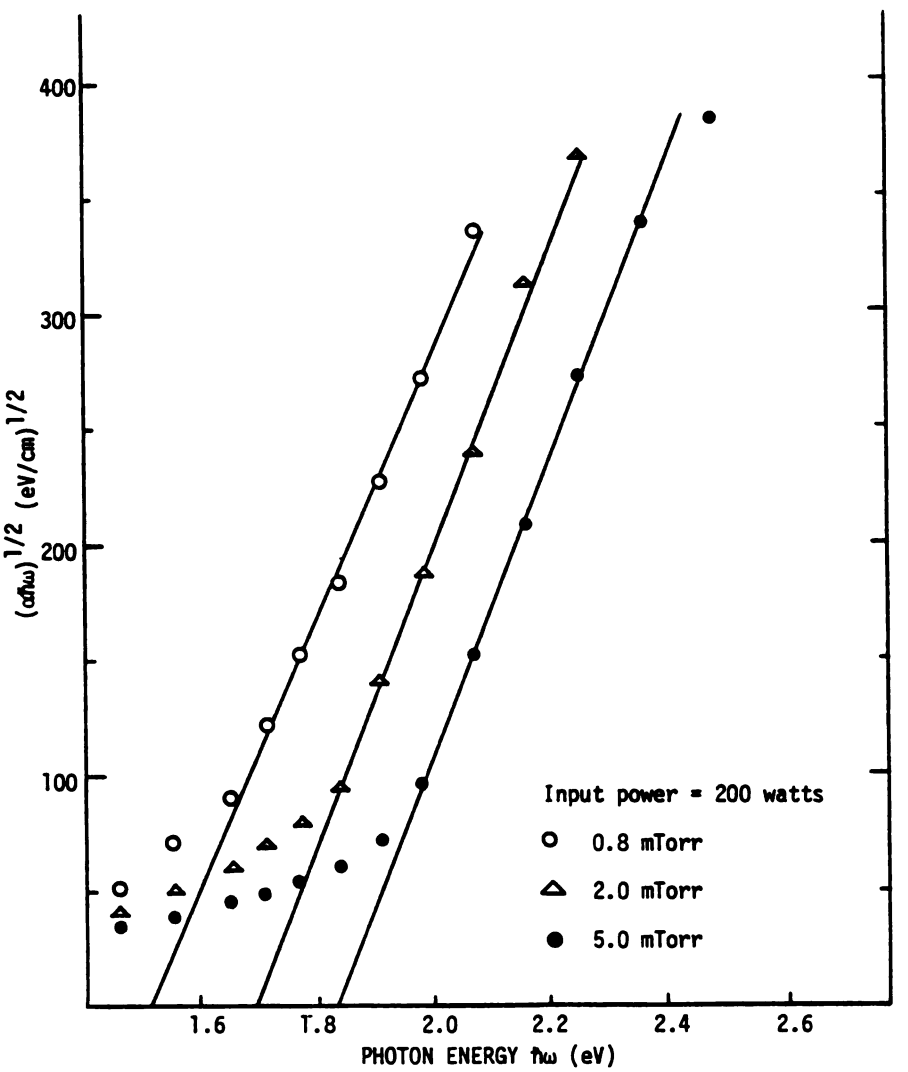

Figure 3.10 $(\alpha\hbar\omega)^{1/2}$ vs. photon energy for constant input power and varying hydrogen partial pressure.

relative roles may vary with system design and deposition parameters.

Our power dependent gap observation is consistent with the plasma interaction model. Increasing power leads to higher velocities and decreasing cross sections. However, this single observation is not taken as definitive proof for plasma chemical reactions predominately accounting for film hydrogenation.

3.3.3 Infrared Transmission

It has been known for some time that hydrogen incorporated into amorphous silicon is primarily responsible for its rather remarkable properties among amorphous semiconductors. More recently it has been discovered that hydrogen bonds into the network in several different configurations depending upon the preparation conditions. Furthermore, the type of hydrogen bonding present can apparently effect such important semiconductor properties as carrier mobility and carrier lifetime. One of the most direct ways to investigate the local environment of hydrogen bonds in an amorphous silicon network is to observe the infrared vibrational absorption spectra. Several groups have studied the absorption spectra and analyses have identified the observed characteristic absorption bands to be due to stretching, bending and wagging vibrational modes of either monohydride bonds (one of four tetrahedral bonding sites of a silicon atom occupied by a hydrogen atom); dihydride bonds (two sites filled by hydrogen atoms), or trihydride bonds (three sites filled by hydrogen atoms).[15,18,33] Figure 3.11 illustrates schematically the various vibrational modes and the peak absorption energies associated with each.

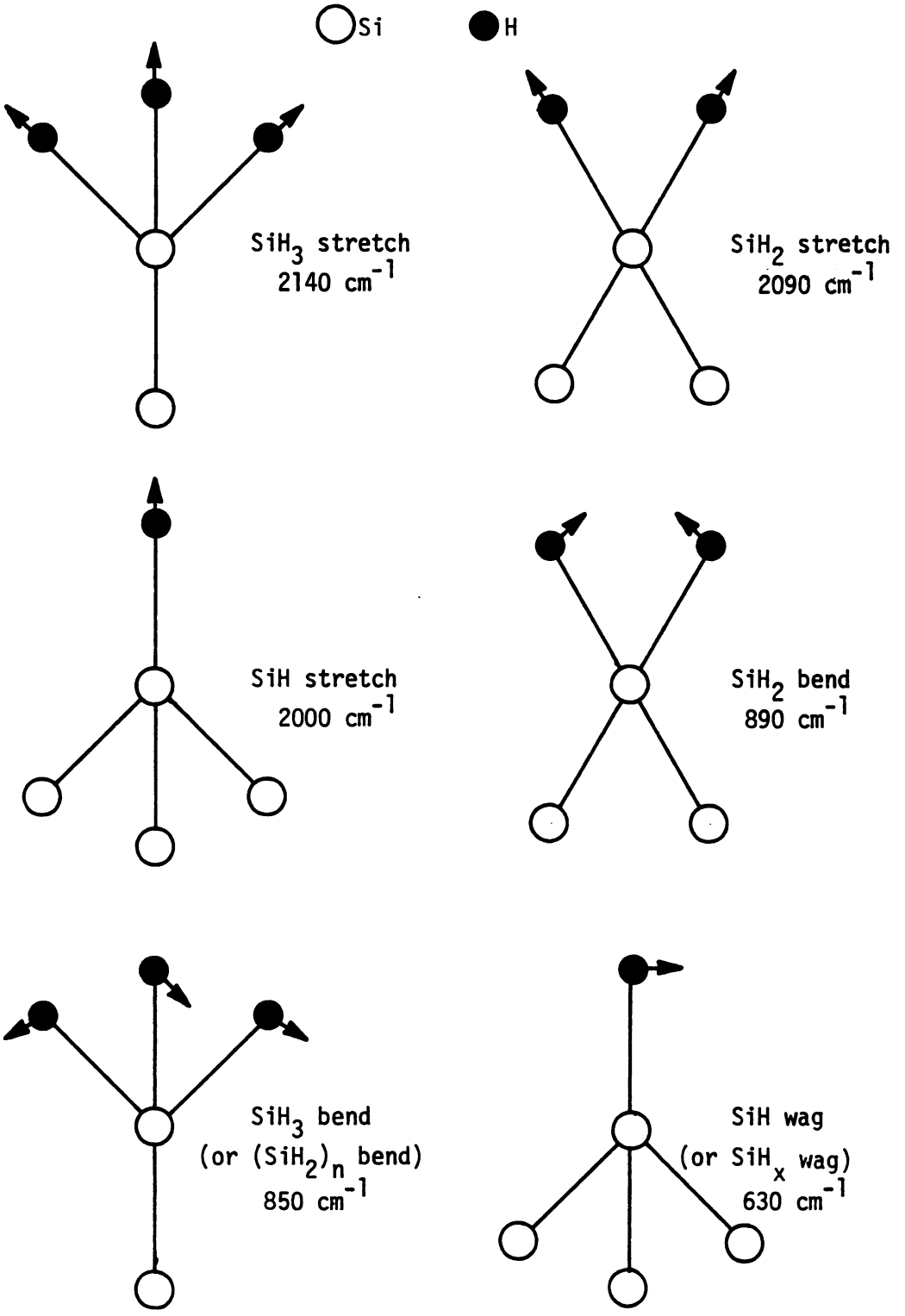

Figure 3.11 Silicon-hydrogen IR vibrational modes and peak absorption energies.

Initially we proposed a study of the effects of sputtering input parameters on the vibrational absorption spectra of our films with the intention of optimizing the deposition conditions to favor predominately monohydride bonding which is associated with higher photoconductivity and better general semiconductor properties. However, a more important result of this study turned out to be the ability to detect impurities unintentionally incorporated into the films and subsequently identifying the source of these impurities.

As previously mentioned, infrared transmission samples are prepared on crystalline silicon substrates. Crystalline silicon substrates have several advantages. Among them are: (1) sufficient transparancy to IR radiation over the range of interest, (2) a refractive index close to that of amorphous silicon, therefore, interference fringes from multiple reflections are minimized, (3) a thermal expansion coefficient close to that of amorphous silicon so that thick films do not detach from the substrates upon cooling. Amorphous silicon films for IR samples are deposited at a rf input power of 200 watts, substrate temperature of 250^{o} C, and argon partial pressure of 5 mTorr. Hydrogen partial pressure is the variable input parameter and is varied from 0.8 mTorr to 5.0 mTorr. Samples are sputtered for 8 hours yielding films 5 to 7 microns thick. The infrared transmission spectra are obtained using a Perkin-Elmer model 457 double beam grating IR spectrophotometer. Transmission of samples are measured relative to an uncoated substrate placed in the reference beam. Figure 3.12 shows the initial results of IR transmission for three samples prepared at hydrogen partial pressures of 0.8 mTorr, 2.0 mTorr, and 5.0 mTorr.

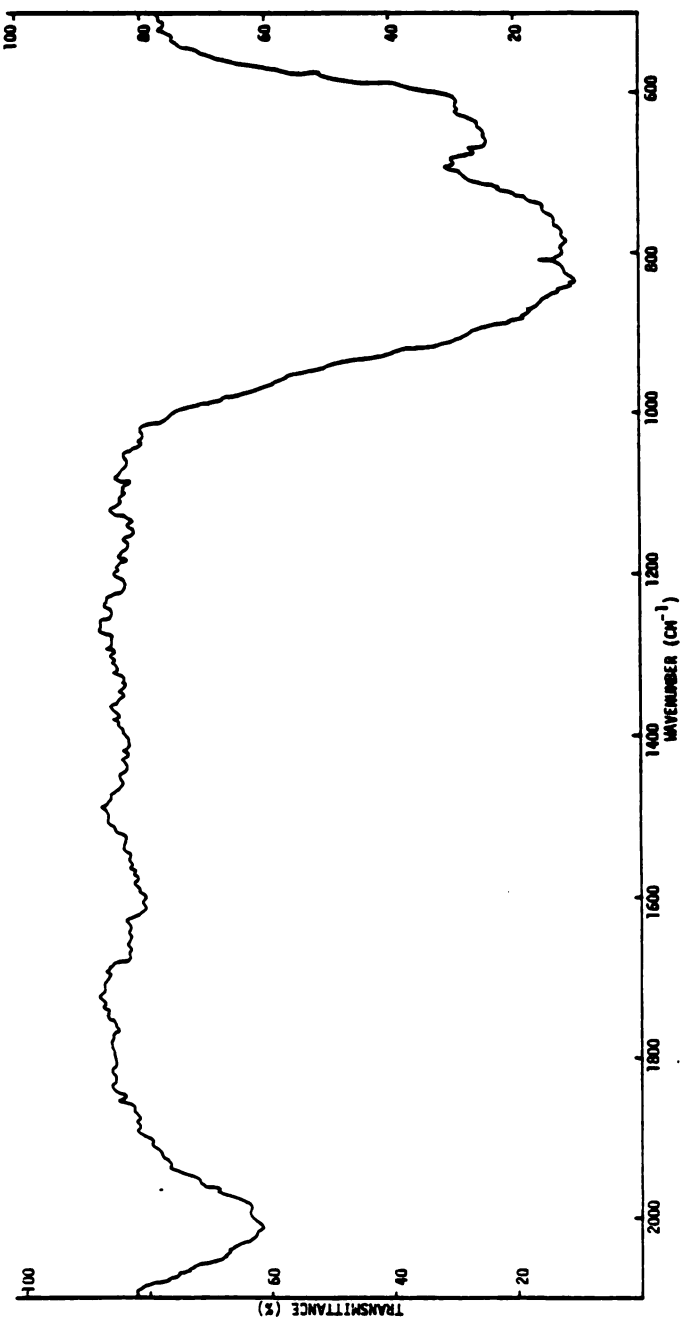

Figure 3.12(a) IR transmittance of 0.8 mTorr hydrogen partial pressure sample (98.6% pure sputtering atmosphere).

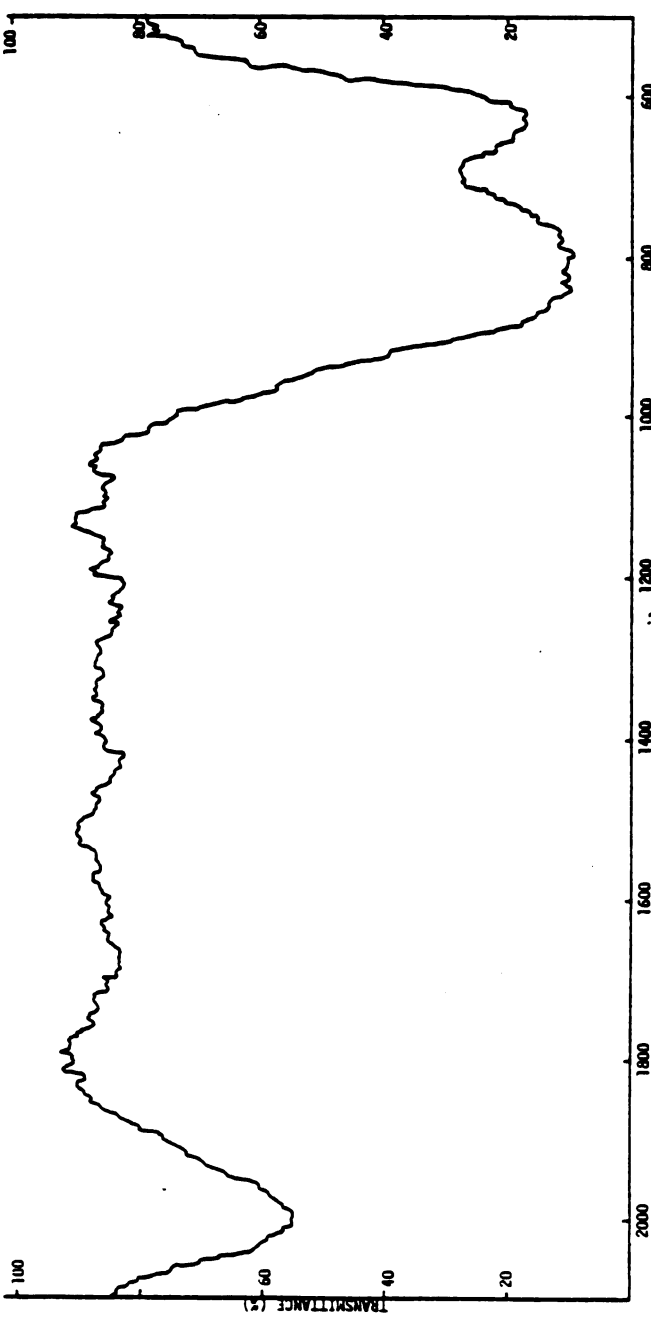

Figure 3.12(b) IR transmittance of 2.0 mTorr hydrogen partial pressure sample (98.6% pure sputtering atmosphere.

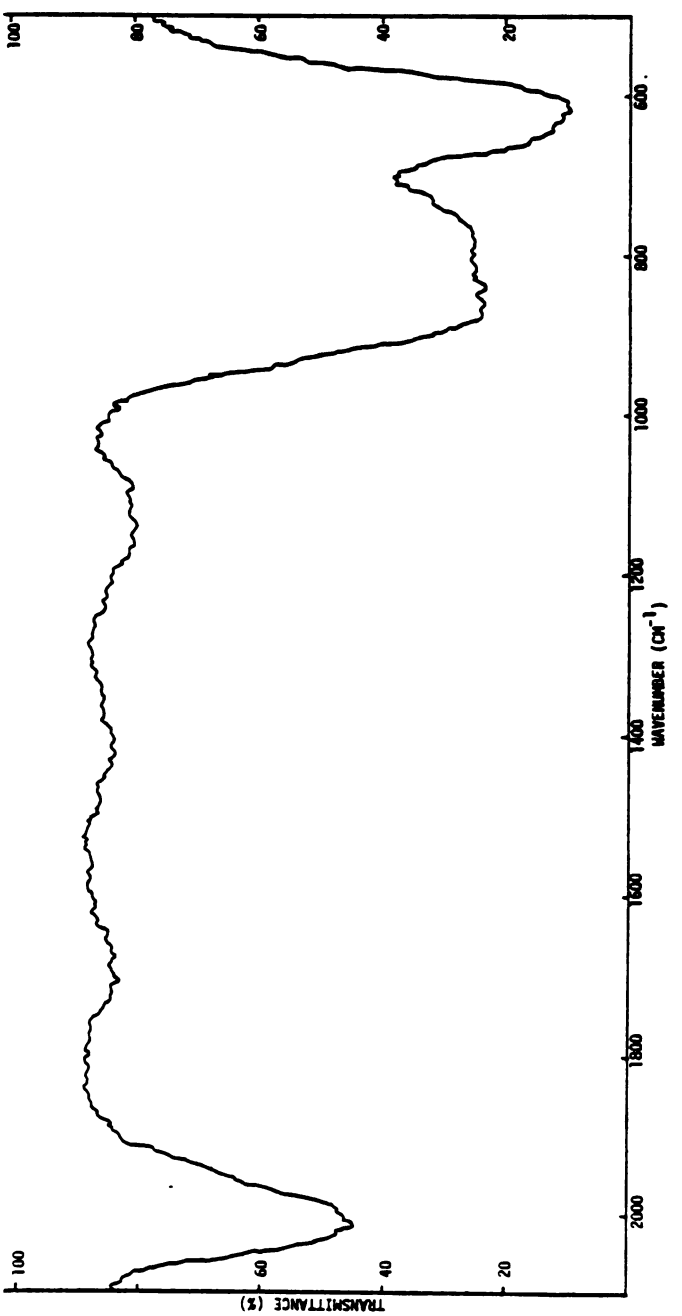

Figure 3.12(c) IR transmittance of 5.0 mTorr hydrogen partial pressure sample (98.6% pure sputtering atmosphere.

There are three distinct absorption bands present for all three films. Two of these, one centered near 2000 cm^{-1} and one centered near 630 cm^{-1}, may be associated with hydrogen bonded into the network in either the monohydride or dihydride bonding configuration. However, the third rather broad band extending from approximately 1050 cm^{-1} to 650 cm^{-1} is unidentified and is suspected of arising from unintentionally incorporated impurities. There are several places these impurities may originate from. Among them are: (1) the epoxy which holds the target in place, (2) the teflon ground shield spacer, (3) residual impurities in the argon or hydrogen sputtering gas (99.99% pure), (4) absorbed impurities in the target, (5) contamination by diffusion pump oil, and (6) air leaks in the vacuum system. Several of the above sources were eliminated from consideration by sputtering a sample in pure argon after removing the epoxy from the target, removing the teflon ground shield spacer from the chamber, and extensively sputter cleaning the target for several hours. Figure 3.13(a) shows the results of such a sample. Of course the absorption bands due to hydrogen bonding have disappeared but the broad impurity band remains.

A close look into the quality of the vacuum system lends some important insight into the purity of the sputtering atmosphere. Comparing the base pressure of the vacuum system prior to sputtering (2×10^{-6} Torr) to the chamber pressure during sputtering (5×10^{-3} Torr), the initial purity at the beginning of a sputtering run is 99.96%. However, comparing the measured flow rate of sputtering gas through the system at 5 mTorr (1.7×10^{-2} scc/sec) to the measured leak rate into the system (2.3×10^{-4} scc/sec), the purity of the sputtering

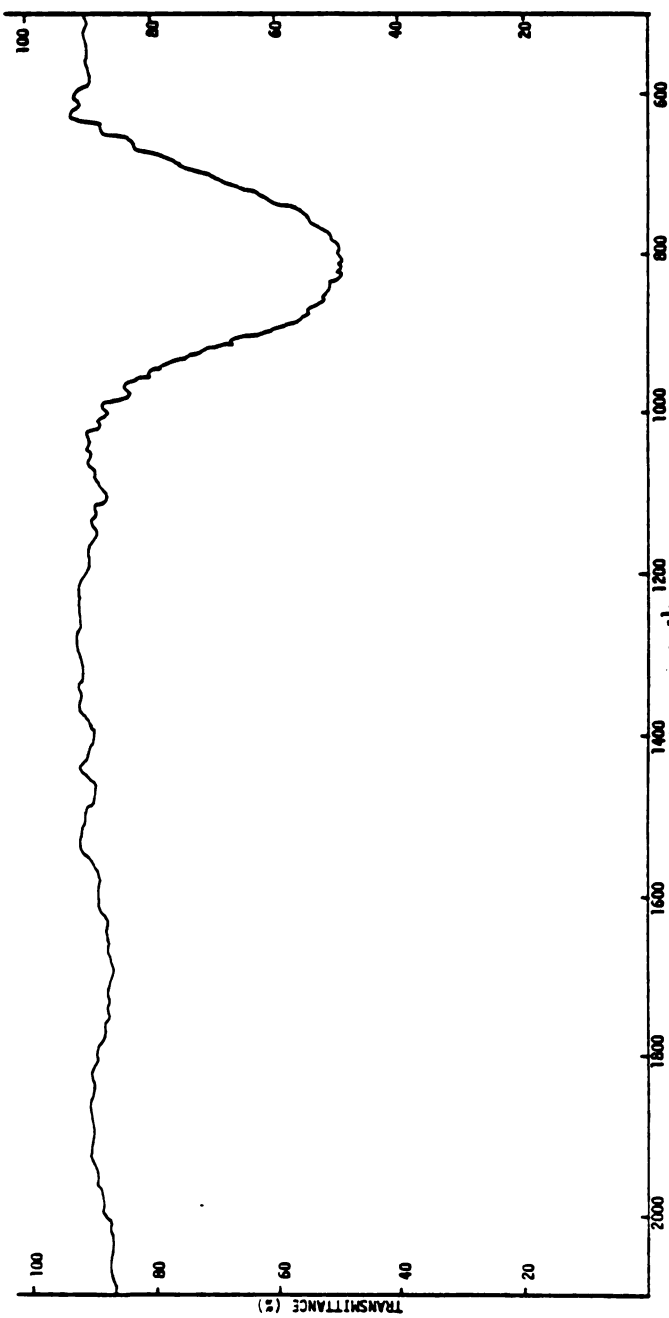

Figure 3.13(a) IR transmittance of non-hydrogenated sample (98.6% pure sputtering atmosphere.

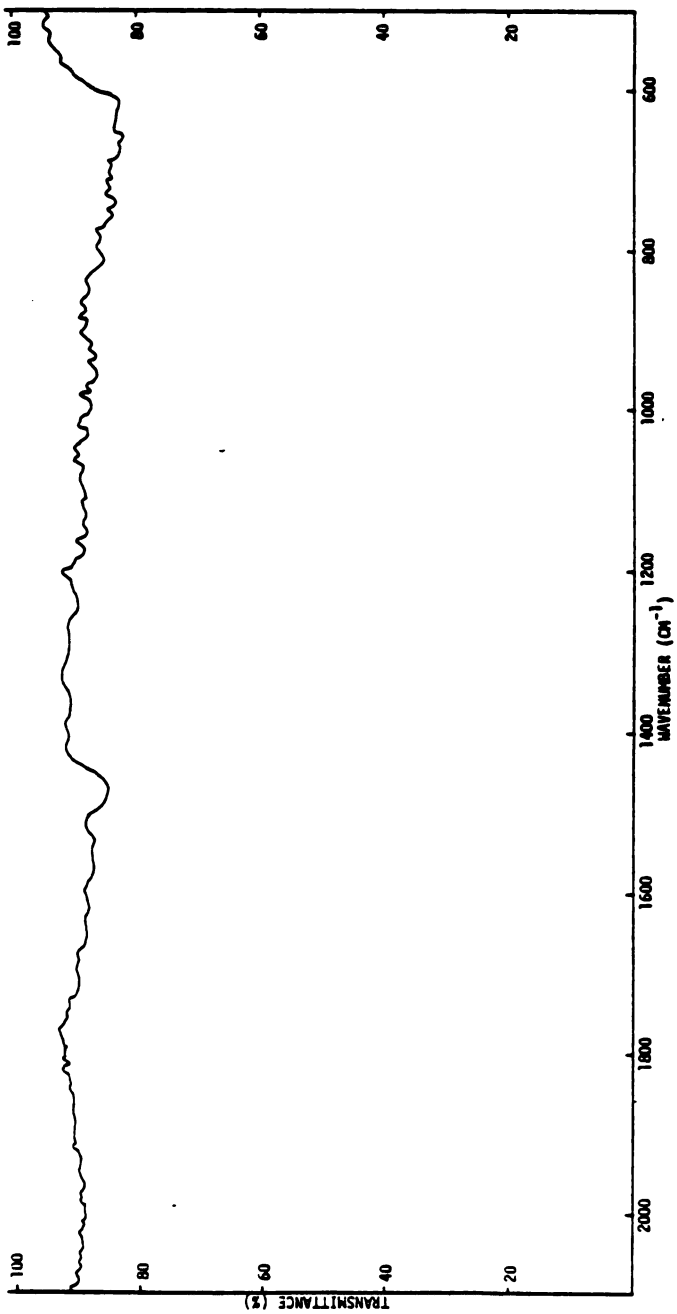

Figure 3.13(b) IR transmittance of non-hydrogenated sample (99.98% pure sputtering atmosphere).

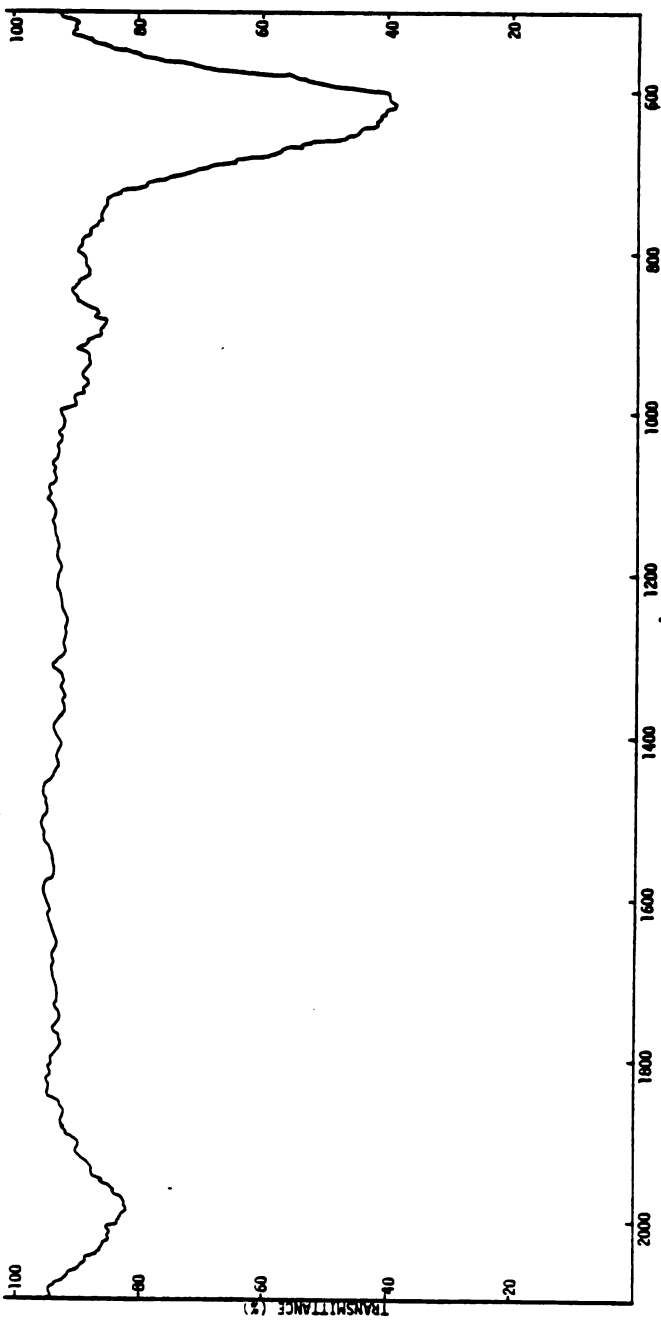

Figure 3.14 IR transmittance of 0.8 mTorr hydrogen partial pressure sample (99.98% pure sputtering atmosphere).

atmosphere in the steady state is reduced to only 98.6%. Furthermore, steady state is achieved in approximately one minute. In light of this result, an effort was made to improve the leak rate into the system. An improvement of two orders of magnitude, to 3×10^{-6} scc/sec, was possible. This results in a purity of 99.98% (nearly equivalent to the cylinder gas purity) even in the steady state. Another non-hydrogenated sample was prepared in this low leak system and the results are shown in Figure 3.13(b). It is obvious that the impurity band has disappeared and the conclusion is the origin of the film contamination was an air leak into the system. Figure 3.14 shows the results of an IR transmission measurement on a sample prepared at a hydrogen partial pressure of 0.8 mTorr in the low leak system. The predominate features of the absorption spectrum are the monohydride stretching mode at 2000 cm^{-1} and the 630 cm^{-1} wagging mode. There is some evidence of a weak band centered at 890 cm^{-1} and a shoulder on the 2000 cm^{-1} peak near 2090 cm^{-1} which indicates a low concentration of dihydride bonds. However, probably the most important feature is the absence of the broad impurity band in the 1050 cm^{-1} - 650 cm^{-1} region indicating that the concentration of unintentionally incorporated impurities is now below the detection level of this technique.

3.4 Electrical Properties

3.4.1 Temperature Dependence of Dark Conductivity

It is known that certain preparation conditions have dramatic effects on conduction processes in amorphous silicon. For example,

several atomic percent of hydrogen incorporated into amorphous silicon reduces the dark conductivity by many orders of magnitude. The reason for this is that hydrogen effects the density and distribution of states in the gap and also in the valence and conduction bands. A certain amount of control over this process is possible by varying the deposition parameters. This section describes the results of varying the hydrogen partial pressure in the sputtering atmosphere and the rf input power on the dark conductivity and the thermal activation energy.

A study of dark conductivity versus temperature provides information concerning the relative contribution of extended and localized states to transport phenomena. Normal band conduction in semiconductors is accomplished through extended states where the number of carriers in the bands is thermally activated and the conductivity may be expressed as

$$\sigma = \sigma_o e^{-E_a/kT}$$

where $E_a = E_c - E_f$ is defined as the activation energy for a non-activated mobility and σ_o is a relatively temperature independent constant. However, in amorphous silicon the mobility of electrons in extended states is likely determined by the thermal release of trapped electrons from states just below the extended state conduction band edge. In this case, mobility will be thermally activated, as well as carrier concentration, and also contribute to E_a.

Localized states, on the other hand, contribute to conductivity through phonon assisted hopping. That is, electrons tunnel from one

localized state to another with the emission or absorption of a phonon. LeComber, Madan, and Spear suggest that there are two distinct groups of localized states.[34] Refering to Figure 3.15, one distribution of localized states adjoins the extended states between E_c and E_A and between E_B and F_v and is associated with the lack of long range order in an amorphous semiconductor. These states are sometimes called tail states. The second group of localized states between E_A and E_B are associated with structural defects within the amorphous network. The phonon assisted hopping mobility is given by an expression of the form

$$\mu_H = \mu_{HO} e^{-W/kT}$$

where μ_{HO} is a relatively temperature independent constant and W is the difference in the energies of the two localized states. If hopping takes place near an energy E_x, the hopping conductivity may be expressed as

$$\sigma = \sigma_{HO} e^{-\frac{(E_x - E_f) + W}{kT}}$$

where σ_{HO} is a constant depending on the density of states, the average hopping distance, and the phonon frequencies involved. When extended states dominate conduction, the pre-exponential term is relatively large, typically 100 $(\Omega\text{-cm})^{-1}$ or more. When hopping dominates, the pre-exponential term is typically much less than unity.

The experimental set-up for measuring dark conductivity versus

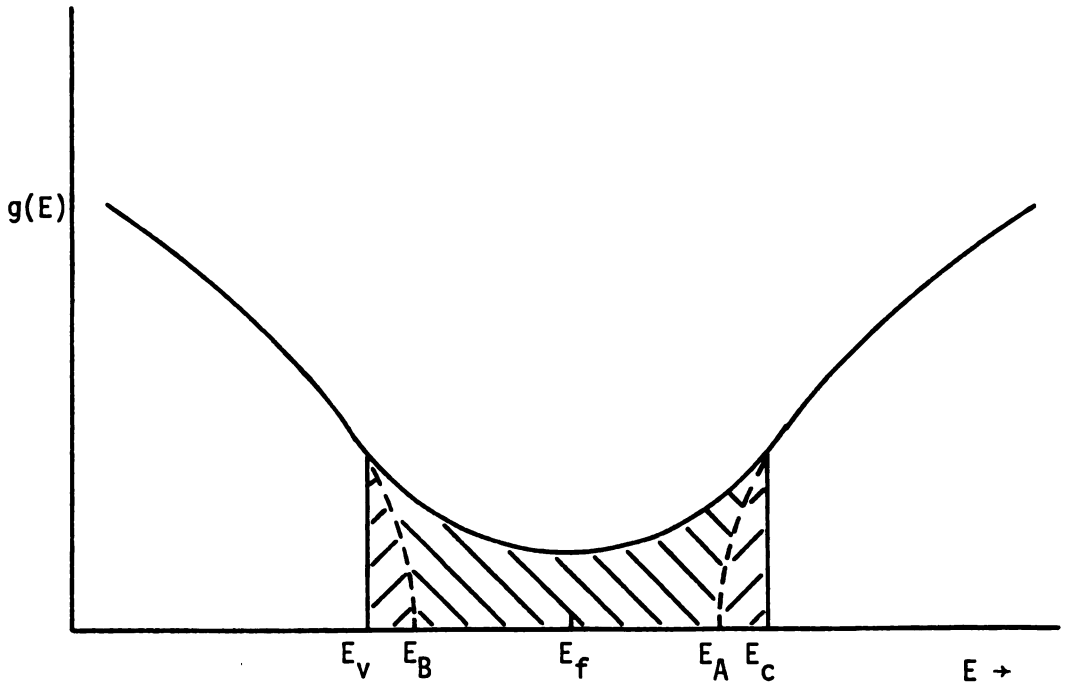

Figure 3.15 Density of states for an amorphous semiconductor showing two distinct groups of localized states.

temperature is shown in Figure 3.16. Samples are prepared in the sandwich geometry with a molybdenum bottom contact sheet and circular top molybdenum contacts. Conductivity is determined by measuring current versus voltage assuming ohmic contacts. This is a reasonable assumption considering the I-V characteristics differ from linear behavior by only about 10% over the range of applied fields (2.5×10^3 - 5.0×10^3 V/cm). A Micro-Technical Industries Thermo-Probe is used to heat the aluminum platform on which the sample rests. Temperatures from 25^o C to 200^o C are investigated. Measurements are taken in a dark room with the sample enclosed in a glass box filled with dry nitrogen to reduce leakage current effects.

Figures 3.17 and 3.18 show the results of dark conductivity versus inverse temperature for different preparation conditions. Straight lines can be drawn through most of the data points over limited regions, indicating activated conduction via one of the mechanisms described above. However, it is not trivial to differentiate between which transport mechanism is dominating. Two alternative models are offered here for consideration.

One interpretation is that all the films show extended state conduction with activation energies ranging from 0.50 eV to 0.71 eV and pre-exponential terms ranging from 0.7 $(\Omega\text{-cm})^{-1}$ to 220 $(\Omega\text{-cm})^{-1}$. In the lowest conductivity samples, 5 mTorr hydrogen and 2 mTorr low leak rate hydrogen, and 200 watts input power, a hopping mechanism is observed for temperatures less than about 100^o C. Hopping is not observed in the other samples because the higher extended state conductivity dominates. E_f is farthest from E_c for the low conductivity

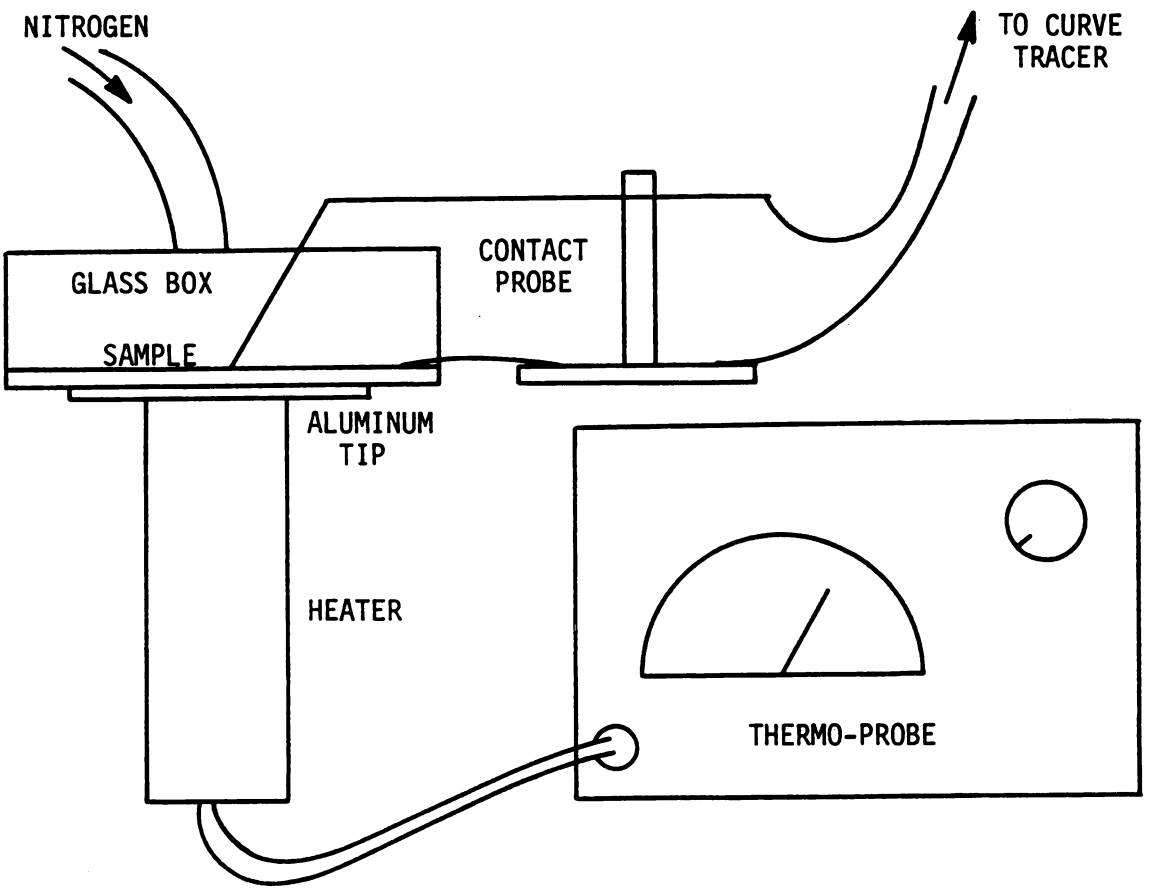

Figure 3.16 Experimental setup for measuring conductivity vs. temperature.

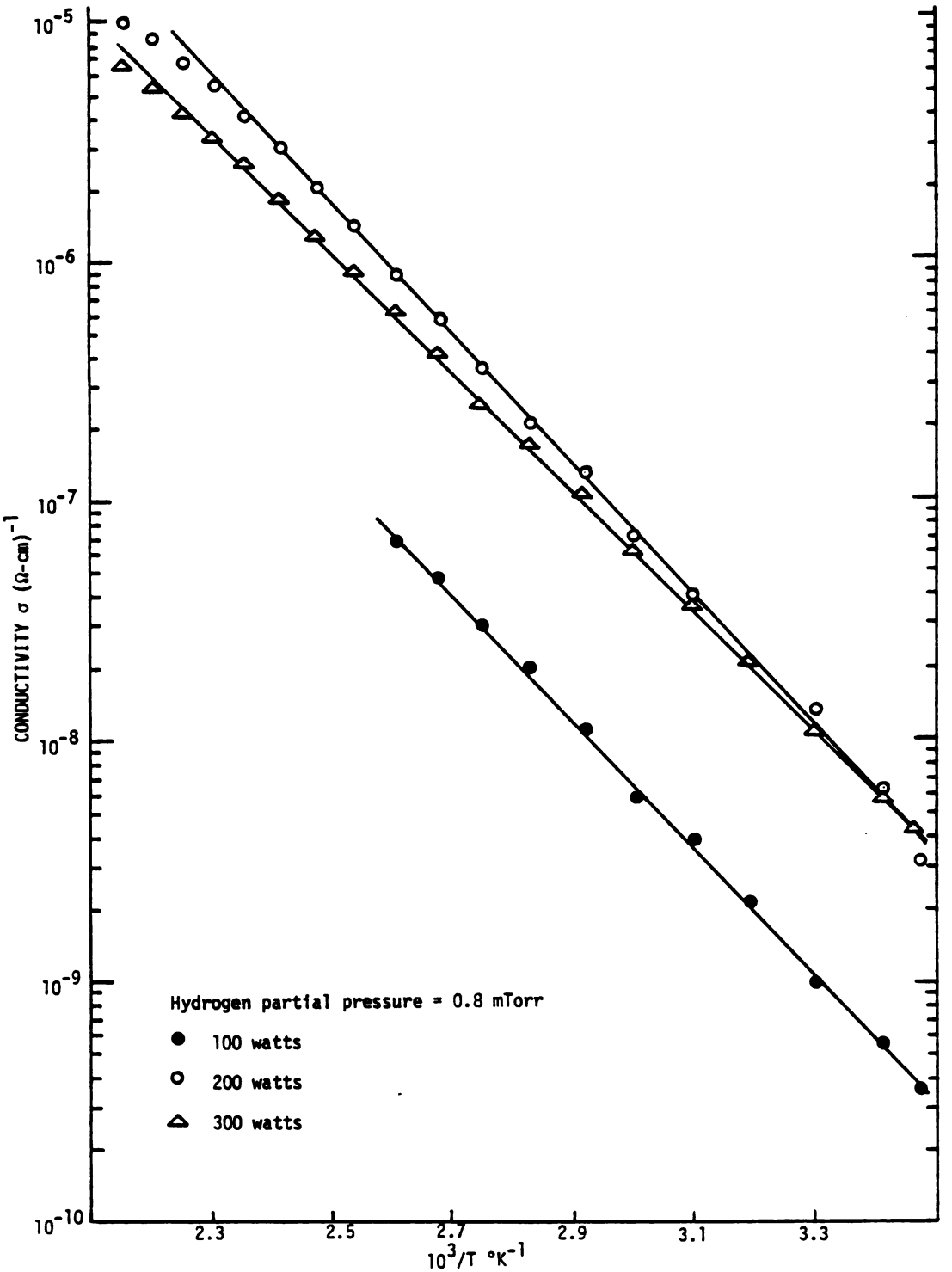

Figure 3.17 Conductivity vs. inverse temperature for constant hydrogen partial pressure and varying power.

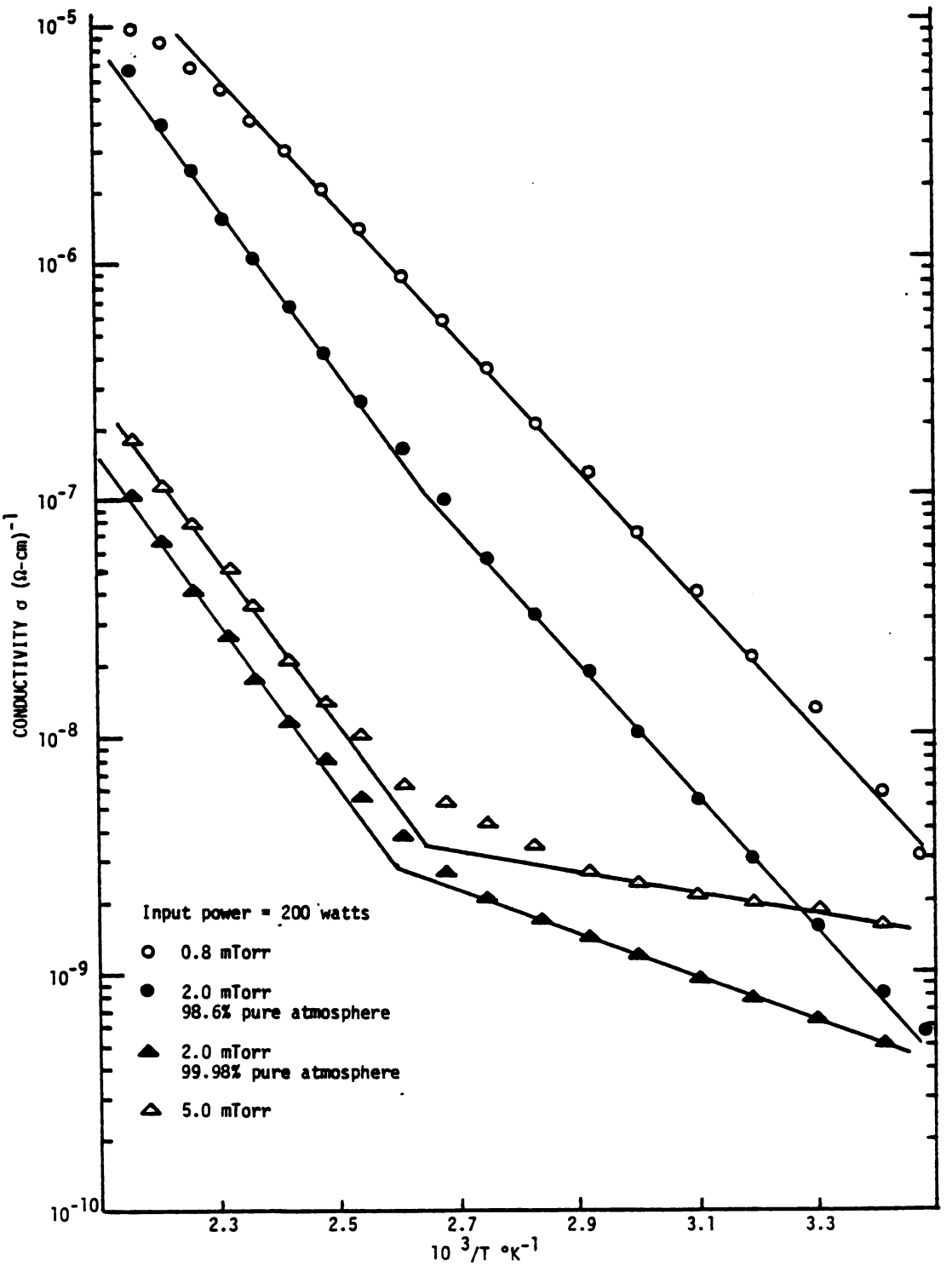

Figure 3.18 Conductivity vs. inverse temperature for constant input power and varying hydrogen partial pressure.

samples. Such a maximum in $E_c - E_f$ has also been argued for by Moustakas in support of photoconductivity measurements versus hydrogen partial pressure.[35] The Harvard group also reports a transition from extended state to hopping conduction, but at 80^o C.[18]

An argument against this model is the relatively low values for the pre-exponential term. For example, the Harvard group report σ_o as greater than 1000 $(\Omega\text{-cm})^{-1}$ with E_a being 0.8 eV to 0.9 eV for $T > 80^o$ C. Our lower pre-exponential terms may indicate a lower mobility. In fact, our $\mu\tau$ products are on the lower end of reported values as will be discussed later in this chapter.

Another interpretation is that only three of the films exhibit extended state conduction at all. These are the films prepared at 200 watts (Figure 3.18) with hydrogen partial pressures of 2.0 mTorr (with both high and low leak rates into the vacuum system) and 5.0 mTorr. Again above 100^o C these films are conducting via extended states characterized by the largest activation energy of approximately 0.7 eV and pre-exponential terms on the order of 10 $(\Omega\text{-cm})^{-1}$ or greater. Below 100^o C hopping conduction takes over, but now two separate hopping mechanisms must be involved. In the 5.0 mTorr hydrogen partial pressure sample and the 2.0 mTorr hydrogen pressure, low leak rate sample, the hopping is taking place deep in the gap near the Fermi level as characterized by small activation energies of 0.10 eV and 0.18 eV and by pre-exponential terms very much less than unity. The other 2.0 mTorr hydrogen partial pressure sample below 100^o C is characterized by an activation energy of 0.56 eV and an intermediate pre-exponential term of 3.3 $(\Omega\text{-cm})^{-1}$. This is indicative

of hopping through states near the bottom of the tail states. All the other films are singly activated over the range of temperatures investigated with activation energies and pre-exponential terms characteristic of hopping through the tail state distribtuion. In this model these hopping states in the tail are eliminated by going to a low leak, 2 mTorr hydrogen deposition, or to a very high hydrogen partial pressure of 5 mTorr. A counter argument to this model is that leaks and/or hydrogen passivation might be expected to affect deep gap states rather than tail states.

Although the dark conductivity data does not seem to be sufficient to uniquely support one of the two models, there is a common ground. In any case, both extended state and hopping conduction are observed with the transition temperature depending on deposition parameters. As is discussed later in the chapter, photoconductivity results tend to support the first model.

3.4.2 Photoconductivity and Mobility-Lifetime Product

When photons of sufficient energy are incident on a semiconductor there is a certain probability that some will be absorbed and excite electrons from the valence band to the conduction band creating hole-electron pairs. These photo-generated carriers have a mean free lifetime during which the electrical conductivity increases. A study of photoconductivity in amorphous silicon, then, is a promising approach to a better understanding of the nature of free carrier recombination in these films. In this section, results of photoconductivity experiments are presented to study the effect of sample preparation

conditions on measures of photoconductivity. Also the mobility-lifetime products ($\mu\tau$) for these films are calculated from the photoconductivities using a technique developed to handle the case of non-uniform illumination.

Samples are prepared in two configurations; a coplanar gap cell geometery with a 0.4 mm spacing between contacts and a sandwich geometry with 1.6 mm diameter circular top contacts and semitransparent bottom contact sheet. The sandwich samples are the same ones used for dark conductivity measurements as described in Section 3.4.1. The photon source is a Bausch and Lomb grating monochrometer. The photon flux out of the monochrometer has been calculated using the manufacturers calibration curves, transmittance curves for the low pass filters employed, and the beam area. Light meter measurements were used to check these calculations. The gap cell samples are mounted vertically and illuminated directly (Figure 3.19(a)), whereas the sandwich samples are mounted horizontally and illuminated through the semitransparent bottom contact using a mirror (Figure 3.19(b)). Dark currents and currents under illumination are measured with a Tektronix 577 curve tracer in the dc mode and are approximately linear for electric fields in the 2.5×10^3 - 5.0×10^3 V/cm range investigated. The photoconductivity ($\Delta\sigma_p$) is calculated as the difference between the conductivity under illumination (σ_L) as determined from the light current, and the dark conductivity (σ_D) as determined from the dark current, i.e.,

$$\Delta\sigma_p = \sigma_L - \sigma_D$$

Figure 3.20 shows the photoconductivity results for gap cell samples prepared with different hydrogen content in the sputtering atmosphere.

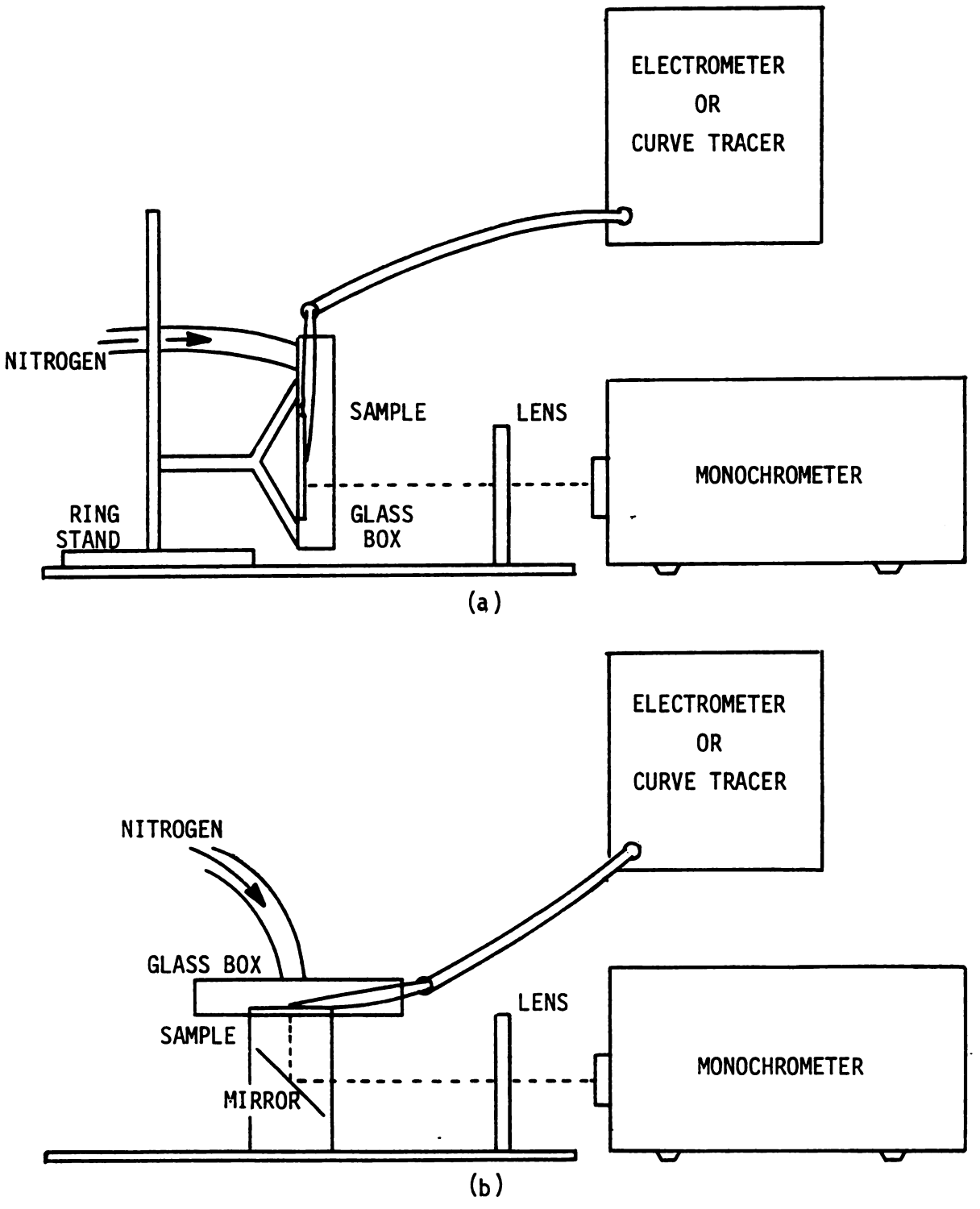

FIGURE 3.19 Experimental setup for measuring photoconductivity.

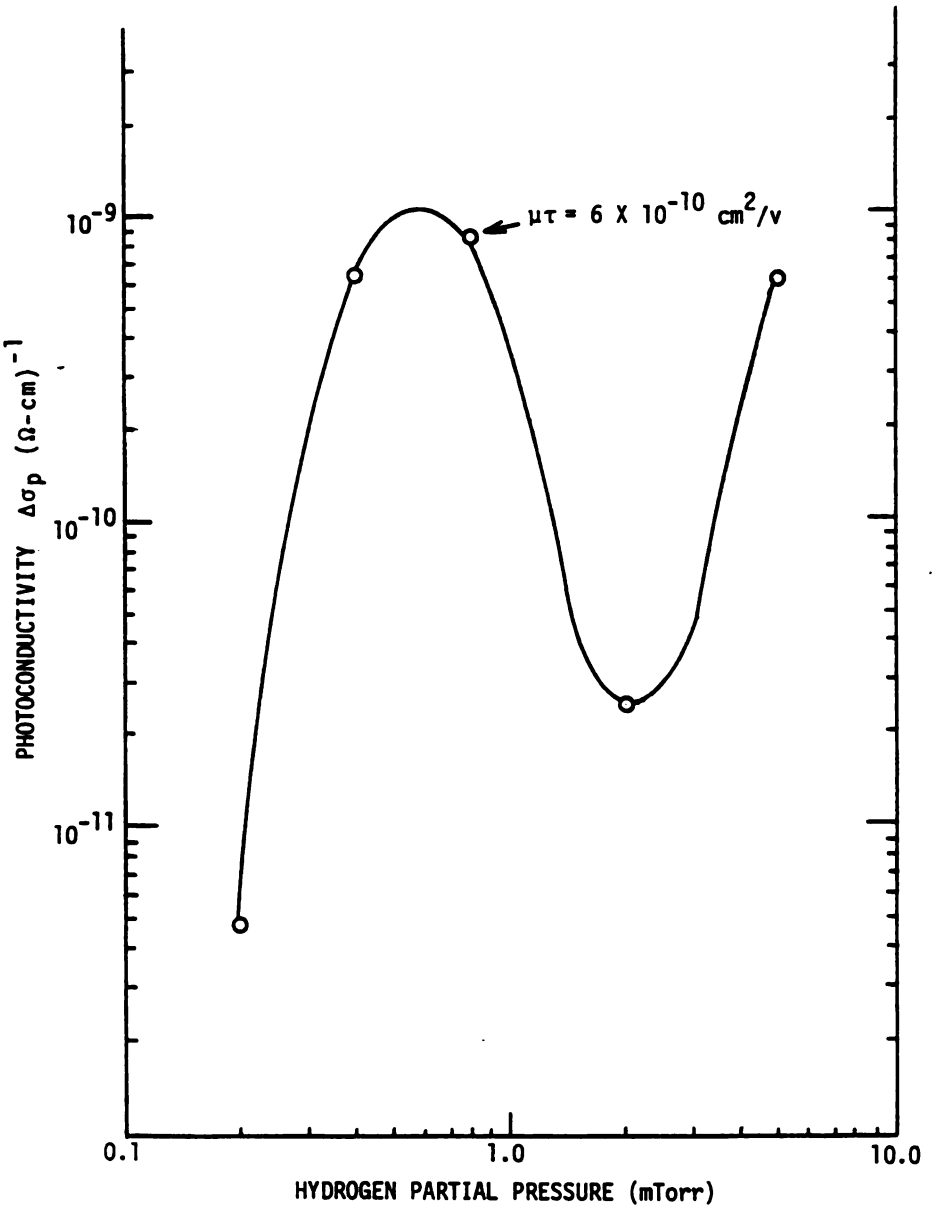

Figure 3.20 Photoconductivity vs. hydrogen partial pressure.

The rf input power is 100 watts and the total pressure is 20 mTorr except for the highest hydrogen partial pressure of 4.9 mTorr for which the total pressure was 24 mTorr. A peak in photoconductivity at low partial pressures of hydrogen followed by a second increase in photoconductivity at higher partial pressures has been previously reported by Moustakas et al.[36] It has also been reported that this minimum disappears when oxygen is purposely incorporated into the films.[37] The fact that we observe a peak in photoconductivity at low partial pressures of hydrogen is an argument against appreciable air contamination in these films even though they may have been prepared under less than ideal leak rate conditions. It is noted that Moustakas reports the peak in photoconductivity at a hydrogen partial pressure of 0.4 mTorr and the minimum at 1.0 mTorr.[36] We observe the peak of 0.8 mTorr hydrogen partial pressure and the minimum of 2.0 mTorr. These differences may be due to the dependence of photoconductivity on system geometry.

Figure 3.20 results from measurements using weakly absorbed, near band gap, light at 0.633 microns wavelength. The generation rate within the film is given by

$$G = \alpha F (1-R) e^{-\alpha x}$$

where α is the absorption coefficient, F is the photon flux incident on the surface, R is the reflectance of the film, and x is the distance into the film. The average generation rate within the film is 1×10^{19} cm^{-3}-sec^{-1} and is uniform to within $\pm$ 20% throughout the sample thickness. With this information, the mobility-lifetime product

may be calculated from the photoconductivity as follows:

$$\sigma_D = q\mu_n n$$

and

$$\sigma_L = q\mu_n (n+\Delta n)$$

for transport dominated by electrons, where q is the electronic charge, μ_n is the electron mobility and n and Δn are the equilibrium carrier concentration and the excess carrier concentration under illumination, respectively. Hole contributions have been neglected here due to extremely short diffusion lengths. Staebler reports hole diffusion lengths on the order of 350 Å.[38] It follows that the photoconductivity is

$$\Delta\sigma_P = q\mu_n \Delta n.$$

Now

$$\Delta n = f\tau$$

where f is the average generation rate within the film and τ is the free carrier lifetime. The mobility-lifetime product is then

$$\mu\tau = \frac{\Delta\sigma_P}{qf}.$$

The photoconductivity of 10^{-9} $(\Omega\text{-cm})^{-1}$, therefore, corresponds to a maximum $\mu\tau$ product for these films of 6×10^{-10} $cm^2/volt$. We have not observed any marked dependence of $\mu\tau$ on incident photon wavelengths.

Photoconductivity has also been determined for the sandwich

samples used for dark conductivity measurements in Section 3.4.1. Figures 3.21 and 3.22 show results of room temperature photoconductivity as well as dark conductivity for samples prepared at a constant input rf power with varying hydrogen partial pressure and for constant hydrogen partial pressure and varying rf input power. The minimum in photoconductivity noted before with the coplanar samples is not observed in Figure 3.21 with the sandwich samples. This may be due to air in the films or the minimum may be present but not observed because of too few data points. It is likely that a certain amount of air contamination is taking place since when the 2.0 mTorr hydrogen partial pressure sample is repeated in a low leak vacuum system where the sputtering atmosphere is approximately 99.98% pure, the photoconductivity shows an increase while the dark conductivity has decreased.

In Figure 3.21 when the hydrogen partial pressure is increased from 0.8 mTorr to 2.0 mTorr the dark conductivity decreases while the photoconductivity increases. This may be understood by recalling that the energy gap has increased, and defect states decreased, which would explain the decrease in dark conductivity due to a reduction of intrinsic carrier concentration and a reduction in hopping. Also an increase in hydrogen content will reduce the number of recombination centers thus increasing the free carrier lifetime and the photoconductivity. Between 2 and 5 mTorr hydrogen partial pressure the dark conductivity is observed to increase. Assuming extended state conduction this behavior would be possible if there was a large increase in mobility overcoming any decrease in carrier concentration. An increase in extended state mobility, on the other hand, should increase

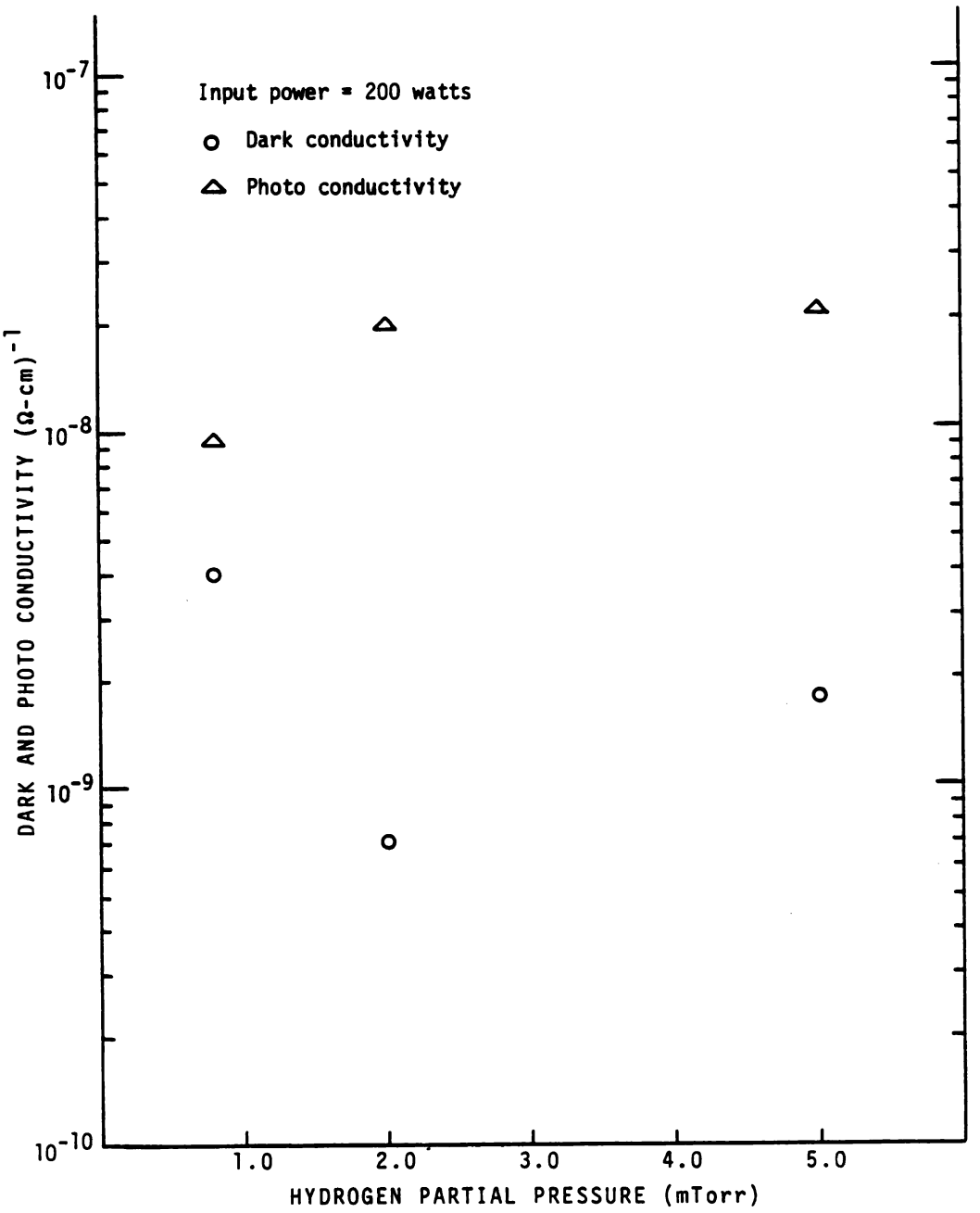

Figure 3.21 Dark and photo conductivity vs. hydrogen partial pressure.

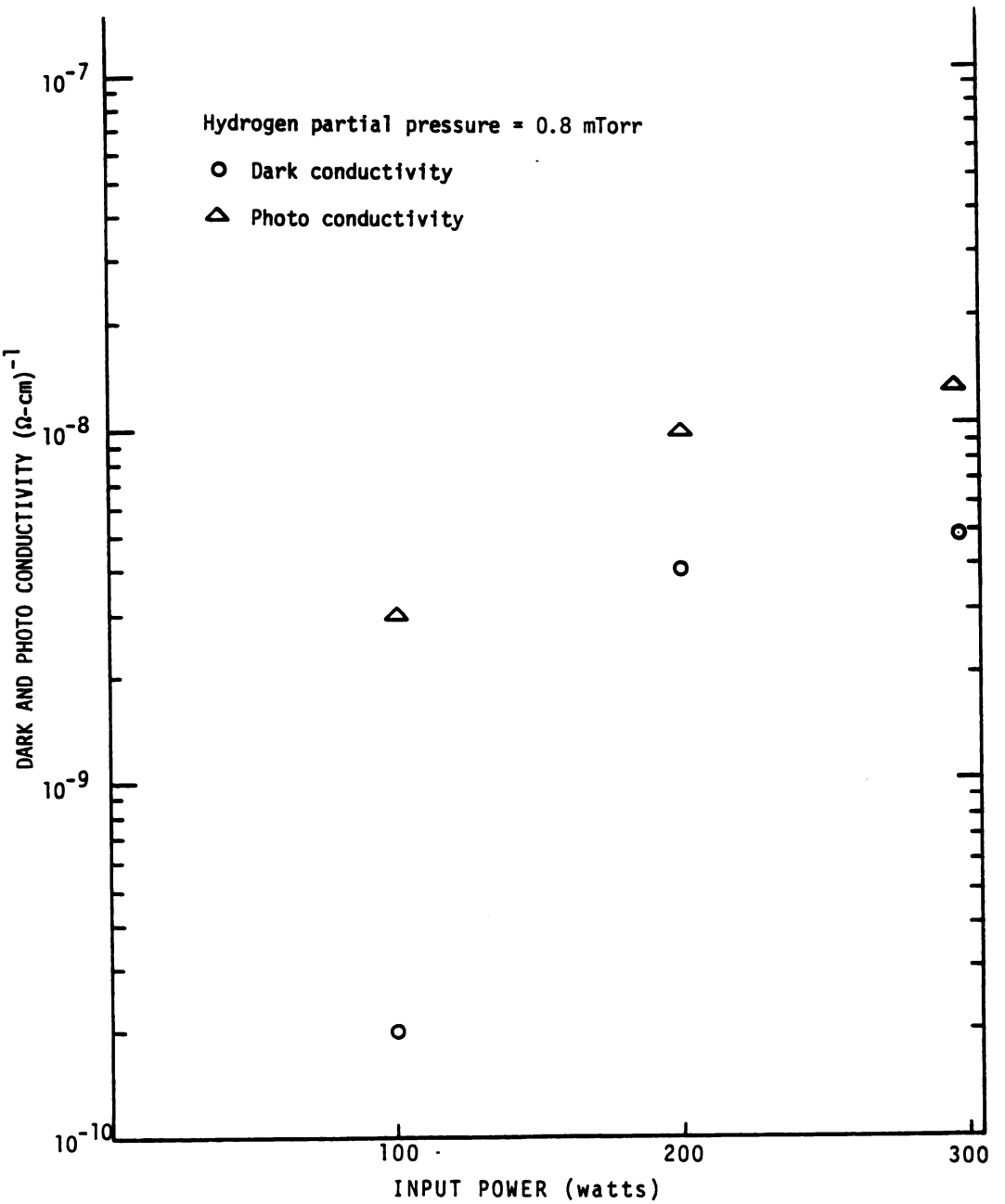

Figure 3.22 Dark and photo conductivity vs. input power.

the photoconductivity, but this is not observed as the photoconductivity is relatively constant. This indicates that the dark conductivity increases due to increasing carrier concentration, that is, a decreasing $E_c - E_f$, if extended state, or number of hopping centers if not. Since no change in $\Delta\sigma_p$ is observed because of increasing defect states, the extended state conduction mechanism is favored.

In Figure 3.22 when the power is increased from 100 watts to 200 watts the dark conductivity increases presumably due, at least in part, to a decreasing $E_c - E_f$ since photoconductivity increases to a lessor extent. The increase in $\Delta\sigma_p$ is likely due to a reduction in recombination centers, either because the density of defect states has been reduced, or because the Fermi level has moved to a region in the gap where the density of states is lower. The energy gap is nearly constant for an input power increase from 200 watts to 300 watts and the equal increase in dark conductivity and photoconductivity may be attributed to an increase in carrier mobility.

The calculation of the mobility-lifetime product for these sandwich samples is not as straight forward as the previous case of coplanar samples. The dark side of the sample farthest from the light source contains a lower concentration of excited carriers than does the lighted side because of the non-uniform illumination effect. The dark side of the sample thus limits the observed photocurrent which complicates the determination of the mobility-lifetime product.

To solve the problem, a sandwich sample is broken up into n slices or partitions with each slice contributing a conductance G_k which are in series making up the total conductance of the sample G_T (Figure 3.23),

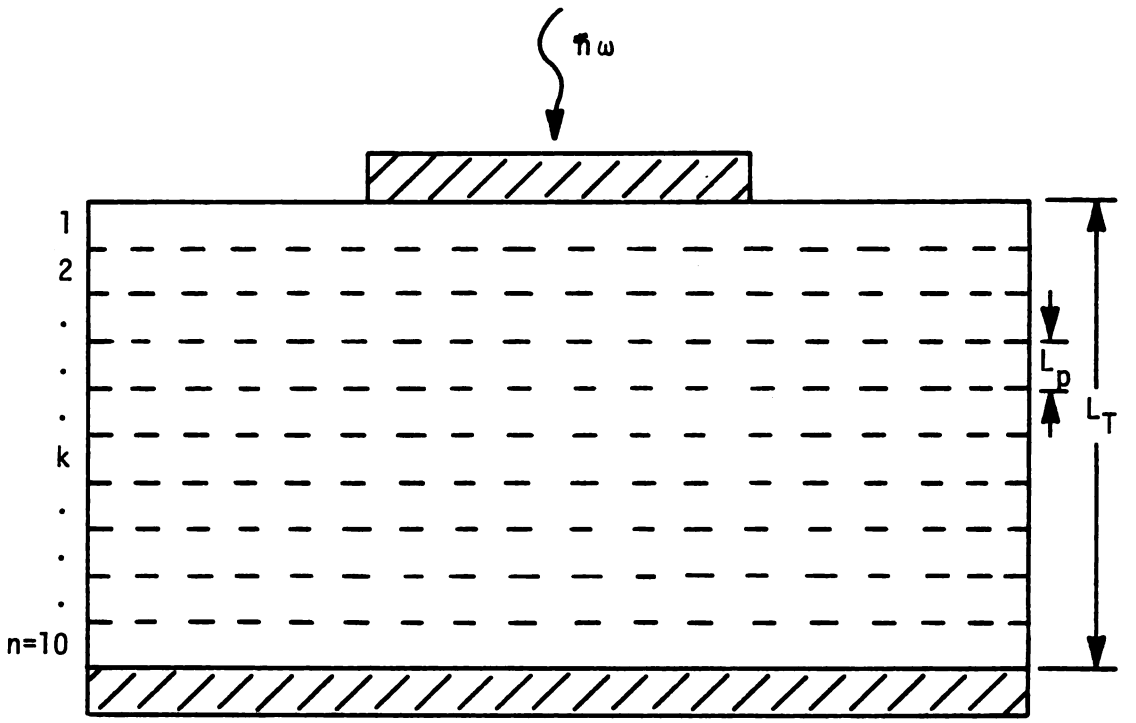

Figure 3.23 Sandwich sample for mobility-lifetime calculation.

$$G_T = \left(\frac{1}{G_1} + \frac{1}{G_2} + \ldots + \frac{1}{G_k} + \ldots + \frac{1}{G_n}\right)^{-1}.$$

The total conductance observed under illumination is then given by

$$G_{TL} = \left(\frac{1}{G_D+\Delta G_1} + \frac{1}{G_D+\Delta G_2} + \ldots + \frac{1}{G_D+\Delta G_k} + \ldots + \frac{1}{G_D+\Delta G_n}\right)^{-1}$$

where G_D is the dark conductance of each slice and ΔG_k is the change in conductance of the kth slice under illumination. To convert conductances into conductivities, the geometry of the samples must be included. This conversion yields

$$\frac{L_p}{L_T}\,\sigma_{TL} = \left(\frac{1}{\sigma_D+\Delta\sigma_1} + \frac{1}{\sigma_D+\Delta\sigma_2} + \ldots + \frac{1}{\sigma_D+\Delta\sigma_k} + \ldots + \frac{1}{\sigma_D+\Delta\sigma_n}\right)^{-1}$$

where L_p is the thickness of each partition, L_T is the total sample thickness and the σ's are conductivities corresponding to the conductances as defined above. The photoconductivity of the kth slice is then determined by the average generation rate in that slice.

$$\Delta\sigma_k = q\mu\tau f_k$$

where

$$f_k = \frac{F_i\left(e^{-(k-1)\alpha L_p} - e^{-k\alpha L_p}\right)}{L_p}.$$

Here, F_i is the photon flux incident on the film surface corrected for

the transmittance of the semitransparent contact and α is the absorption coefficient of the film. The mobility-lifetime product may then be determined by solving the nth order equation

$$\frac{L_P}{L_T}\sigma_{TL} = \left(\frac{1}{\sigma_D+q\mu\tau f_1} + \frac{1}{\sigma_D+q\mu\tau f_2} + \ldots + \frac{1}{\sigma_D+q\mu\tau f_k} + \ldots + \frac{1}{\sigma_D+q\mu\tau f_n}\right)^{-1}.$$

This derivation is valid so long as the drift component of the illuminated current is much greater than the diffusion component. This condition is met in these films. Because of the very low carrier mobilities, there is essentially no diffusion current.

The photoconductivity in Figures 3.22 and 3.23 results from measurements using light at 0.633 microns wavelength with an incident photon flux of 5×10^{15} cm^{-3} sec^{-1}. The molybdenum contacts are approximately 20% transmitting. The $\mu\tau$ products shown in Figures 3.24 and 3.25 were determined by solving for the real positive root of the above equation on a Hewlett-Packard 34C pocket calculator using ten partitions for each sample. The values for the absorption coefficient for each sample are taken from Section 3.3.1.

The maximum $\mu\tau$ product does not necessarily correspond with the maximum photoconductivity. For example the sample prepared at 2.0 mTorr hydrogen partial pressure and 200 watts has a photoconductivity twice as large as the sample prepared at 0.8 mTorr hydrogen partial pressure and 200 watts but about the same $\mu\tau$. Also the 5.0 mTorr hydrogen partial pressure sample has about the same photoconductivity as the 2.0 mTorr sample but the $\mu\tau$ product is almost three times as large. The largest $\mu\tau$ product observed is for a sample prepared at

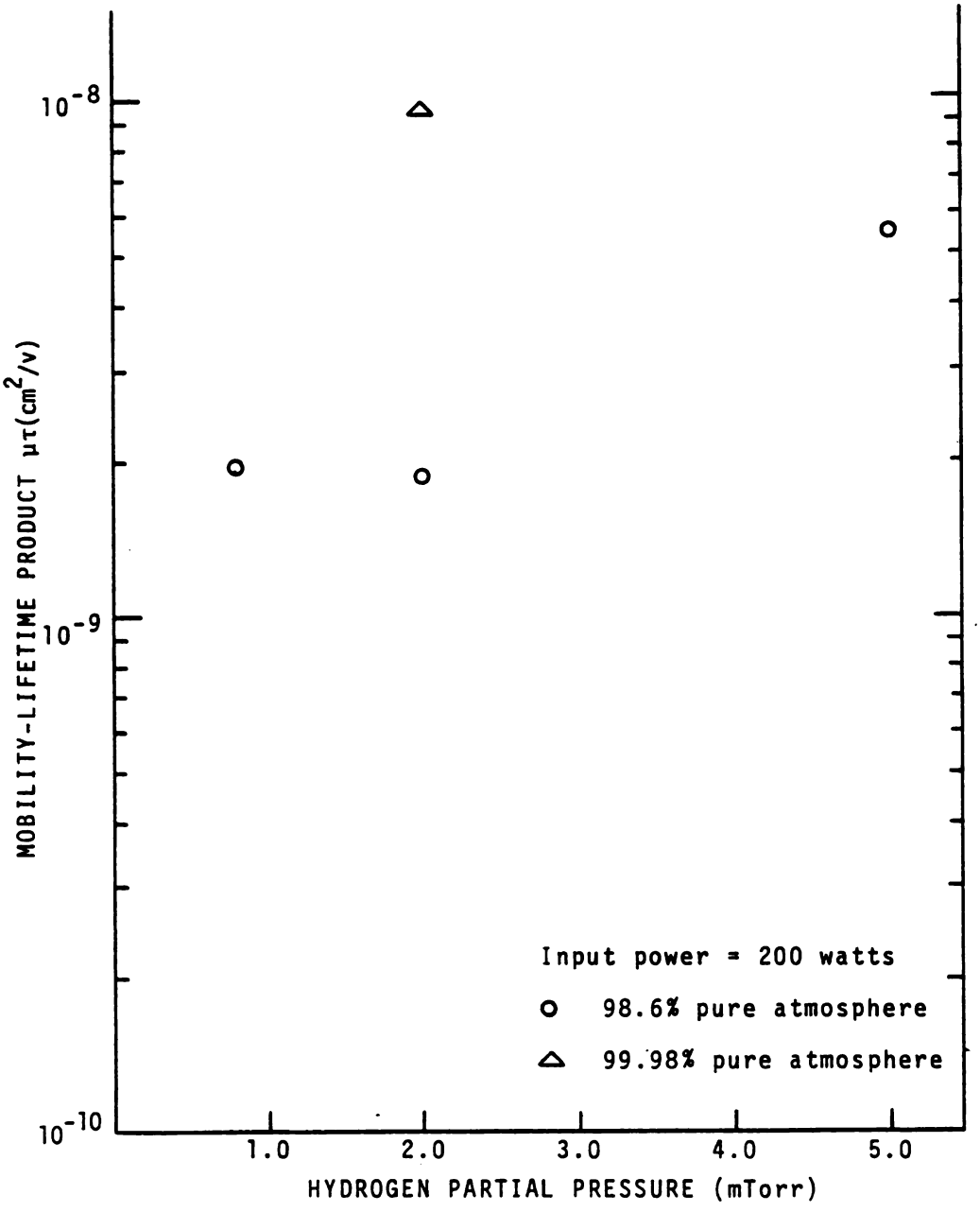

Figure 3.24 Mobility-Lifetime product vs. hydrogen partial pressure.

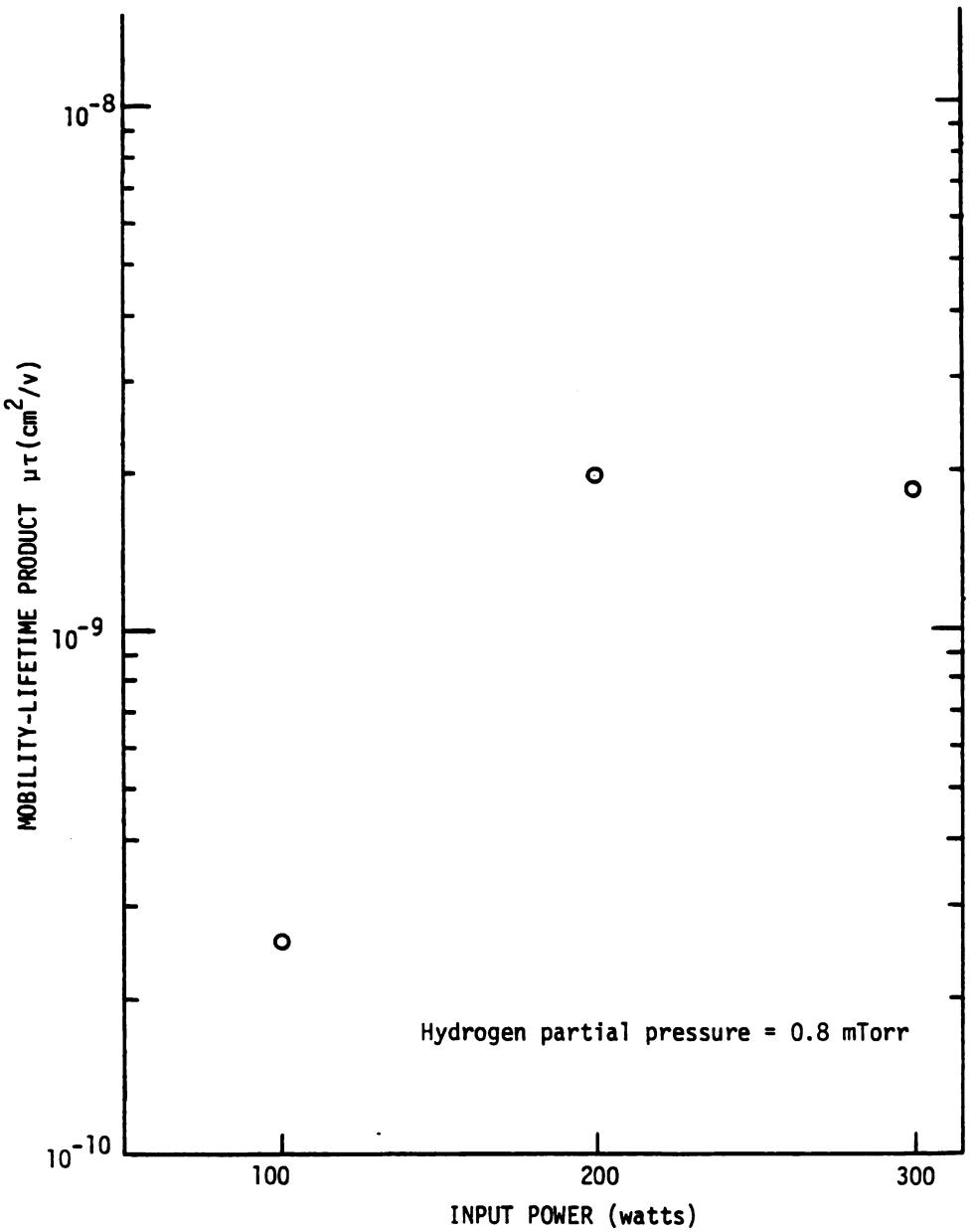

Figure 3.25 Mobility-Lifetime product vs. input power.

2.0 mTorr hydrogen partial pressure and 200 watts in the low leak rate vacuum system where the sputtering atmosphere was approximatley 99.98% pure. This maximum $\mu\tau$ product is equal to 9.6×10^{-9} cm^2/v which is an improvement of five times over the same sample prepared under less pure conditions. Values of $\mu\tau$ reported by others for hydrogenated amorphous silicon have ranged from 10^{-6} cm^2/v to 10^{-10} cm^2/v.[39,40]

3.5 Conclusions

The experimental data presented in this chapter show that intrinsic rf sputtered hydrogenated amorphous silicon material properties depend critically on deposition parameters. The optical properties and electrical properties of silicon films have been studied as functions of the hydrogen partial pressure in the sputtering atmosphere and the rf input power. Even though these are independently varied sputtering parameters, other sputtering parameters vary with them and it is difficult to determine which ones are the fundamental cause of the observed changes in material properties. Also the quality of the vacuum system, in particular the leak rate as compared to the gas flow rate, is an important quantity in determining the film properties. Models are suggested to explain the observed behavior of dark and photo conductivity. From the results of this chapter some intelligent choices may be made concerning the best deposition parameters to achieve optimum semiconductor properties in a particular application.

CHAPTER IV

MODIFICATION OF HYDROGENATED AMORPHOUS SILICON BY CO-SPUTTERING

4.1 Introduction

One of the most important developments in solid state electronics has been the successful doping of crystalline semiconductors. Parts per million of impurities cause several orders of magnitude change in electrical conductivity by modifying hole and electron concentrations. Large parts of the electronics industry depend upon this now "taken for granted" phenomenon. With the recent surge of interest in amorphous semiconductors, much effort has been expended to achieve similar control of the electronic properties of amorphous materials. Early on, several techniques such as co-evaporation, co-sputtering from a composite target, and sputtering from a heavily doped target were tried in an attempt to dope amorphous silicon and amorphous germanium films by the usual donor and acceptor impurities.[41,42,43,44] These experiments yielded disappointing results in that the electrical conductivity was not observed to be highly dependent on impurity content and led to the conclusion that amorphous semiconductors are relatively insensitive to doping impurities. More recently, through a better understanding of amorphous semiconductors and by utilizing different preparation techniques, these limitations have been overcome.

It has become the general consensus that the insensitivity to doping impurities of amorphous silicon and germanium is due to a large number

of structural defects which introduce a large density of localized electronic states in the mobility gap. The density of states in the gap is too high to allow much change in the position of the Fermi level, and thus the electrical properties, unless the impurity concentration is quite high. However, an effective way to reduce the density of states in the gap is to use hydrogen as a termination agent for dangling bonds. Films prepared by the techniques of glow discharge decomposition of silane, SiH_4, and by reactive sputtering in an argon/hydrogen atmosphere contain several atomic percent hydrogen and have a much lower density of states in the gap than evaporated or argon sputtered films. These films have been successfully doped both n and p type by introducing impurities from the gas phase into the deposition atmosphere. Phosphine and arsine have been used as gaseous n type impurities and diborane has been used as a gaseous p type impurity to achieve control of the electrical conductivity over a ten order of magnitude range.[1,14,45,46] More recently ion implantation of group III and V substitutional impurities into glow discharge films has been shown to be an effective way to control the electrical properties over the same range as gas phase doping but with a lower doping efficiency.[23] Because the method of preparation has a distinct effect on the density and distribution of states in the gap and on the doping efficiency, there is presently a great deal of interest in alternate preparation techniques.

In this chapter we will discuss the modification of hydrogenated amorphous silicon by co-sputtering with solid III and V impurities as an alternative method of sample preparation. Aluminum from column III

of the periodic table and arsenic from column V are investigated. The focus of this study, however, is primarily on aluminum, a traditional substitutional p type impurity in crystalline silicon. We will consider the details of the sample preparation as well as the modification of the optical properties and electrical properties of co-sputtered silicon samples. The results are compared to those reported for gaseous doped, ion implanted,and other co-sputtered and co-evaporated films. The co-sputtering approach to impurity incorporation has the advantage of an inherent simplicity in terms of techniques and required apparatus. In addition, co-sputtering may be applied to a large class of materials including those not readily obtainable in a gaseous form.

4.2 Sample Preparation

Films in this study are deposited by rf sputtering in the system described in Section 3.2.1. Prior to film deposition,the sputtering chamber and all gas lines are evacuated by the diffusion pump. A pressure of 2×10^{-6} Torr is measured with the ionization gauge located at the base plate of the evaporation bell jar; the actual base pressure in the chamber and gas lines is higher, however, due to the conductance of the interconnecting vacuum lines. For all samples in this co-sputtering study,a total sputtering gas pressure of 23 mTorr is then established by throttling the diffusion pump, adjusting the needle valve, and pressurizing the gas lines. The sputtering gas is a 9:1 argon/hydrogen mixture and is pre-mixed as described in Section 3.2.2. The basic sputtering target is a two inch diameter poly-crystalline silicon disk which makes up the cathode of the rf sputtering

system. The cathode requires water cooling to prevent overheating and deterioration of the target. The substrate holder is usually grounded (except when bias sputtering) and is spaced 5.9 cm above the target. A sputtering power of 100 watts or about 5 watts/cm^2 is applied to the matching network which yields a deposition rate at the substrate of 1.3 Å/sec or about 0.5 microns/hour. The system can usually be matched to the generator via the matching network so that less than 5 watts are reflected. Substrates are prepared as described in Section 3.2.2. The substrate is heated to a temperature of 175° C as determined by a thermocouple in contact with the glass but shielded from direct exposure to the plasma. The target is sputter cleaned for 5 minutes using a shutter to shield the substrate and the substrate is back biased sputtered at -15 volts dc for 5 minutes prior to deposition. The film thickness after 4 hours is typically 2 microns as determined by Tolansky multiple-beam interferometry. Two types of samples, optical and electrical, are deposited simultaneously side by side in the system. Optical samples consist of an amorphous silicon film deposited directly on a microscope cover slip. Electrical samples require metal contacts and are made in two configurations, coplanar and sandwich. Coplanar electrodes are deposited on top of the amorphous silicon film, are separated by 0.4 mm, and are 1 cm in length. Sandwich electrodes consist of either a continuous bottom contact sheet with both 0.8 mm and 1.6 mm diameter circular top contacts or 4 bottom strip contacts cross-hatched with 4 top strip contacts in a matrix configuration of 16, 1/32" x 1/32" sandwich devices. Molybdenum contacts are used throughout and are also deposited by rf sputtering.

Doping impurities are incorporated by co-sputtering from an impurity/silicon composite target constructed by positioning flat pieces of the solid impurity on the surface of the silicon target in a ring near the periphery (Figure 4.1). This geometry allows flexibility in choosing the impurity/silicon target area ratio since sputtering yield within a cylindrically symmetrical sputtering chamber is constant for a given radial distance from the target center and a large radius is used. Figure 4.2 illustrates sputtering yield from a 2" target and was obtained by measuring target wear. The aluminum is obtained as five nines pure aluminum wire and is flattened to present a surface planar with the silicon target. The arsenic is prepared by subliming high purity grade arsenic metal powder onto a glass microscope slide in a nitrogen atmosphere. The glass is then removed leaving a flat shiny arsenic surface.

For the case of co-sputtering aluminum, sample films have been made by systematically varying the aluminum/silicon target area ratio from 0% to 10.6%. Of course it is desirable to know how the actual aluminum content in the film correlates with the percentage of aluminum in the target. Electron microprobe analysis was performed on optical samples with aluminum making up 2.8%, 7.1% and 10.6% of the composite target area. Samples with less aluminum content have resistivities that are restrictively high. A thin layer of graphite is evaporated onto microprobe samples to increase the surface conductance. A 7 kV electron beam is used for the microprobe as either a point source, 1 μ x 1 μ, or as a swept area 40 μ x 50 μ. Several areas across the samples are analyzed to test homogeneity. At this electron beam

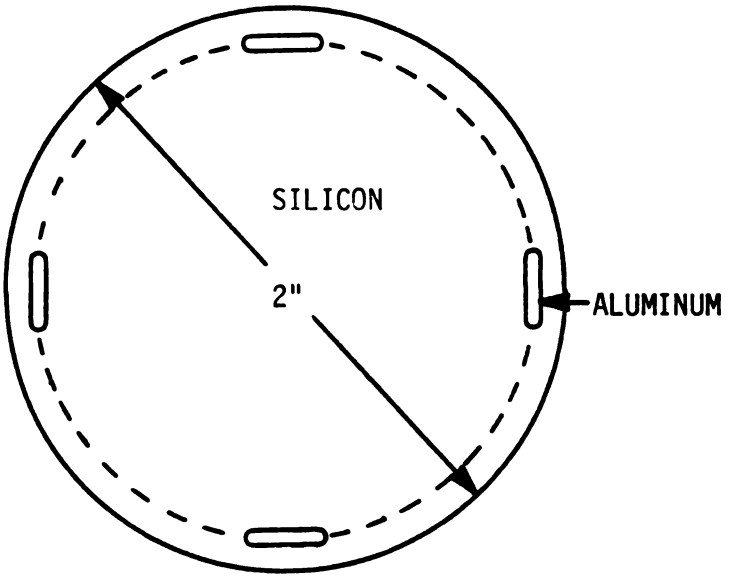

Figure 4.1 Silicon/aluminum composite sputtering target.

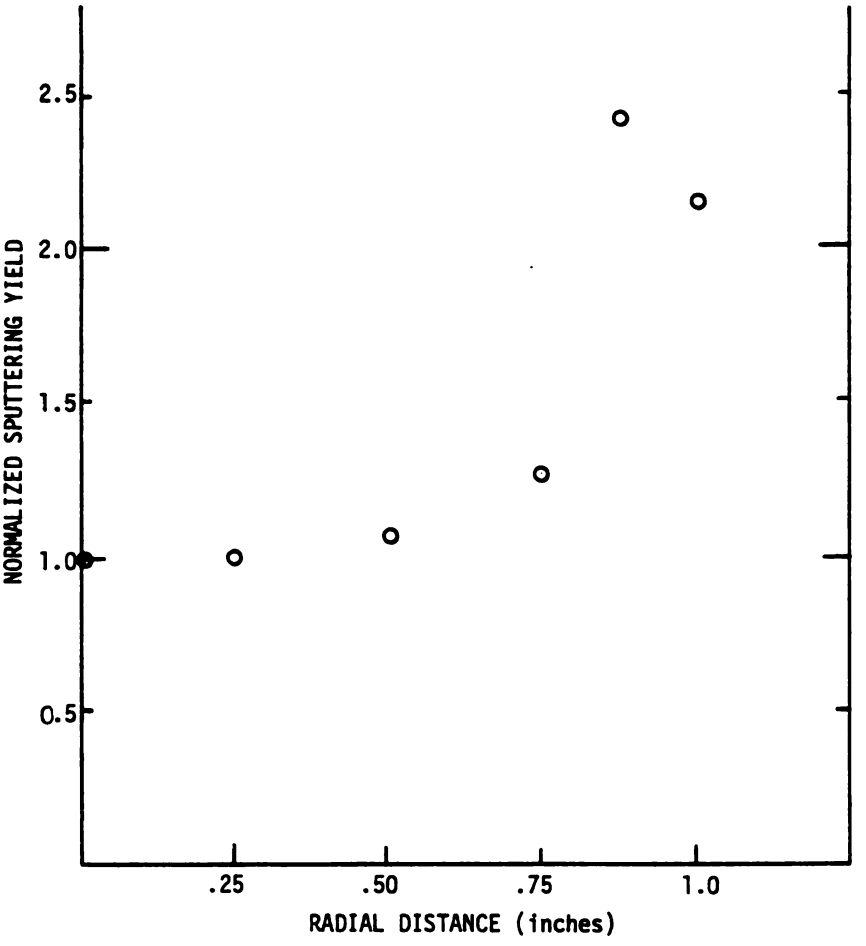

Figure 4.2 Sputtering yield from target as a function of radial distance (normalized to unity at center).

energy,magnesium, sodium and calcium are not detected,indicating the beam does not penetrate through the film into the glass substrate. The results of the analysis show that the percentage of aluminum in the sample films is approximately 2.2 times more than that present in the target and is homogeneous across the sample. This information will be used in Section 4.5 when results are compared to other work.

4.3 Optical Properties

Optical transmission and reflection data were taken for samples deposited on glass substrates from composite aluminum/silicon targets with aluminum accounting for 0% to 10.6% of the target area. Photon generation from 0.8 eV to 2.5 eV is achieved with a Bausch and Lomb grating monochrometer and the appropriate low pass filters. The dual beam system uses chopped light, germanium photodiodes, and a phase-locked amplifier for detection as described in Section 3.3. The formulas used and the approximations made to determine the optical properties are also covered in detail in Section 3.3 but will be briefly reviewed here for completeness.

Of particular interest is the optical absorption coefficient α. Two approximations have been made to determine α. First we assume that reflection is constant with wavelength. This is justified provided α is not small since the interference averaged reflectance varies only from 25% to 30% over the wavelengths of interest. Secondly, since reflection from the air/silicon, silicon/glass, and glass/air interfaces has not been determined separately, we approximate the transmittance as $T \simeq (1-R)e^{-\alpha d}$, where d is the film thickness and

(1-R) is the value at which the interference averaged transmittance levels off at higher wavelengths. The resulting uncertainty in α is $\leq$ 10% for $\alpha > 10^3$ cm^{-1}. Figure 4.3 shows the calculated α for a sample deposited from a 0.4% aluminum/silicon composite target as well as α for crystalline silicon and crystalline gallium arsenide as reported by Dash and Newman and by Hill.[47,48] The steepness of α vs. $\hbar\omega$ for amorphous hydrogenated silicon-aluminum is closer to a direct band gap material such as GaAs. This can be advantageous in thin film solar cell applications since a large portion of the solar spectrum can be absorbed in a one micron thick film.

The relationship $\alpha\hbar\omega = F(\hbar\omega - E_{og})^2$ (developed in Section 3.3), where F is a constant and E_{og} is defined as the optical gap, is approximately correct over limited regions for these samples. Figure 4.4 shows $(\alpha\hbar\omega)^{\frac{1}{2}}$ vs. $\hbar\omega$ for samples deposited from composite targets with 0.4% to 10.6% aluminum. For small concentrations of aluminum the intercept indicates an optical gap of 1.83 eV. With increasing aluminum concentration up to 2.7% the optical gap remains constant but an increased tail and increased slope are observed. This suggests that the basic band structure is unchanged but the aluminum atoms add states, presumably near the valence band edge, in the gap. However, further increase in aluminum concentration introduces a different behaviour and the intercept E_{og} is now shifted to lower energies. This rather abrupt change in behavior seems to be around 3% to 4% aluminum in the target. By 10.6% aluminum, the optical gap has dropped by half to 0.87 eV. With aluminum concentration above 3% to 4% in the target, the material takes on characteristics of a new semiconductor as far as the optical properties are concerned, namely a hydrogenated

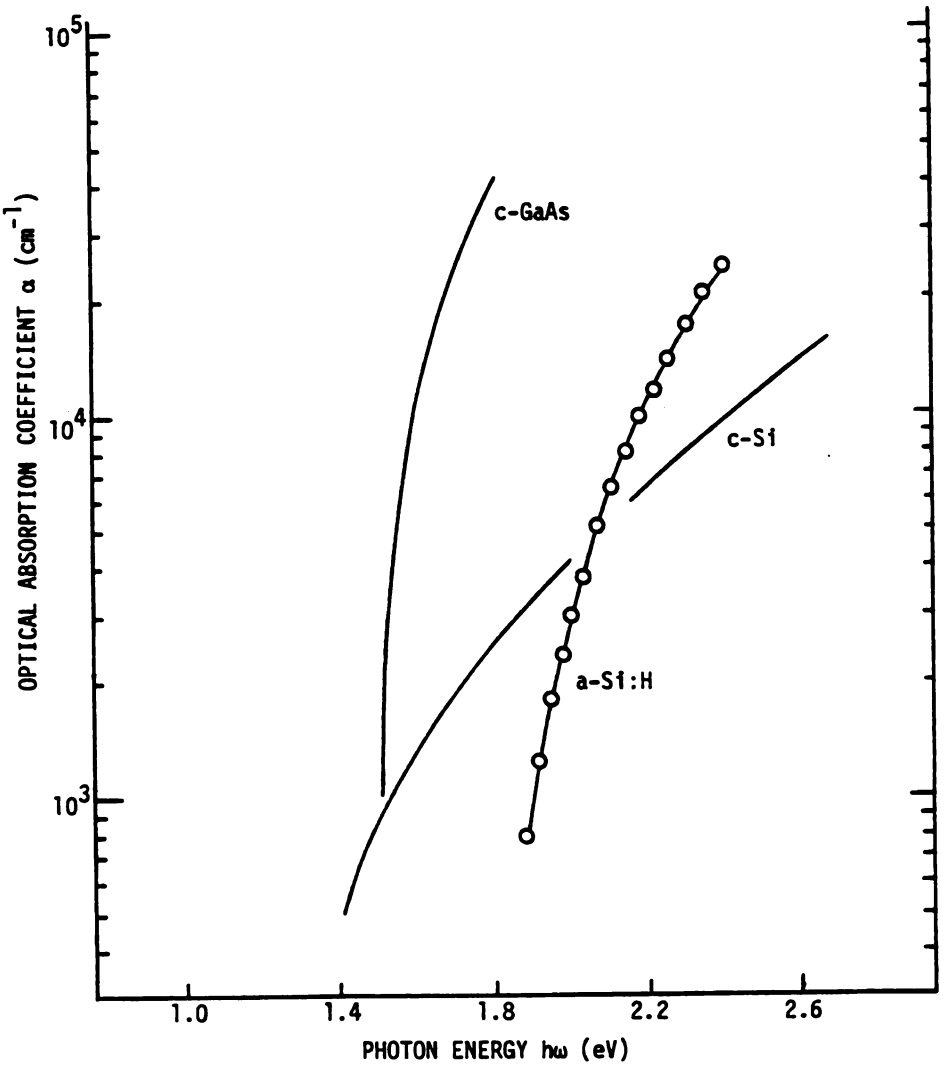

Figure 4.3 Optical absorption coefficient for a-Si:H, c-Si, and c-GaAs.

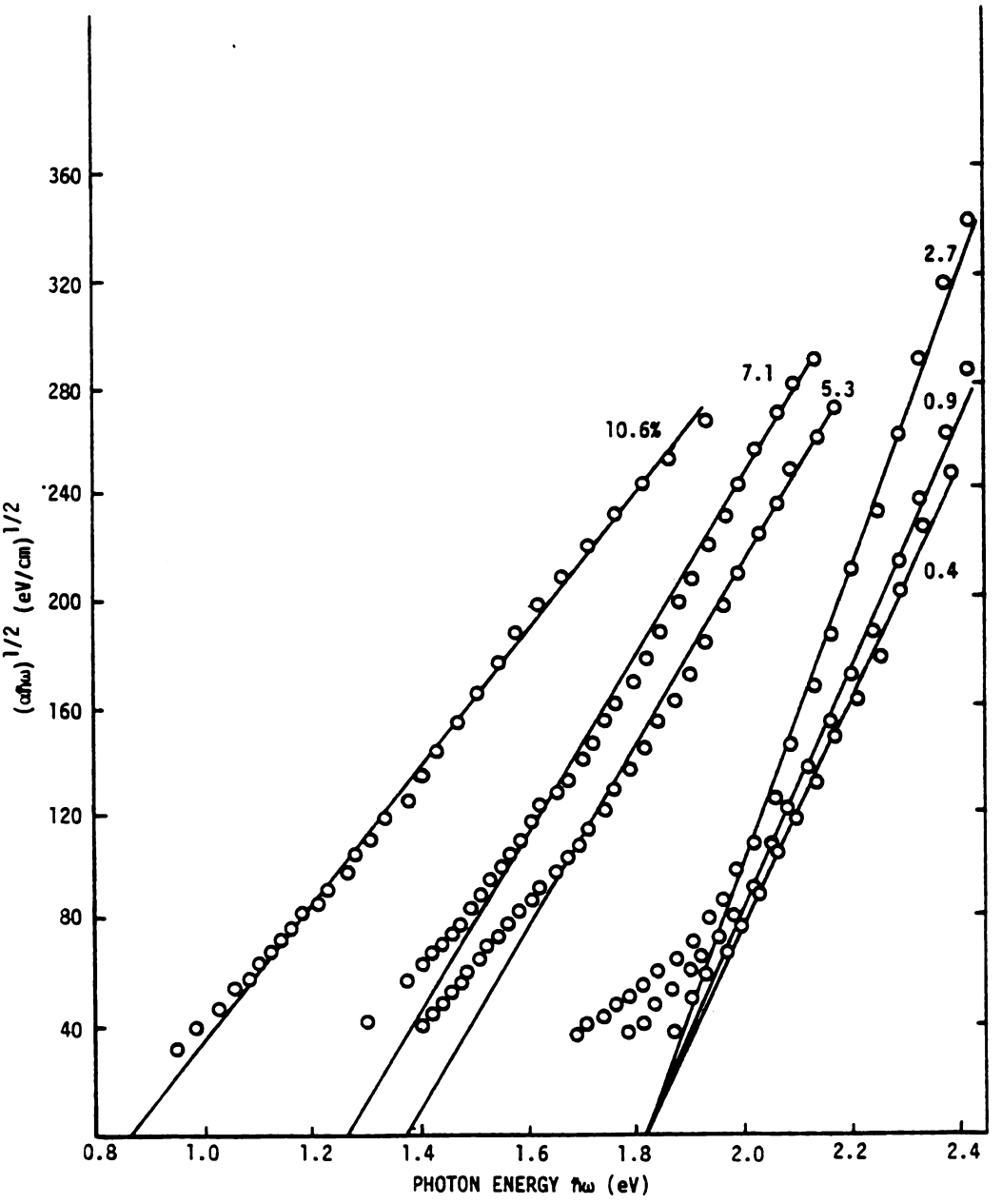

Figure 4.4 $(\alpha\hbar\omega)^{1/2}$ vs. photon energy for different Al/Si target ratios.

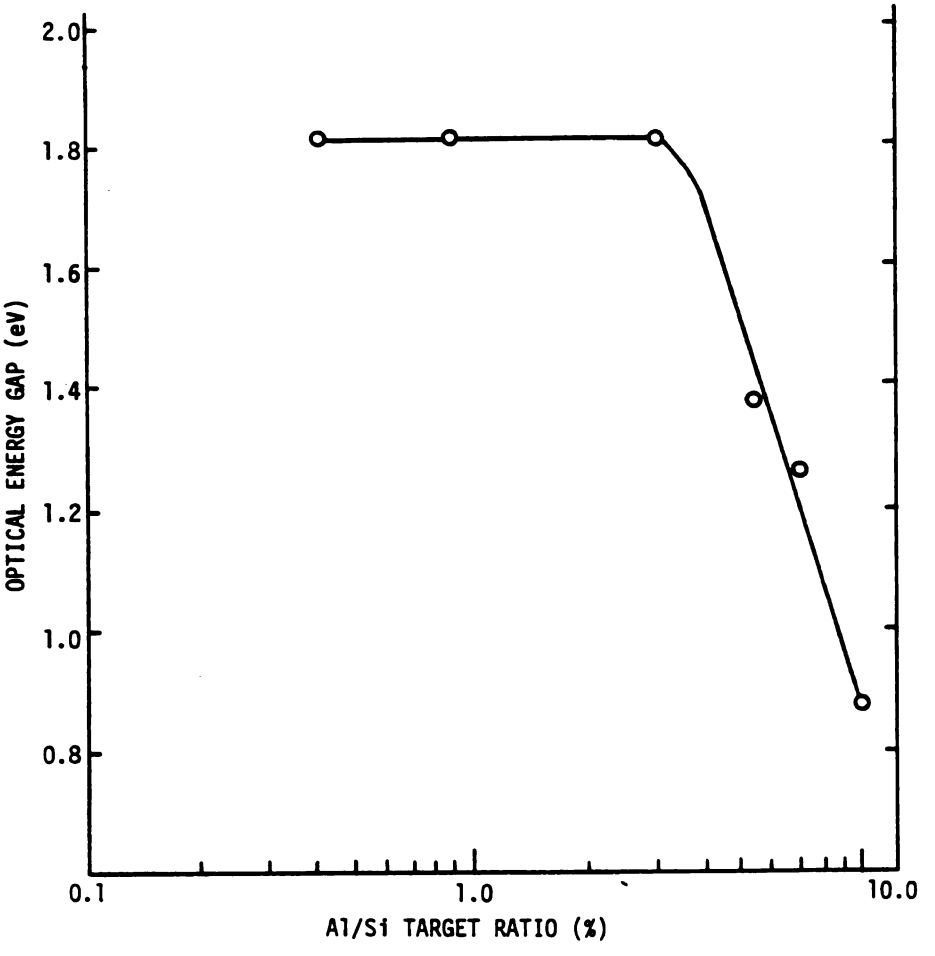

Figure 4.5 Optical energy gap vs. Al/Si target ratio.

amorphous silicon-aluminum alloy. Choosing the aluminum concentration allows one to tailor the optical gap (Figure 4.5). Below 3% the effect is merely to add states to the tail of the density of states. Above 5% a rather different band structure entirely is observed. Perhaps non-localized states become localized around this transition point.

4.4. Electrical Properties

The electrical properties of samples prepared from composite targets containing 0% to 10.6% aluminum are reported in this section. Current vs. voltage is measured for all samples in the sandwich geometry prepared with molybdenum top and bottom contacts. For some samples with high aluminum content, coplanar samples are also prepared with top molybdenum contacts. For very small aluminum concentrations, that is for samples with relatively high resistivies, the measurements with the matrix type sandwich contacts are compromised by surface leakage. By changing to the circular sandwich sample geometry this leakage problem is reduced. I-V measurements are taken at room temperature in the dark with a continuous flow of dry nitrogen through a desiccated container. The magnitude of the electric field applied is between 2.5 kV/cm and 5.25 kV/cm. For the sandwich geometry, measurements include contact effects. We believe bulk effects dominate the I-V measurements for the following reasons. 1) The I-V curves are fairly linear, although slightly superlinear. Actually the measured conductivity at 1.0 volts bias averages 24% higher than the conductivity at 0.5 volts bias. Band bending does indeed occur at the contacts since we observe zero bias photocurrents, however, the bulk resistance is

sufficiently high to dominate the impedance to current flow. 2) Measurements with the four coplanar strip geometry, where contact effects are minimized, verify the sandwich geometry results. 3) Molybdenum has previously been reported as a suitable contact material for p type hydrogenated amorphous silicon.[14]

Figures 4.6 and 4.7 summarize the results of the room temperature conductivity for varying percentages of aluminum in the composite target from 0% to 10.6%. Initially the conductivity decreases with aluminum concentration suggesting that compensation of the inherently n type starting material is taking place. Thereafter the conductivity increases monotonically with aluminum concentration and ranges over 7 orders of magnitude. This change in conductivity can be attributed to two factors. One is a shrinking band gap as is indicated by the optical data. The second is the movement of the Fermi level closer to the valence band edge.

It is also instructive to consider the temperature dependance of the conductivity. For normal extended state conduction, the conductivity is expressed as $\sigma = \sigma_o e^{-Ea/kT}$, where the pre-exponential term σ_o is approximately constant and E_a is defined as the thermal activation energy. Conductivity versus temperature is measured from room temperature to 100^o C. Semilog plots of σ vs. $10^3/T$ yield approximately straight lines over much of the region investigated and the slopes of these lines determine the activation energy E_a (Figure 4.8). Initially, for small concentrations of aluminum in the target, there is an increase in E_a as compensation takes place. For larger aluminum content E_a decreases to a minimum value slightly less than 0.2 eV in agreement

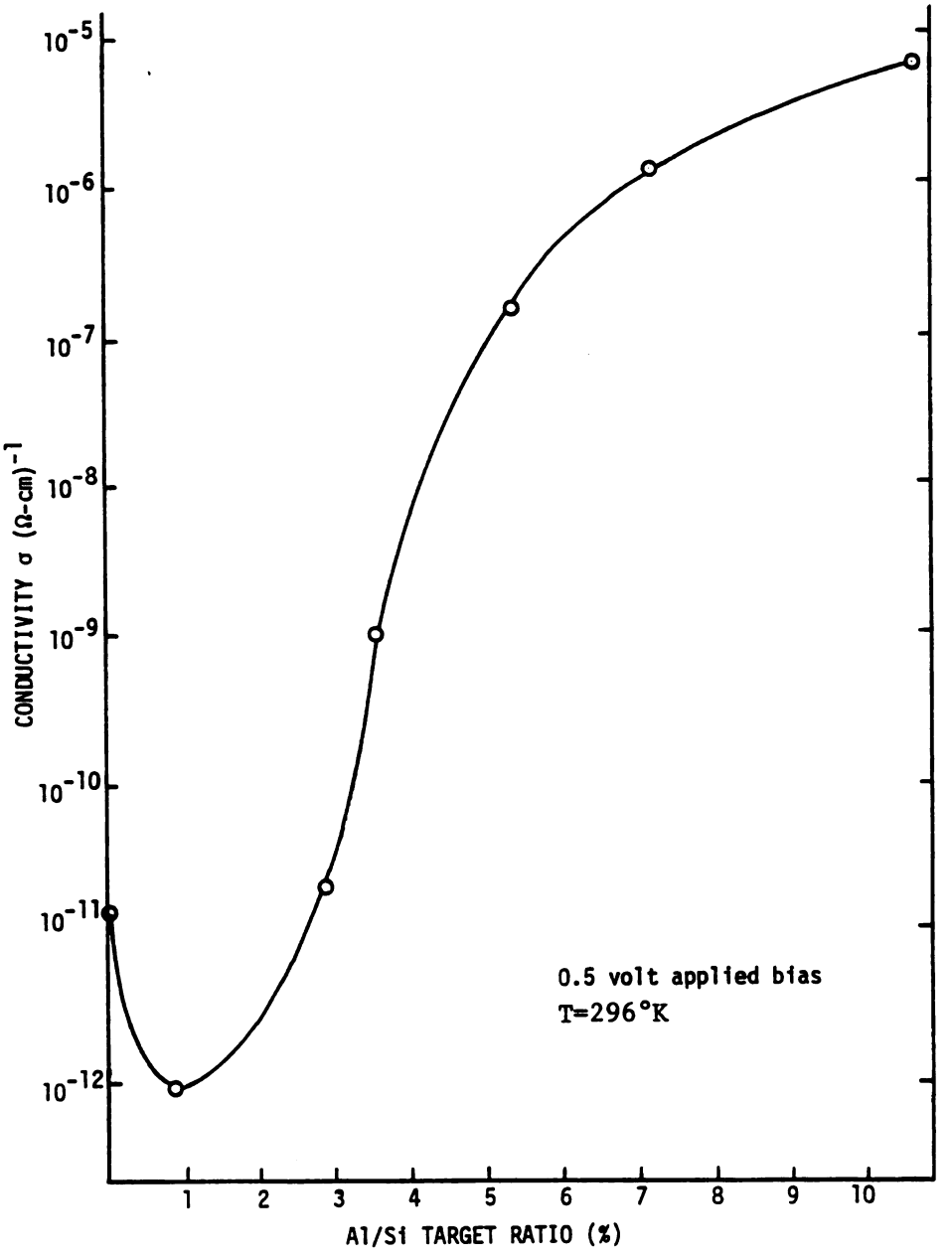

Figure 4.6 Room temperature conductivity vs. Al/Si target ratio at 0.5 volt applied bias.

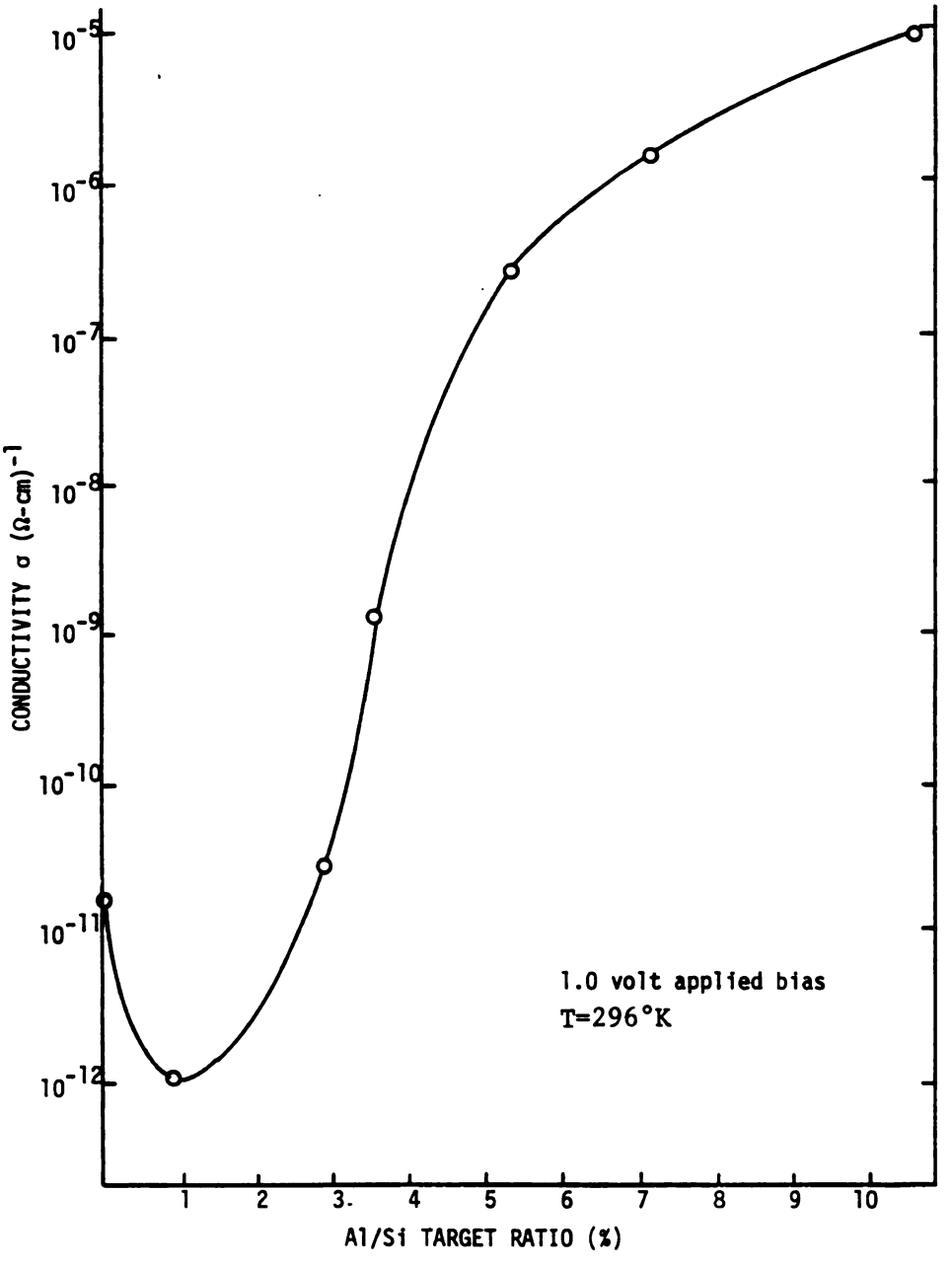

Figure 4.7 Room temperature conductivity vs. Al/Si target ratio at 1.0 volt applied bias.

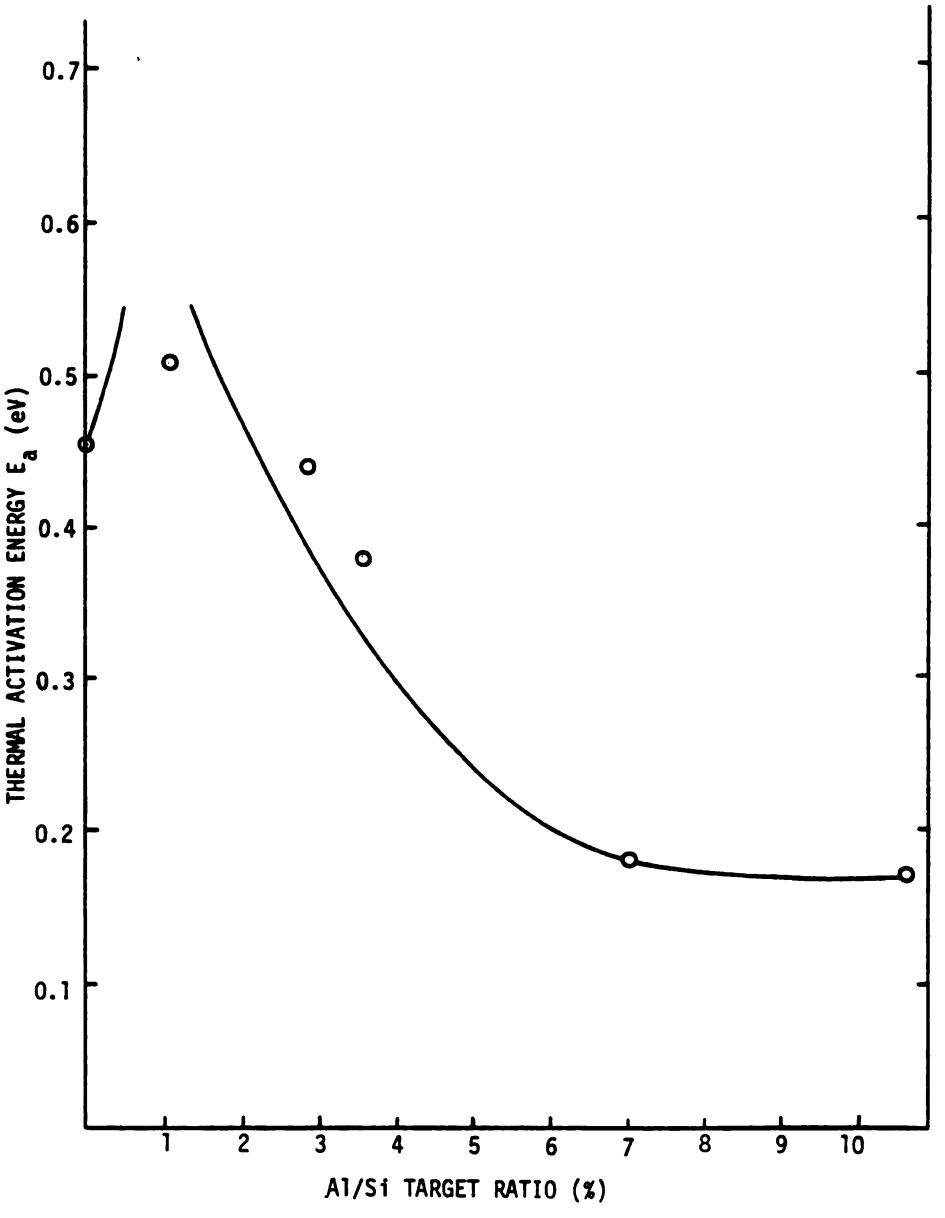

Figure 4.8 Thermal activation energy vs. Al/Si target ratio.

with previously reported work on gas phase doping and ion implantation. Using the extended state model these data, in conjunction with the optical data, suggest that the Fermi level is moved from 0.45 eV below the conduction band to 0.20 eV above the valence band edge as the aluminum concentration is increased. Note that E_a apparently levels off at 7% aluminum on the target. Additional increases in conductivity are then due to a shrinking band gap rather than further movement of the Fermi level.

Such an analysis neglects hopping contributions to conductivity. The pre-exponential term, σ_o, is in the range of 10^{-2} to 10^{-3} $(\Omega\text{-cm})^{-1}$. Values of σ_o less than one are usually associated with hopping, while extended state conduction corresponds to values of σ_o on the order of 10^2 - 10^3 $(\Omega\text{-cm})^{-1}$. This would indicate that in the temperature range studied, hopping is a dominant conduction mechanism and part of the role of aluminum modification is to vary the hopping activation energy. The Harvard group, in undoped films, report hopping below 80^o C.[18] If our co-sputtered films have more states in the gap, one would expect hopping to persist to higher temperatures. In most of the co-sputtered samples, the system leak rate was not closely monitored and could have been as high as 2.3×10^{-4} scc/sec. The gas purity at 20 mTorr sputtering pressure would then be only 99.7% which could account for a higher density of states in the gap.

Co-sputtered arsenic was also investigated, but to a lessor extent. Arsenic is a traditional n type substitutional impurity in crystalline silicon and has been used effectively as a gaseous impurity in glow discharge amorphous silicon. A sample deposited from a composite

target with an arsenic/silicon target area ratio equal to 2.5% and prepared in the 16 device matrix configuration shows essentially no change in room temperature conductivity when measurements are taken in the sandwich structure. However, in the coplanar structure there is a large difference between top and bottom coplanar measurements. The conductivity measured with bottom coplanar contacts is four orders of magnitude higher than that measured on the top. Another interesting observation is that the arsenic on the target is a dull dark grey or black after the sputtering run,in contrast to the shiny metallic appearance before sputtering. This phenomenon may be associated with oxidation,however,the results were repeated in a very low leak situation where the leak rate into the vacuum system is small enough so that the sputtering atmosphere is 99.98% pure. These observations are interpreted to indicate that initially arsenic does dope the material but that its effectiveness as a dopant degrades to zero after several minutes of sputtering. The first several hundred angstroms of film are doped but the remaining is not, therefore, the sandwich measurements do not indicate appreciable change in conductivity but the coplanar measurement do.

4.5 Comparison with other Techniques

In this section we will consider the results of our investigation of incorporating impurities into hydrogenated amorphous silicon by the technique of co-sputtering in comparison to results reported using different techniques. Because of the wide number of impurities investigated by several groups using sometimes vastly different deposition parameters, comparison between methods must be made carefully. Figure

4.9 summarizes the ranges of achievable room temperature conductivity reported for different impurities and preparation techniques. In some cases reports were for coplanar electrodes, in others sandwich electrodes. Not all of these results are directly comparable. For instance some impurities are traditional substitutional n type impurities in crystalline silicon, others are traditional substitutional p type impurities in crystalline silicon, and yet others are neither such as the alkalies, halogens and the transition metal nickel. Also some of the films do not contain hydrogen. We will restrict our detailed comparisons of aluminum co-sputtered films to other hydrogenated films containing traditional p type impurities.

We have observed a change in conductivity over seven orders of magnitude which is less than the best results reported for gaseous doping. We have not achieved the high end of the reported conductivities, however, the lowest conductivity observed for co-sputtered aluminum compensated material is comparable to values reported for boron compensated films. A direct comparison to other work requires information about the number of acceptor impurities actually incorporated into the film. As previously discussed, electron microprobe analysis on our samples indicate an aluminum concentration in the films approximately 2.2 times higher than the ratio in the composite target. This is consistent with measurements of the sputtering yield on the target as a function of distance from the center.

The problem of doping amorphous silicon is not as straightforward as that in the crystalline case. Because of the flexibility of arrangement of atoms in the random network, it is not obvious that a p type

Figure 4.9 Survey of ranges of available conductivity for different doping impurities and preparation techniques.

(1) Glow discharge hydrogenated amorphous silicon (a-Si:H) with 0-1000 ppm PH_3 in deposition atmosphere.[45]

(2) RF sputtered a-Si:H with 0-2000 ppm PH_3 in deposition atmosphere.[49]

(3) Glow discharge a-Si:H ion implanted with 0-10^{22} cm^{-3} P.[23]

(4) Glow discharge a-Si:H ion implanted with 0-10^{21} cm^{-3} As, Sb, and Bi.[50]

(5) DC co-sputtered a-Si:H with 0-10^{-2} ppv Sb.[22]

(6) DC sputtered a-Si:H with doped target containing 0-2 X 10^{16} cm^{-3} P.[51]

(7) Glow discharge a-Si:H with 0-10^{5} ppm B_2H_6 in deposition atmosphere.[45]

(8) RF sputtered a-Si:H with 0-2000 ppm B_2H_6 in deposition atmosphere.[49]

(9) Glow discharge a-Si:H ion implanted with 0-10^{22} cm^{-3} B.[23]

(10) Glow discharge a-Si:H ion implanted with 0-10^{21} cm^{-3} Al, In, and Ga.[50]

(11) RF co-sputtered a-Si:H with 0-10.6% Al/Si target ratio. *(this study)

(12) DC sputtered a-Si:H with doped target containing 0-10^{19} cm^{-3} B.[51]

(13) Glow discharge a-Si:H ion implanted with 0-10^{21} cm^{-3} alkali ions (Na, K, Rb, Cs).[52]

(14) Glow discharge a-Si:H ion implanted with 0-10^{21} cm^{-3} halogen ions (F, Cl, Br, I).[50]

(15) DC co-sputtered a-Si (non-hydrogenated) with 0-8.5 at.% Ni.[53]

(16) Co-evaporated a-Si (non-hydrogenated) with 0-1.2 at.% In.[21]

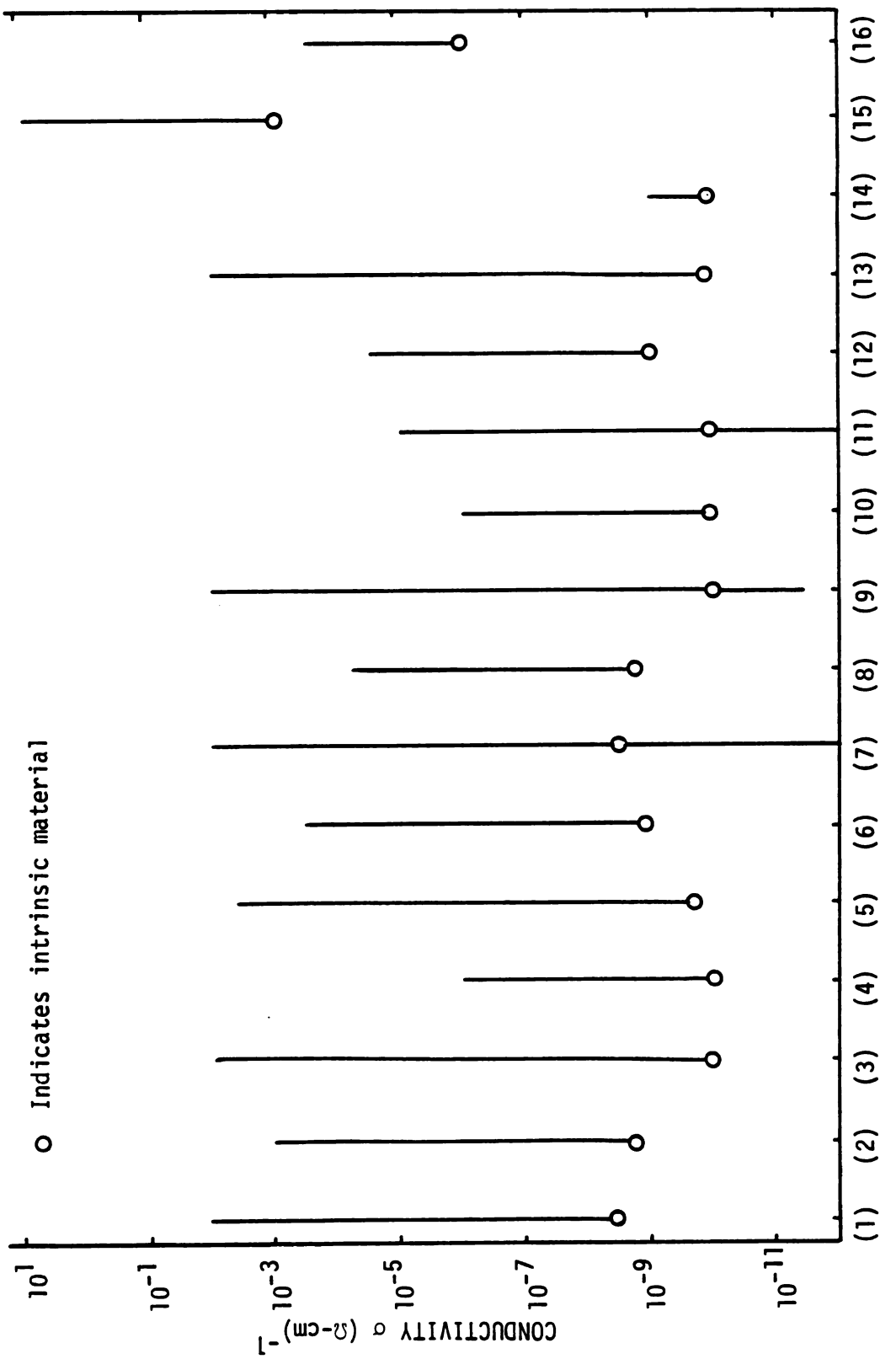
CONDUCTIVITY σ (Ω-cm)⁻¹
10¹
10⁻¹
10⁻³
10⁻⁵
10⁻⁷
10⁻⁹
10⁻¹¹
(1) (2) (3) (4) (5) (6) (7) (8) (9) (10) (11) (12) (13) (14) (15) (16)
O Indicates intrinsic material

Figure 4.9

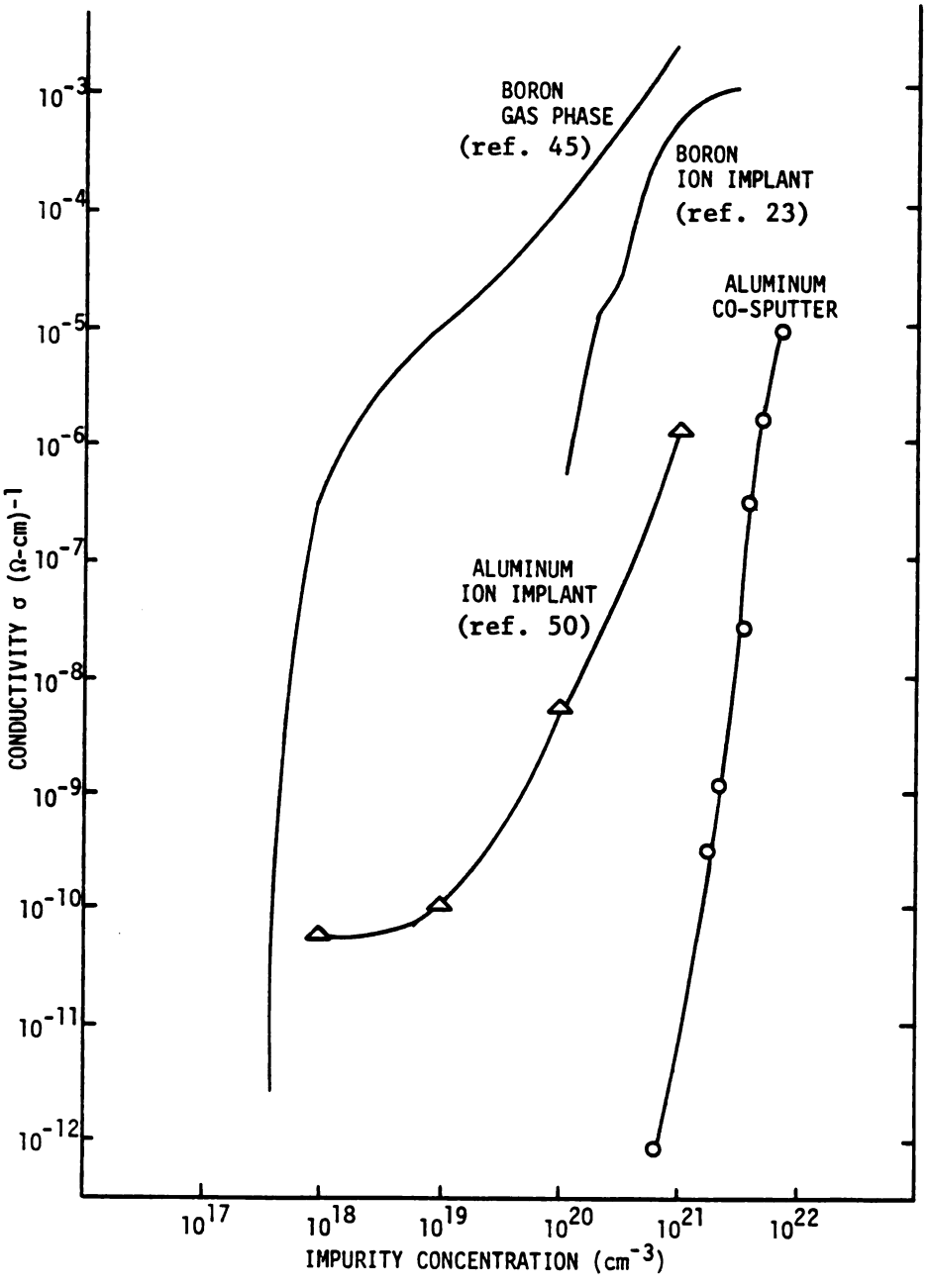

Figure 4.10 Conductivity vs. acceptor impurity concentration for different doping techniques.

(or n type) impurity will bond into the amorphous structure in such a way as to retain its acceptor-like (or donor-like) characteristics. This is a very important practical and as yet, poorly understood problem.

Figure 4.10 shows that gas phase doping of glow discharge produced material with boron is probably the most efficient way to date of accomplishing p type doping. It is estimated that approximately one of ten incorporated boron atoms acts as an acceptor in gas phase doping. Because this is considerably less than 100%, there is much interest in alternate techniques. The technique of ion implantation of boron into glow discharge material is apparently less efficient than boron gas phase doping. The data indicate that for ion implantation perhaps one in a hundred implanted boron atoms acts as an acceptor. The efficiency of ion implantation doping is also dependant on the impurity being implanted as can be seen for the case of aluminum implants where only about one in a thousand aluminum atoms are effective acceptors. Using the results of the electron microprobe analysis, co-sputtering aluminum is even less efficient than ion implantation of aluminum. About one aluminum atom in three thousand acts as an acceptor in co-sputtered hydrogenated amorphous silicon films. Fundamentally, co-sputtering may tend to be less efficient than gas phase or ion implantation because not all sputter ejected particles from the target are atomic. Aluminum molecules up to Al_7 have been reported in argon sputtered aluminum.[54] Still co-sputtering is an interesting approach to impurity incorporation because of the inherent simplicity in terms of techniques and required apparatus and because it may be applied to a large class of materials

including those not readily obtainable in a gaseous form. It does lend itself to an effective tailoring of the optical gap.

CHAPTER V

SCHOTTKY BARRIER DEVICES

5.1 Introduction

Schottky barrier devices have previously been fabricated with hydrogenated amorphous silicon by several groups.[4,14,55,56,57,58,59,60] Both glow discharge decomposition of silane and reactive rf sputtering have been successfully used for silicon deposition. In fact, the highest conversion efficiency reported in the literature to date for a hydrogenated amorphous silicon solar cell (5.5%) was a platinum MIS Schottky barrier device fabricated with silane decomposed material.[4] The insulating layer in this structure was native SiO_2. However, presently missing from the literature are certain details of the device fabrication techniques which result in the formation of rectifying Schottky barrier devices.

In this chapter, the properties of Schottky barrier devices fabricated with rf sputtered hydrogenated amorphous silicon are reported for two reasons. First, the details of the sample preparation are presented as a guide to future researchers. Among the important factors here are the deposition methods of the Schottky barrier metal contact and the purity requirements of the deposition atmosphere for producing device quality hydrogenated amorphous silicon in a rf sputtering system. Secondly, the dark Schottky barrier characteristics

and the photovoltaic properties of devices are compared to other "state of the art" devices reported in the literature. This provides useful information for assessing the quality of the device material produced and identifing outstanding problem areas.

5.2 Sample Preparation

The basic techniques of Schottky barrier sample preparation are similar to those outlined in Chapter III,with modifications to achieve an ohmic contact to one side of the device and a Schottky barrier contact to the other side. It is noted also that the quality of the vacuum system in terms of the leak rate versus the gas flow rate, as discussed in Section 3.3.3, is a very important consideration in producing device quality hydrogenated amorphous silicon and must be monitored closely.

An important part of any efficient solar cell structure is a low resistance ohmic contact since any contact resistance adds to the series resistance and reduces the available output power. One common method of producing ohmic contacts is to heavily dope a thin layer of material adjacent to the metal contact. This ensures that any barrier due to band bending which may exist will be sufficiently thin that carriers can easily tunnel through it. Another approach to achieving an ohmic contact on an amorphous silicon cell is to deposit a thin non-hydrogenated layer onto the metal contact. Non-hydrogenated amorphous silicon contains a large number of defect states and the effect on the metal-semiconductor junction is again to reduce the barrier thickness so that a tunneling ohmic contact results. Thompson *et al*. have used this technique and report improved device performance

with a non-hydrogenated interface layer.[59] This is also the technique employed here to obtain ohmic contacts at the back (unilluminated side) of devices. The non-hydrogenated layer is achieved by initially sputtering silicon in pure argon gas directly from the argon cylinder, bypassing the mixing tank. Prior to actual deposition, the target is extensively sputter cleaned, with the shutter shielding the substrate, to remove any hydrogen that may have been absorbed in the target. Non-hydrogenated silicon is then deposited onto the metal contact for 15 minutes yielding approximately a 1000 angstrom thick interface layer.

Following the non-hydrogenated ohmic contact layer, the hydrogenated amorphous silicon,or active part of the device, is deposited to a thickness of about 1 micron. The results of Chapter III may be used to help decide which deposition parameters are likely to yield the best photovoltaic material. Good device quality material should have a low density of states in the gap to allow a wide space charge layer. Because of the very short diffusion lengths of carriers in amorphous silicon, nearly all the photo current is due to generation in the space charge layer. The contribution due to diffusion of carriers generated outside the space charge layer is negligible. Also the $\mu\tau$ product should be sufficiently high so that the drift length, $\mu\tau E$, is large enough to prevent appreciable recombination in the space charge layer. That is, $\mu\tau E$ should be greater than the width of the space charge layer where E is the electric field in the space charge layer. A high $\mu\tau$ product also corresponds to a large photoconductivity which helps to reduce series resistance. For the rf sputtering system used here (it will likely differ for other systems and geometries), the highest $\mu\tau$ products occur at 200 watts input power. Also,for a

2.0 mTorr hydrogen partial pressure sample there was a 5 fold increase in $\mu\tau$ going from a 98.6% pure sputtering atmosphere to a 99.98% pure atmosphere. This indicates that the quality of the vacuum system, as determined by the leak rate, may be an extremely important factor influencing Schottky barrier device performance. In fact, a device fabricated by evaporating a gold contact onto hydrogenated amorphous silicon prepared at 2.0 mTorr hydrogen partial pressure and 20 mTorr argon partial pressure in a 99.7% pure sputtering atmosphere shows nearly perfectly linear and symmetrical I-V characteristics with no sign of rectification at all. Some band bending does exist at the gold-silicon interface because an open circuit voltage of 80 mV is observed when the device is illuminated with strongly absorbed blue light (λ = .450 μ). The barrier, however, is too thin to rectify the current flow, presumably because of a large number of defect states present, originating from impurities incorporated from the sputtering atmosphere. This is in contrast to observations of a similar gold Schottky barrier device prepared at 2.0 mTorr hydrogen partial pressure, 5.0 mTorr argon partial pressure, and a 99.98% pure sputtering atmosphere. This device (called device #3) shows excellent rectification characteristics in the dark and produces an open circuit voltage of 450 mV when illuminated with a tungsten light source. The properties of device #3 are reported in detail in the next two sections.

Another important factor influencing Schottky device characteristics is the method of deposition of the Schottky barrier metal contacts. A Schottky device (called device #2) was prepared under identical conditions as device #3 except the Schottky contact was platinum and was deposited by rf sputtering as opposed to evaporation. Platinum has a

work function equal to 5.4 eV as compared to 4.8 eV for gold. Therefore, everything else being equal, a better barrier would be expected with a platinum contact. This, however, is not observed as the platinum device #2 exhibits near linear and symmetrical I-V characteristics with no rectification. The open circuit voltage of this device is 320 mV under tungsten light illumination,indicating quite significant band bending at the interface. Again, however, the barrier is too thin to rectify the current flow. In this case, sputter damage to the surface of the hydrogenated amorphous silicon during the platinum deposition is probably responsible for a large number of surface states which result in a thin barrier. An inferiority of sputtered Schottky barriers has also been reported by Beichler et al.[60]

The next two sections describe the dark electrical and photovoltaic properties of two Schottky barrier devices fabricated by evaporating a thin gold contact onto hydrogenated amorphous silicon deposited by rf sputtering in a 99.98% pure atmosphere. One is device #3, as already mentioned, and the other (device #4) is prepared under the same conditions except with a hydrogen partial pressure of 3.0 mTorr. Both gold contacts are approximately 30% transmissive which, from the data of Schneider, indicates a gold thickness of about 200 Å.[61] Small contact pads of silver paint have been applied to the gold for protection against scratches. Figure 5.1 illustrates the device geometry.

5.3 Dark Current-Voltage Characteristics of Schottky Barrier Devices

Typical dark current-voltage curves of device #3 and device #4

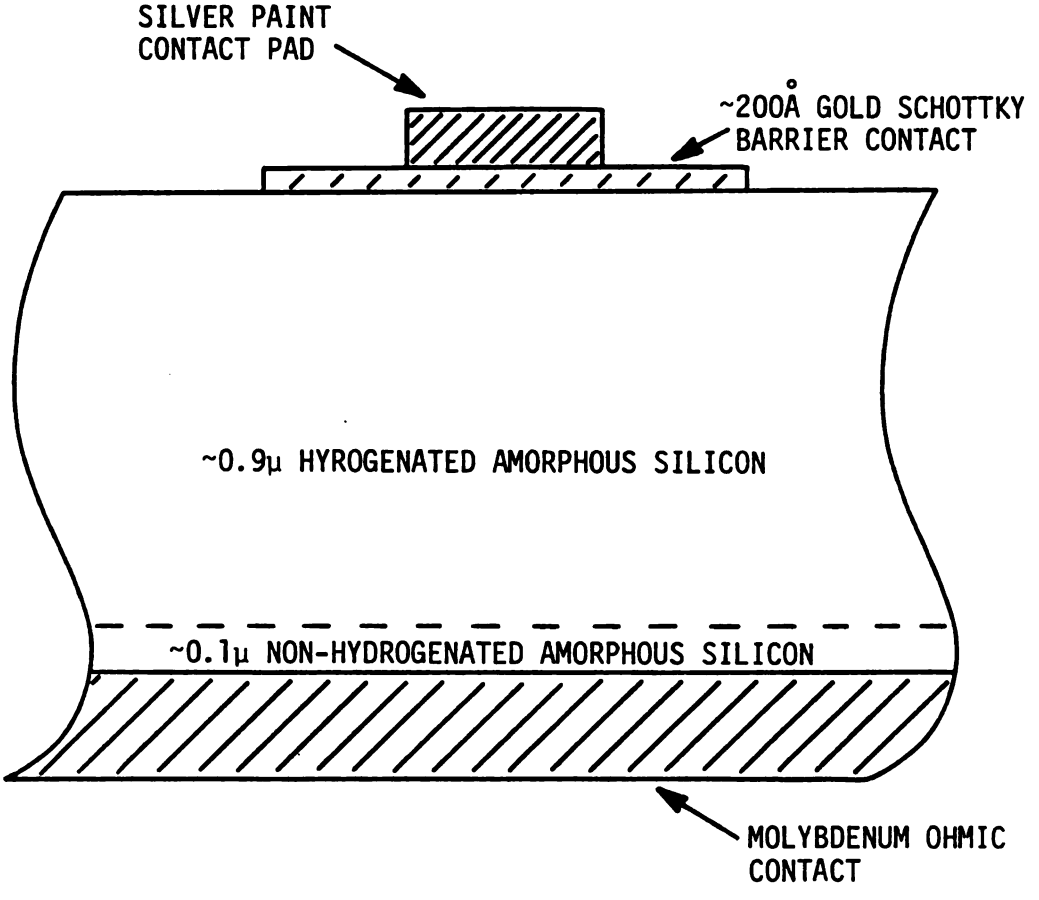

Figure 5.1 Schottky barrier device geometry.

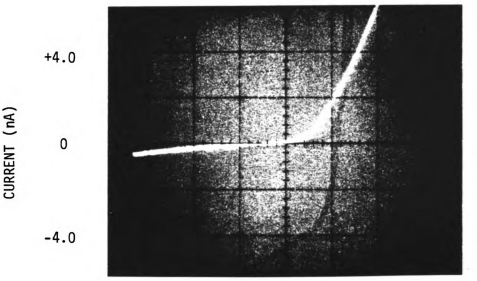

(a) Device #3

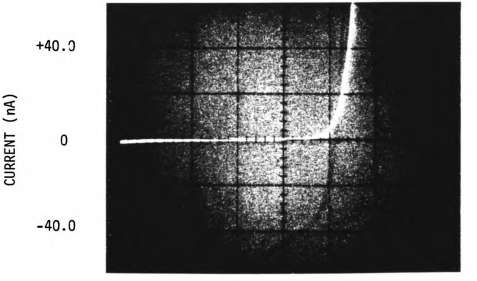

(b) Device #4

Figure 5.2 Dark I-V characteristics of Schottky barrier devices.

are shown in Figure 5.2 as displayed on a Tektronix 577 curve tracer operating in the dc mode. Excellent rectification characteristics are observed for both devices with rectification ratios greater than 100. For small forward bias, the current follows an exponential relationship with voltage, however, it is evident (especially for device #3) that a series resistance limits the forward current flow for higher applied bias. A large series resistance is a serious limitation in photovoltaic applications since part of the available output power is lost across any series resistance. This problem is diminished somewhat in actual operation, however, because the photoconductive effect reduces the series resistance when the device is illuminated.

The current density-voltage relationship for a Schottky barrier, including series resistance effects, may be written as

$$J = J_s(e^{q/nkT(V-R_sJA_t)}-1)$$

where V is the diode voltage, R_s is the series resistance, A_t is the device area, n is the diode quality factor, and J_s is the saturation current density. The forward bias J-V characteristics of devices #3 and #4 have been measured with a Keithly 610B Electrometer. The results are shown in Figures 5.3 and 5.4 along with the characteristics corrected for series resistance. The series resistance, diode quality factor, and saturation current density may be determined from three data points as[62]

$$R_s = \frac{(V_3-V_2)\ln(J_2/J_1) - (V_2-V_1)\ln(J_3/J_2)}{(J_3-J_2)A_t\ln(J_2/J_1) - (J_2-J_1)A_t\ln(J_3/J_2)}$$

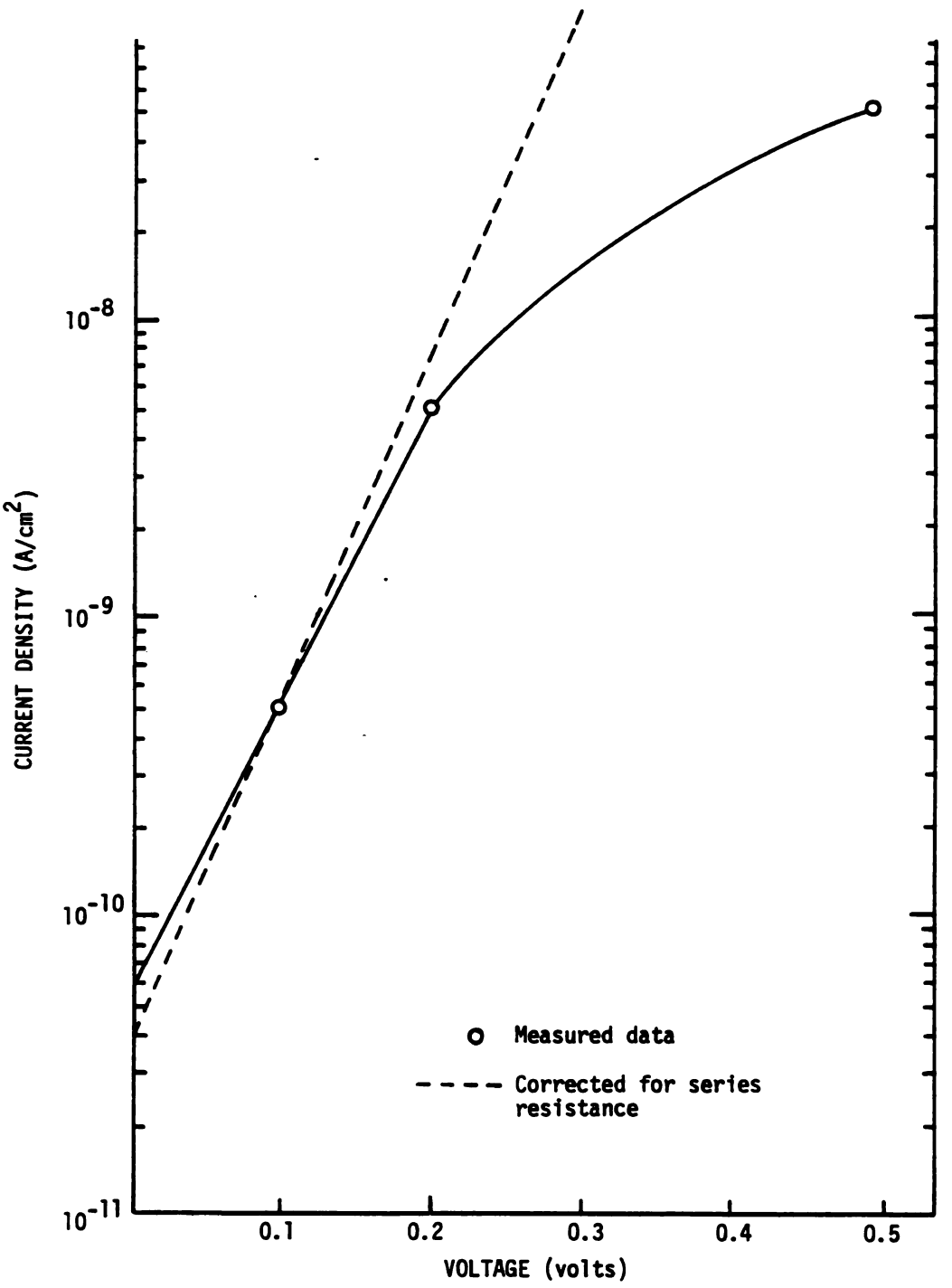

Figure 5.3 Forward bias current density - voltage characteristics of device #3.

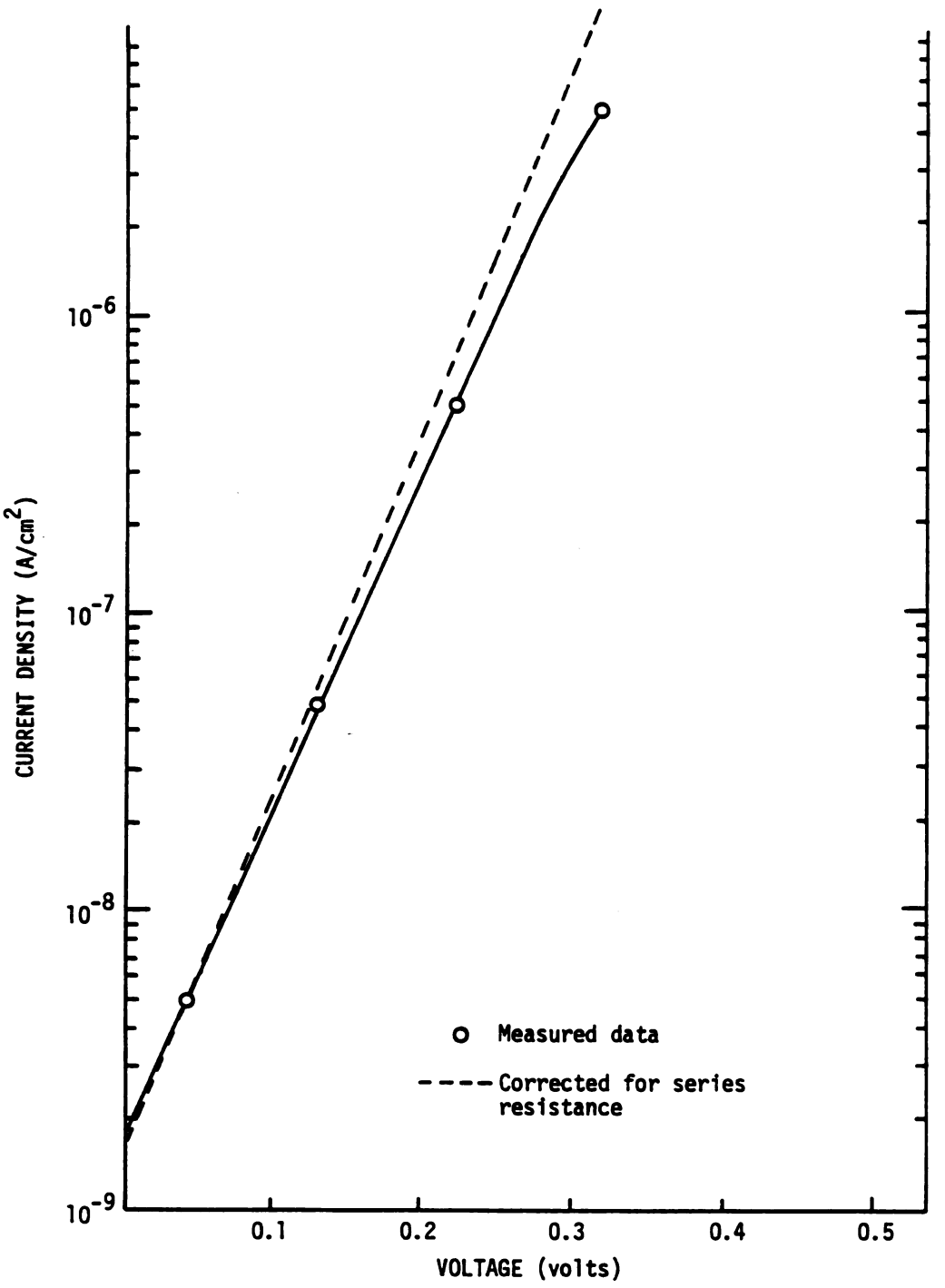

Figure 5.4 Forward bias current density - voltage characteristics of device #4.

$$n = \frac{kT}{q} \frac{(V_2-V_1) - R_s(J_2-J_1)A_t}{\ln(J_2/J_1)}$$

$$J_s = J_1 e^{-q/nkT(V_1-R_sJ_1A_t)} .$$

The results show that device #3 has a series resistance of 230 M, a diode quality factor of 1.43, and a saturation current density of $4.0 \times 10^{-11} A/cm^2$. The series resistance of device #4 is 740 kΩ, the diode quality factor is 1.46, and the saturation current density is $1.6 \times 10^{-9} A/cm^2$. The two orders of magnitude difference in series resistance and saturation current density have not been accounted for at this time. A value of n = 1 corresponds to an ideal Schottky barrier, whereas, values greater than 1 are due to interfacial layers, tunneling currents, or space charge layer recombination.[63] The Schottky barrier height, ϕ_B, may be determined from the expression for saturation current density

$$J_s = A^* T^2 e^{-q\phi_B/kT}$$

where A^* is the Richardson constant and T is the temperature. Solving this for ϕ_B yields

$$\phi_B = \frac{kT}{q} \ln\left(\frac{A^* T^2}{J_s}\right) .$$

At room temperature a value of $A^* = 100$ A-cm^{-2}-°K^{-2} may be used without significant error since a 100% change in A^* will cause only a 0.018 V change in ϕ_B.[64] For device #3, the barrier height is determined to be 1.03 V, and for device #4 it is 0.94 V.

5.4 Photovoltaic Characteristics of Schottky Barrier Devices

The results of measuring the short circuit current density as a function of light intensity for device #3 and device #4 are shown in

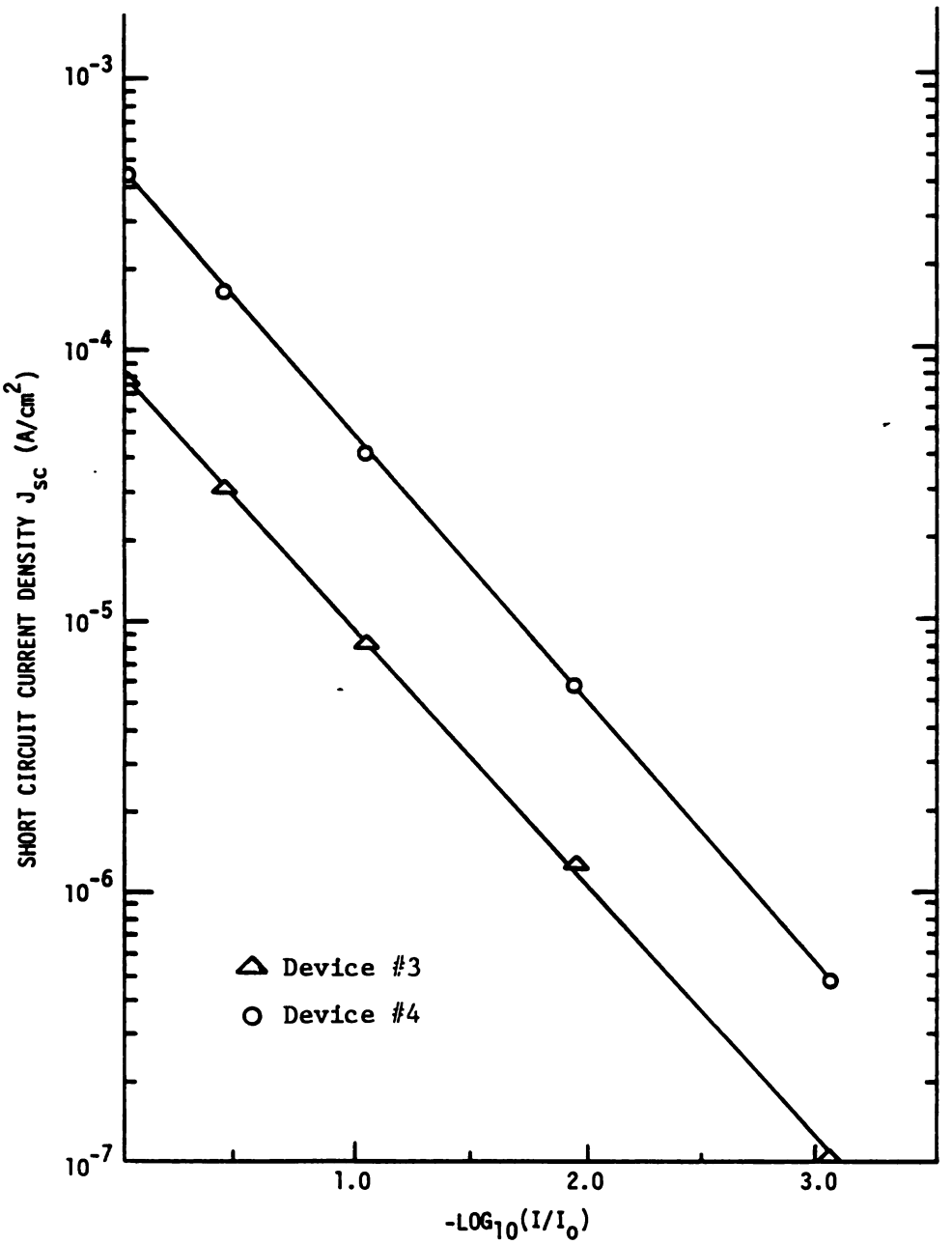

Figure 5.5 Short circuit current density vs. relative intensity for Schottky barrier devices.

Figure 5.5. The illumination is from a tungsten light source and is focused to give a maximum intensity of approximately 150 mW/cm^2. A series of neutral density filters of known optical density are used to accurately decrease the intensity in discrete steps. The short circuit current density is nearly linearly proportional to intensity over the three orders of magnitude investigated, from 0.15 to 150 mW/cm^2. This implies that current measurements on these particular devices at relatively low intensities, such as those available with a monochrometer, may be used to make conclusions about their performance at higher intensities. From the diode equation, the open circuit voltage is given by

$$V_{oc} = \frac{nkT}{q} \ln \left(\frac{J_{sc}A_a}{J_sA_t} + 1\right)$$

where A_a and A_t are the active and total device areas, respectively. Measurements on both devices reveal a logarithmic dependence of V_{oc} with intensity as predicted by the above equation,taken together with the linear dependence of J_{sc} with intensity (Figure 5.6). The data for device #3 deviates slightly from a logarithmic dependence as V_{oc} begins to saturate at the higher intensities. This would be the case if high level injection effects were beginning to occur.

The external spectral response, or collection efficiency at each wavelength, is defined as the number of electron-hole pairs collected under short circuit conditions at each wavelength relative to the number of photons incident on the surface at that wavelength, [63] i.e.,

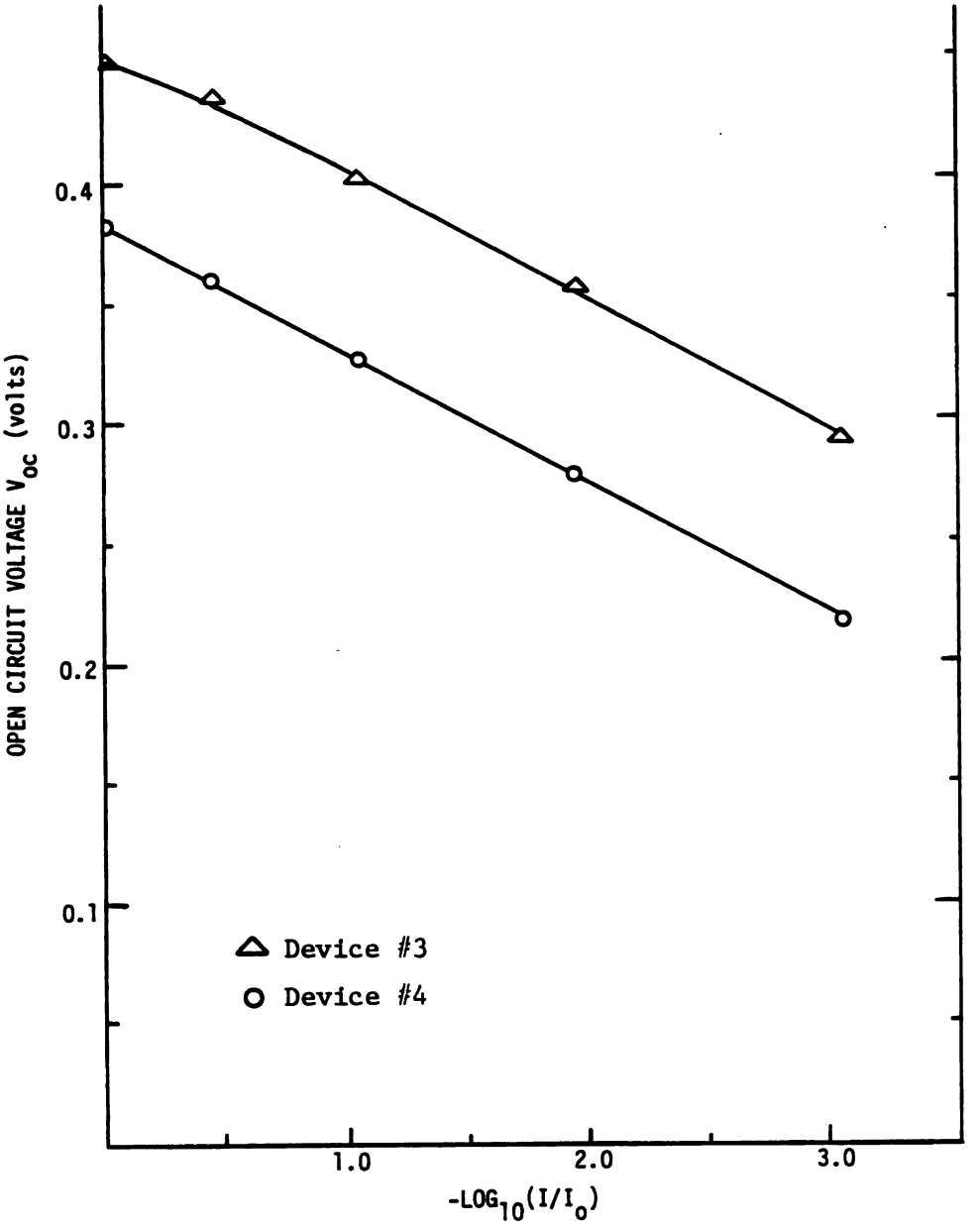

Figure 5.6 Open circuit voltage vs. relative intensity for Schottky barrier devices.

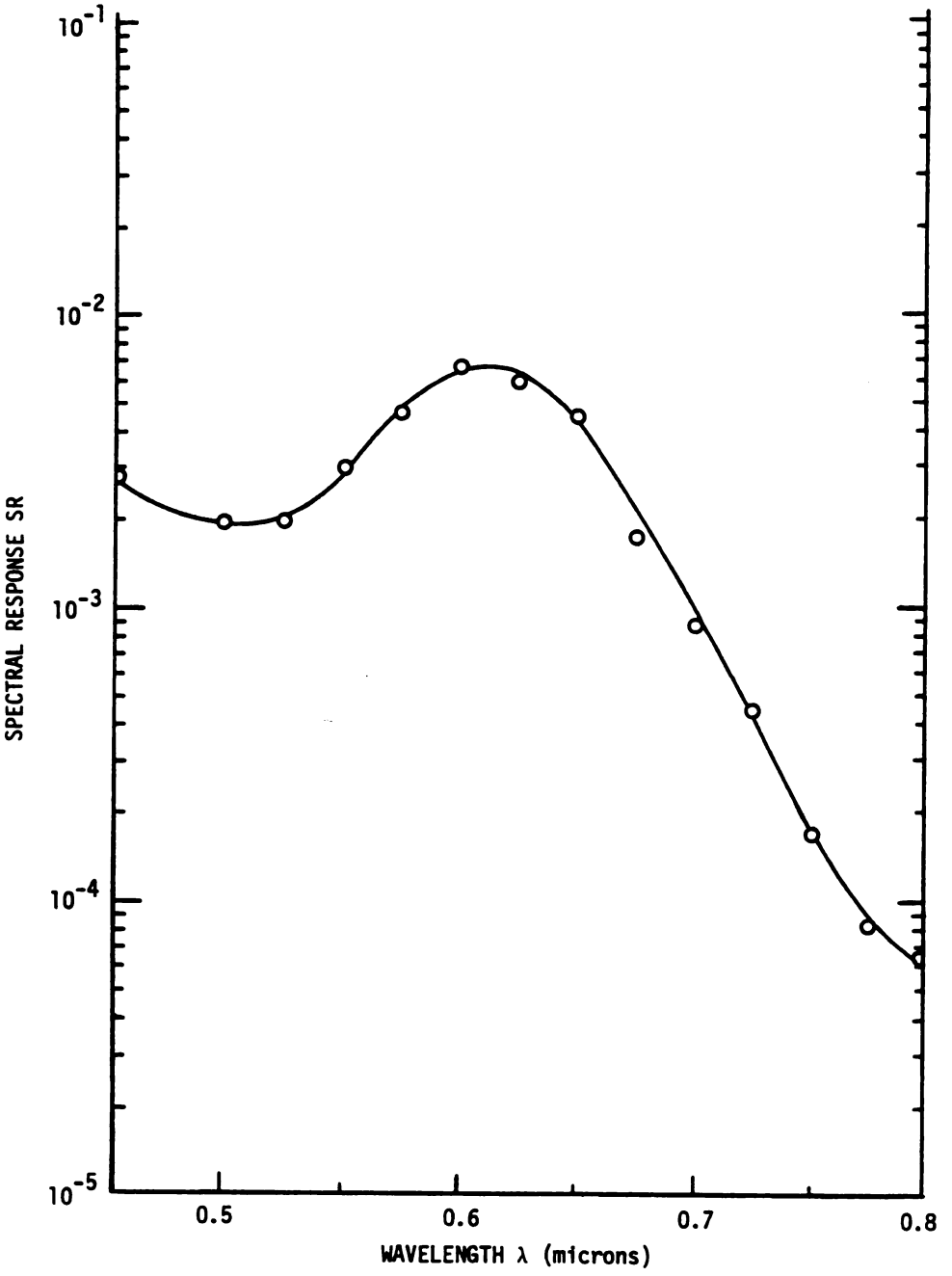

Figure 5.7 Measured spectral response of Schottky barrier device #3

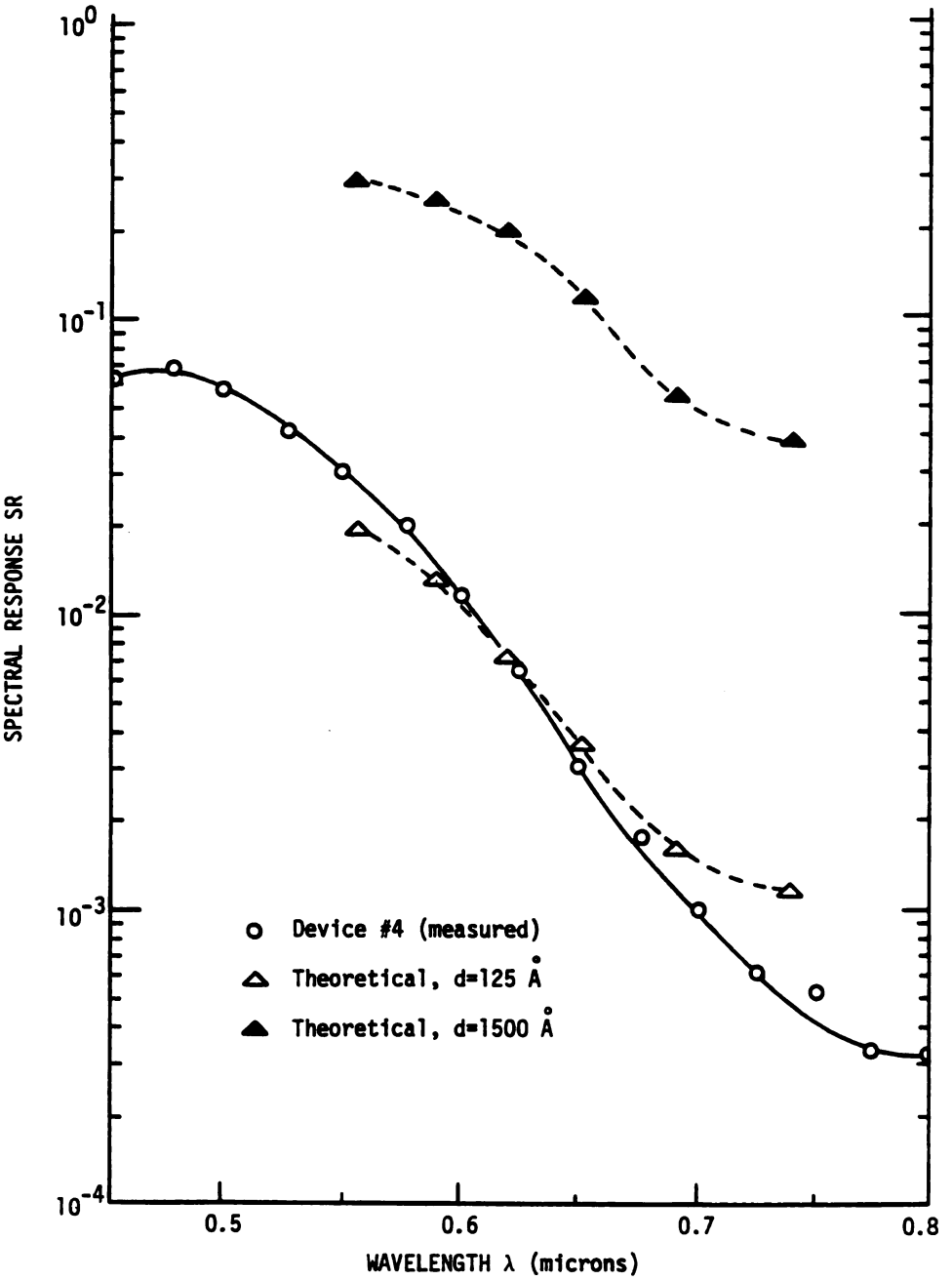

Figure 5.8 Measured and theoretical spectral response of Schottky barrier device #4.

$$SR(\lambda) = \frac{J_{sc}(\lambda)}{qF(\lambda)} \quad .$$

The external spectral response of these devices have been measured throughout the visible spectrum using a Bausch and Lomb monochrometer with output intensities of 0.9 - 2.5 mW. Figures 5.7 and 5.8 show the results of these measurements. Even at the shorter wavelengths where the spectral responses are maximum, they are still considerably less than unity suggesting that recombination in the space charge layers or narrow space charge layers are limiting the collection efficiency.

The spectral response, assuming recombination in the space charge layer, may be written as[65]

$$SR = \frac{2\gamma}{d}\left(1 - e^{-\alpha d} - \frac{1-e^{-d(\alpha+1/\gamma)}}{1 + 1/\gamma\alpha}\right)$$

where d is the width of the collection region (effectively the width of the space charge layer) and γ is the drift length of holes and electrons, assumed equal here, defined as $\gamma = \mu\tau E$. E is the electric field in the collection region and is given by $E = V_{bi}/d$, where V_{bi} is the built-in voltage. Also, α is the absorption coefficient. Using the absorption coefficient data from Chapter III, values for $\mu\tau$ determined from photoconductivity, and approximating the built-in voltage as the maximum open circuit voltage, the above equation can be fitted to the spectral response data. For device #4, after taking into account the transmission of the gold contact, a good fit is found for a space charge layer width d = 125 Å as shown in Figure 5.8. Furthermore,

the spectral response, neglecting recombination, given as

$$SR = 1 - e^{-\alpha d}$$

also gives a space charge layer width of 125 Å when fitted to the data. This shows that for the values of $\mu\tau$ used, the relatively poor spectral response is not due to recombination in the space charge layer but due to a quite narrow space charge layer.

Considering the reverse bias breakdown characteristics of device #4 shown in Figure 5.9, reversible breakdown occurs at about 1.0 volts which supports the concept of a thin space charge layer. In one-sided p-n junctions in crystalline silicon, a breakdown voltage of 1 volt corresponds to a background doping of 1.25×10^{19} cm^{-3}.[66] The corresponding space charge layer width is approximately 110 Å.[67] Such a comparison with the amorphous silicon devices in this study is reasonable since the barrier heights to the tunneling process are comparable. V_{bi} for the heavily doped crystalline devices is approximately 1.0 volts as is the metal-semiconductor barrier in the amorphous devices.

For such a narrow space charge layer, $\mu\tau$ would have to be in the range of 10^{-11} cm^2/V for appreciable recombination in the space charge layer. Since the measured $\mu\tau$ is 2 orders of magnitude greater, essentially all the holes and electrons generated in the space charge layer may be assumed to be collected.

The spectral response of device #3 and #4 both deviate from the theoretical calculations at low λ and high α. This is common, to some extent, for any Schottky barrier device and is due to surface recombination

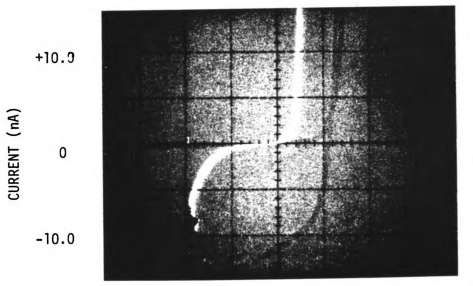

(a)

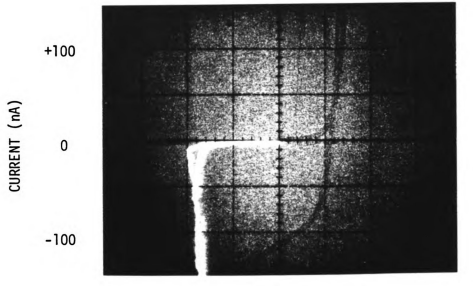

(b)

Figure 5.9 Reverse breakdown characteristics of Schottky barrier device #4.

and near-surface recombination due to defects. However, the non-ideal effects are much more pronounced in device #3.

The I-V characteristics of both devices under illumination equivalent to AM1 (solar illumination under ideal conditions = 100 mW/cm^2) are shown in Figure 5.10. The light source is a tungsten bulb and has been calibrated with an Eppley Radiometer. Device #3 displays a V_{oc} = 0.41 V and a J_{sc} = 0.11 mA/cm^2. From the shape of the I-V curve it is apparent that there is a large series resistance limiting, to some extent, the short circuit current. This series resistance is about 200 kΩ. The fill factor is defined as the ratio of the voltage-current product at the maximum output power point and the product of V_{oc} J_{sc}, i.e.,

$$FF = \frac{V_m J_m}{V_{oc} J_{sc}} \quad .$$

If the fill factor, the open circuit voltage, and the short circuit current density are known, the conversion efficiency may be determined. For device #3, FF = 0.25 and thus the conversion efficiency is 0.01%. Series resistance is not the limiting factor in device #4 with a value of about 3 kΩ. Device #4 exhibits a V_{oc} = 0.35 V, J_{sc} = 0.48 mA/cm^2, and FF = 0.50, thus the conversion efficiency is 0.09%. Here the small value of J_{sc} limits the efficiency and is due to the narrow width of the space charge layer.

With the above information,along with some of the results of Chapter III, simplified energy band diagrams may be sketched for these devices. Figure 5.11 shows possible band diagrams for device #3 and device #4.

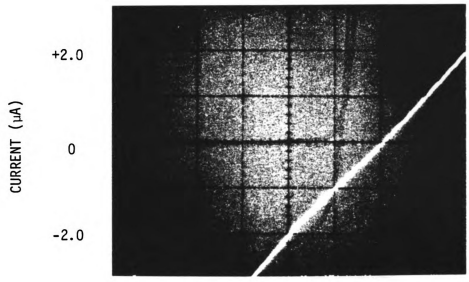

(a) Device #3

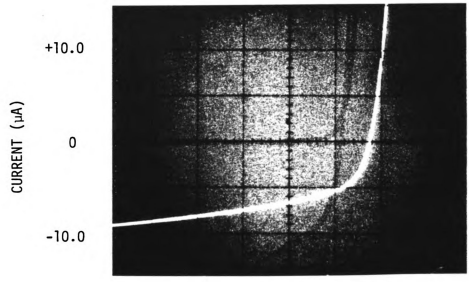

(b) Device #4

Figure 5.10 I-V characteristics of Schottky barrier devices under illumination equivalent to AM1.

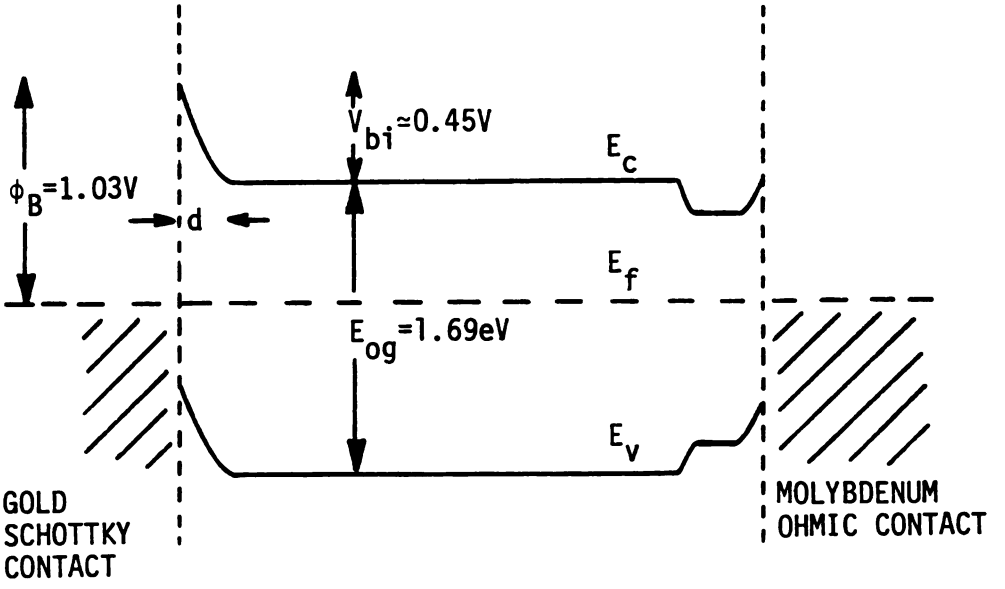

(a) Device #3

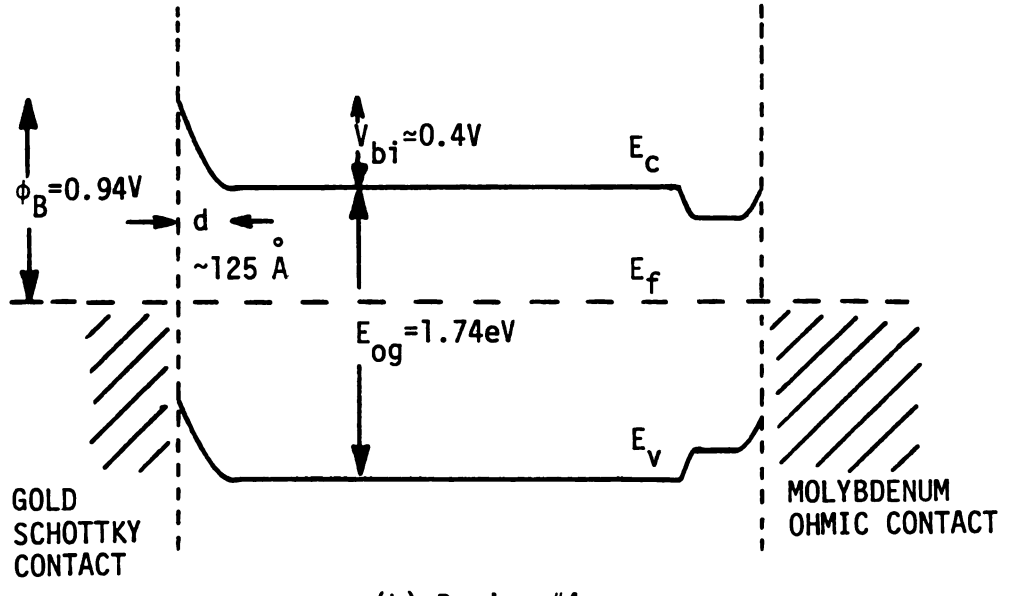

(b) Device #4

Figure 5.11 Energy band diagrams of Schottky barrier devices.

5.5 Conclusions

The sample preparation conditions which yield Schottky barrier devices have been presented in this chapter. Two of the important factors influencing device performance are the purity of the sputtering atmosphere and the method of Schottky metal contact deposition. When the sputtering atmosphere is 99.98% pure, Schottky barrier devices with good rectification characteristics are formed, for 99.7% pure atmosphere they are not. Sputtering the Schottky metal contact results in a large number of defect surface states caused by sputter damage,and rectifying devices are not formed. Therefore, evaporation deposition is preferred, and two gold-hydrogenated amorphous silicon devices have been fabricated with this technique.

The two series of devices fabricated show good Schottky diode characteristics in the dark with rectification ratios greater than 100 and diode quality factors of 1.43 and 1.46. Saturation current densities of $1.6 \times 10^{-9} A/cm^2$ and $4.0 \times 10^{-11} A/cm^2$ have been determined by extrapolation of the forward bias characteristics yielding Schottky barrier heights of 0.94 V and 1.03 V. All of these parameters compare favorably with other amorphous silicon devices reported in the literature.

The photovoltaic characteristics of these devices have been determined under tungsten light illumination equivalent to AM1. Open circuit voltages of 0.41 V and 0.35 V are observed which are less than the best reported values but are fairly equivalent to typical values. Short circuit current densities are 0.11 mA/cm^2 and 0.48 mA/cm^2 and conversion efficiencies are 0.01% and 0.09%. The best values here are

about 25 times smaller than the best reported sputtered devices.[68] Evidence is given which indicates that the collection efficiency is limited by narrow space charge layers and not $\mu\tau$ products or recombination. To widen the space charge layer, hence improve the collection efficiency, the purity of the sputtering atmosphere must be improved by using higher purity cylinder gases and further reducing the leak rate.

CHAPTER VI

SUMMARY AND CONCLUSIONS

The objectives of this research have been two-fold: 1) to investigate the co-sputtering of silicon and substitutional impurities from composite targets in a hydrogenated atmosphere as an alternate technique for preparing doped hydrogenated amorphous silicon; 2) to investigate the effects of deposition parameters on material properties in order to facilitate the determination of the best sputtering conditions to achieve optimum semiconductor characteristics. In particular, the deposition atmosphere purity requirements for producing device quality material and Schottky barrier photovoltaic devices in a rf sputtering system have been established. This study was motivated by the growing interest in using amorphous silicon in place of crystalline silicon in several semiconductor device applications. A prime motivation was that hydrogenated amorphous silicon has potential to meet the demand for inexpensive large-area photovoltaic arrays for electric power generation.

The fabrication techniques of rf sputtered hydrogenated amorphous silicon samples and the experimental procedures for determining the optical and electrical properties have been described in Chapter III. These properties were studied as functions of the hydrogen partial pressure in the sputtering atmosphere and the rf input power. A technique to determine the mobility-lifetime product from

photoconductivity data under non-uniform illumination conditions was developed. Using this technique, mobility-lifetime products from $2.3 \times 10^{-10} cm^2/V$ to $9.6 \times 10^{-9} cm^2/V$ were observed. The effects of sputtering atmosphere purity, as determined by the leak rate into the vacuum system versus the gas flow rate through the system, were also observed. It was found that the mobility-lifetime product increased from $1.9 \times 10^{-9} cm^2/V$ to $9.6 \times 10^{-9} cm^2/V$ when the sputtering atmosphere purity increased from 98.6% to 99.98%. Models were suggested to explain the observed behavior of the dark and photo conductivity. The results of Chapter III were used as a guide in selecting the deposition parameters for the fabrication of Schottky barrier photovoltaic devices reported in Chapter V. Chapter IV reported the investigation of co-sputtering silicon with aluminum and arsenic solid impurities in a hydrogenated atmosphere as an alternate method of preparing doped hydrogenated amorphous silicon samples. The modification of the optical and electrical properties were reported and results were compared to those reported for gaseous doped, ion implanted, and other co-sputtered and co-evaporated films. For co-sputtered aluminum films, the room temperature conductivity was varied over seven orders of magnitude, from $10^{-12} (\Omega\text{-cm})^{-1}$ to $10^{-5} (\Omega\text{-cm})^{-1}$, and the optical energy gap was also varied from 1.83 eV to 0.87 eV, by sputtering from a composite Si/Al target with aluminum making up 0% to 10.6% of the target area. Co-sputtering aluminum was found to be a less efficient method of p type doping, in terms of the number of incorporated aluminum atoms which act as acceptors, than gas phase or ion implantation. Still, co-sputtering is an interesting approach

to impurity incorporation because of the inherent simplicity of the preparation techniques and required apparatus, and because it may be applied to a large class of solid materials not readily available in gaseous form. Also it has been observed to lead to effective tailoring of the optical energy gap. Fabrication techniques and the dark and photovoltaic characteristics of Schottky barrier devices were reported in Chapter V. The important results were the determination of the purity of the sputtering atmosphere which resulted in the formation of rectifying Schottky barriers, and the method of Schottky metal contact deposition. It was found that rectifying Schottky barrier devices resulted when the deposition atmosphere purity was 99.98% and the Schottky contact was deposited by evaporation. Sputtering in a less pure atmosphere or sputtering the Schottky contact resulted in non-rectifying devices. Device characteristics were compared to those reported in the literature and it was concluded that the short circuit current was limited by the thickness of the space charge layer which resulted in relatively low conversion efficiencies. A space charge layer thickness of approximately 125 Å was determined for one device from spectral response data.

The next step to achieve in device fabrication with the rf sputtering system in this study, is wider space charge layers. An order of magnitude increase, to approximately 1500 Å, is needed to achieve photovoltaic efficiencies comparable to the best results of others. Such an increase will presumably require an improvement in the sputtering atmosphere purity. A reasonable goal is 99.999%, which will require a reduction in leak rate. A helium leak test of

the system will be required to find and eliminate leaks down to about 10^{-7} scc/sec if the present gas flow rate is to be maintained.

An additional area for further study is in the relationship between deposition parameters and semiconductors properties. There is a need for further understanding of the underlying reasons behind a change in a particular parameter, such as power, and a corresponding change in a particular property, such as $\mu\tau$. For example, consider the mechanisms for the reaction

$$Si + H_x \rightarrow SiH_x.$$

This could be due to target hydrogenation, plasma interactions, surface reactions on the substrate, or any combination of the three. In fact the exact mechanisms of hydrogenation of the films are not known in any detail. Evidence has been presented here that favors a plasma silicon-hydrogen interaction, but does not rule out hydrogenation at the target or substrate. An understanding of the relationship between deposition parameters and material properties requires a clear identification of the hydrogenation mechanisms.

Also, it would be useful to relate deposition parameters to more basic phenomena. Again considering power as an example, one may note that increasing power may correspond to an increasing plamsa electron temperature, electron concentration, and increasing velocity of both sputtering ions and reactive ions. Models relating these more basic phenomena to material properties could provide useful insights into the question of improving amorphous silicon devices. Such models will require more information about the plasma itself which may be obtained by spectroscopic and plasma probe experiments.

LIST OF REFERENCES

LIST OF REFERENCES

1. R.C. Chittick, J.H. Alexander and H.F. Sterling, J. Electrochem. Soc., 116, 77 (1969).

2. Paul D. Maycock, 14th IEEE Photovoltaic Specialists Conf. - 1980, San Diego, CA., 6.

3. Joseph J. Loferski, IEEE Spectrum, 17, 26 (1980).

4. D.E. Carlson, C.R. Wronski, A.R. Triano and R.E. Daniel, 12th IEEE Photovoltaic Specialists Conf. - 1976, Baton Rouge, LA., 893.

5. D.E. Carlson, 14th IEEE Photovoltaic Specialists Conf. - 1980, San Diego, CA., 291.

6. W.E. Spear and P.G. LeComber, Phil. Mag., 33, 935 (1976).

7. D.E. Carlson and C.R. Wronski, Appl. Phys. Lett., 28, 671 (1976).

8. M.H. Brodsky, J. Vac. Sci. and Tech., 8, 125 (1971).

9. A. Madan, P.G. LeComber and W.E. Spear, J. Non-cryst. Sol., 20-21, 239 (1976).

10. A.K. Malhorta and G.W. Neudeck, Appl. Phys. Lett., 28, 47 (1976).

11. W.E. Spear and P.G. LeComber, J. Non-cryst. Sol., 8-10, 727 (1972).

12. W.E. Spear, P.G. LeComber, S. Kinmond and M.H. Brodsky, Appl. Phys. Lett., 28, 105 (1976).

13. D.E. Carlson and C.R. Wronski, J. Elec. Mat., 6, 95 (1977).

14. W. Paul, A.J. Lewis, G.A.N. Connell and T.D. Moustakas, Sol. St. Commun., 20, 969 (1976).

15. M.H. Brodsky, Manuel Cardona and J.J. Cuomo, Phys. Rev. B, 16, 3556 (1977).

16. J.C. Knights, G. Lucovsky and R.J. Nemanich, Phil. Mag. B, 37, 467 (1978).

17. E.C. Freeman and William Paul, Phys. Rev. B, 18, 4288 (1978).

18. D.A. Anderson, T.D. Moustakas and W. Paul, 7th Inter. Conf. on Amorphous and Liquid Semic., ed. by W.E. Spear, 334 (1977).

19. F.R. Jeffrey, H.R. Shanks and G.C. Danielson, J. Appl. Phys., 50, 7034 (1979).

20. S.R. Ovshinsky and A. Madan, Nature, 276, 482 (1978).

21. H. Mell, L. Schweitzer and U. Voget-Grote, J. Non-cryst. Sol., 35 & 36, 639 (1980).

22. N. Van Dong and T.Q. Hai, J. Non-cryst. Sol., 35 & 36, 351 (1980).

23. G. Müller, S. Kalbitzer, W.E. Spear and P.G. LeComber, 7th Inter. Conf. on Amorphous and Liquid Semic., ed. by W.E. Spear, 442, (1977).

24. Y. Hamakawa, H. Okamoto and Y. Nitta, 14th IEEE Photovoltaic Specialists Conf. - 1980, San Diego, CA., 1074.

25. L.I. Maissel and R. Glang, Handbook of Thin Film Technology, Chapters 3 & 4, McGraw-Hill, Inc. 1970.

26. J.L. Vossen and J.J. O'Neill, Jr., RCA Rev., 29, 149 (1968).

27. D.K. Reinhard, Ph.D. Thesis, Massachusetts Institute of Technology (1973).

28. S. Wang, Solid State Electronics, 650, McGraw-Hill, Inc. 1966.

29. G.A.N. Connell and A. Lewis, phys. stat. sol (b), 60, 291 (1973).

30. G.A.N. Connell and J.R. Pawlik, Phys. Rev. B, 13, 787 (1976).

31. K. Weiser and M.H. Brodsky, Phys. Rev. B, 1, 791 (1970).

32. R.A. Smith, Semiconductors, 201-210, Cambridge University Press 1959.

33. G. Lucovsky, R.J. Nemanich and J.C. Knights, Phys. Rev. B, 19, 2064 (1979).

34. P.G. LeComber, A. Madan and W.E. Spear, Electronic and Structural Properties of Amorphous Semiconductors, ed. by P.G. LeComber and J. Mort, 373-392, Academic Press 1973.

35. T.D. Moustakas, J. Elec. Mat., 8, 391 (1979).

36. T.D. Moustakas, D.A. Anderson and William Paul, Sol. St. Commun., 23, 155 (1977).

37. M.A. Paesler, D.A. Anderson, E.C. Freeman, G. Moddel and William Paul, Phys. Rev. Lett., 41, 1492 (1978).

38. D.L. Staebler, J. Non-cryst. Sol., 35 & 36, 387, (1980).

39. W.E. Spear, Adv. in Phys., 26, 811 (1977).

40. R.O. Bell, Appl. Phys. Lett., 36, 936 (1980).

41. P. Nath, S.K. Barthwal and K.L. Chopra, Sol. St. Commun., 16, 301 (1975).

42. R.W. Vass, M.A. Meininger and R.M. Anderson, J. Appl. Phys., 45, 843 (1974).

43. R. Messier, A.K. Sarkar and R. Roy, Mat. Res. Bull., 9, 157 (1974).

44. J.J. Hauser, Sol. St. Commun., 13, 1451 (1973).

45. W.E. Spear and P.G. LeComber, Sol. St. Commun., 17, 1193 (1975).

46. J.C. Knights, Phil. Mag. B, 34, 663 (1976).

47. W.C. Dash and R. Newmann, Phys. Rev., 99, 1151 (1955).

48. D.E. Hill, Phys. Rev, 133, A866 (1964).

49. D.A. Anderson, Bull. Am. Phys. Soc., 23, 249 (1978).

50. P.G. LeComber and W.E. Spear, and G. Müller and S. Kalbitzer, J. Non-cryst. Sol., 35 & 36, 327 (1980).

51. N.V. Dong and T.Q. Hai, phys. stat. sol. (b), 88, 555 (1978).

52. W.E. Spear and P.G. LeComber, and S. Kalbitzer and G. Müller, Phil. Mag. B, 39, 159 (1979).

53. T. Shimizu, M. Kumeda, I. Watanabe and Y. Noumi, J. Non-cryst. Sol., 35 & 36, 645 (1980).

54. L.I. Maissel and R. Glang, 3-27.

55. T.D. Moustakas, C.R. Wronski and D.L. Morel, J. Non-cryst. Sol., 35 & 36, 719 (1980).

56. M. Shur, W. Czubatyj and A. Madan, J. Non-cryst. Sol., 35 & 36, 731 (1980).

57. L. Vieux-Rochaz and A. Chenevas-Paule, J. Non-cryst. Sol., 35 & 36, 737 (1980).

58. J.I.B. Wilson and P. Robinson, Solid State Elec., 21, 489 (1978).

59. M.J. Thompson, J. Allison, M.M. Alkaisi and I.P. Thomas, Revue de Phys. Appl., 13, 625 (1978).

60. J. Beichler, W. Fuhs, H. Mell and H.M. Welsch, J. Non-cryst. Sol., 35 & 36, 587 (1980).

61. M.V. Schneider, Bell System Tech. J., 45, 1611 (1966).

62. L.J. Giacoletto, Electronics Designers' Handbook, 10-1, McGraw-Hill, Inc. 1977.

63. H.J. Hovel, Semiconductors and Semimetals - Volume 11 Solar Cells, 112-126, Academic Press 1975.

64. S.M. Sze, Physics of Semiconductor Devices, 363-424, John Wiley & Sons, Inc. 1969.

65. R.O. Bell, Appl. Phys. Lett., 36, 936 (1980).

66. James M. Feldman, The Physics and Circuit Properties of Transistors, 341-342, John Wiley & Sons, Inc. 1972.

67. S.M. Sze, 89.

68. M.J. Thompson, M.M. Alkaisi and J. Allison, Proc. of Inter. Photovoltaic Conf., Berlin, 1979, 303.